Western Graduate&PostdoctoralStudies

Western University

Scholarship@Western

Electronic Thesis and Dissertation Repository

8-30-2013 12:00 AM

In situ High-Pressure Studies of Energetic Materials by Vibrational Spectroscopy and X-ray diffraction

Liang Zhou
The University of Western Ontario

Supervisor
Yang Song
The University of Western Ontario

Graduate Program in Chemistry
A thesis submitted in partial fulfillment of the requirements for the degree in Master of Science
© Liang Zhou 2013

Follow this and additional works at: https://ir.lib.uwo.ca/etd

Part of the Physical Chemistry Commons

Recommended Citation

Zhou, Liang, "In situ High-Pressure Studies of Energetic Materials by Vibrational Spectroscopy and X-ray diffraction" (2013). *Electronic Thesis and Dissertation Repository*. 1592.
https://ir.lib.uwo.ca/etd/1592

This Dissertation/Thesis is brought to you for free and open access by Scholarship@Western. It has been accepted for inclusion in Electronic Thesis and Dissertation Repository by an authorized administrator of Scholarship@Western. For more information, please contact wlswadmin@uwo.ca.

In situ High-Pressure Studies of Energetic Materials by Vibrational Spectroscopy and X-ray Diffraction

(Thesis format: Integrated-Article)

By

Liang Zhou

Graduate Program in Chemistry

A thesis submitted in partial fulfillment
of the requirements for the degree of
Master of Science

The School of Graduate and Postdoctoral Studies
The University of Western Ontario
London, Ontario, Canada

© Liang Zhou 2013

Abstract

Nitrogen-rich materials have been considered as the most promising replacement of traditional energetic materials due to the large energy difference between the different nitrogen allotropes. Apart from the traditional chemical synthesis, high-pressure technique had been proved an effective tool to create such kinds of materials. Here we report studies of four promising precursors, 5-aminotetrazole, 5-methyltetrazole, 5, 5´-bis(2-methyltetrazolyl)amine monohydrate and cyanuric triazide, under high pressure by Raman and IR spectroscopy. 5, 5´-bis(2-methyltetrazolyl)amine monohydrate and cyanuric triazide were also studied using X-ray diffraction. Besides, the high-pressure behavior of s-triazine was also investigated to understand the properties of cyanuric triazide.

Firstly, 5-aminotetrazole and 5-methyltetrazole were investigated to examine the pressure effects on the ring structures and the high-pressure behaviors. No phase transitions for 5-aminotetrazole were found in the whole pressure range. However, four phase transitions were observed for 5-methyltetrazole, evidenced by the by the appearance of new lattice modes, the changes in peak profile as well as the pressure dependence of Raman lattice modes. Upon decompression, the tetrazole ring vibration modes in both compounds were fully recovered, suggesting the tetrazole ring had very high stability.

Then 5, 5´-bis(2-methyltetrazolyl)amine monohydrate was investigated by vibrational spectroscopy and X-ray diffraction. All the result suggested there were no phase transitions in the entire investigated pressure range. Upon decompression, all the Raman and IR modes were completely recovered, indicating the reversibility and high stability of this material.

At last, s-triazine and cyanuric triazide were studied. A total of four phase transitions for s-triazine were observed, evidenced by changes in peak profile, the number of vibrational modes, as well as the pressure dependence of Raman lattice modes over different pressure ranges. The transition was identified irreversible for the lattice modes were not recovered upon decompression. In addition, a ring-opening reaction took place, suggested by the recovered Raman and IR internal modes. For cyanuric triazide, no phase transitions were observed in the pressure range of 0-26 GPa and one chemical reaction above 26 GPa. In addition, the transition was partially irreversible evidenced by the different Raman profiles in different parts of the sample. A possible reaction mechanism was proposed accordingly.

Keywords

High pressure · Diamond anvil cell · Vibrational spectroscopy · X-ray diffraction · Nitrogen-rich materials · Energetic materials · Polymeric nitrogens · Phase transitions · Ring-opening reaction

The Co-Authorship Statement

I hereby declare that this thesis I made a major contribution to the work in the experimental design, data analysis and interpretation. Prof. Yang Song is a co-author on all materials presented in this thesis and played a major role in the editing and revision of the materials presented in all chapters.

The 5, 5´-bis(2-methyltetrazolyl)amine monohydrate in chapter 3 and the cyanuric triazide in chapter 4 were synthesized by Prof. Muralee Murugesu’s group in the University of Ottawa. High-pressure properties of 5, 5´-bis(2-methyltetrazolyl)amine monohydrate was simulated by Dr. Anguang Hu in Defence Research and Development Canada-Suffield. The Raman spectra of s-triazine and the IR spectra of cyanuric triazide were measured by undergraduate student Erica Till under my supervision.

I am aware of the University of Western Ontario Policy on Authorship and I certify that I have properly acknowledged the contribution of other researchers to my thesis.

I certify that, with the above qualifications, this thesis, and the research to which it refers, is the product of my own work.

Acknowledgements

First of all, I would like to acknowledge my advisor Prof. Yang Song for his exceptional supervision, encouragement and guidance during the past two years, without which my graduate studies would not have been possible. His passion and enthusiasm are something I will always admire. I also would like to thank my collaborators, Prof. Muralee Murugesu and Dr. Anguang Hu for all their input. In addition, I thank for Prof. Nicholas C. Payne and Prof. T. K. Sham for their excellent teaching.

I would also like to thank all the members of the Song's group (Yue Hu, Zhihao Yu and Ankang Zhao and Haiyan Mao) as well as the former group members (Zhaohui Dong and Vinod Panchal). Thank for their help during the past two years and the happiness brought to me.

Special thanks to all of my friends (Zhiqiang Wang & Ruiping Ge, Xiaoxuan Guo, Michael Wu, Yixing Tang, Peng He, Yiyi Liu, Rachel Wang & Jinqiang Hou, Fuyan Zhao & Fangfang Zhou, Dong Zhao, Jian Chen, Lu Zhang, Lijia Liu, Sonia Lin, Renjie Hou, Jun Xu, Junwei Sun, Jun Li, Bo Fan, Nazhen Liu, Donghan Chen, Yu Sun, Jia Jia, Ming Huang, Jiacheng Guo, Jing Zhang, Jing Chao, Xiangrong Zhang, Mengdi Fan, Cong Bi, Lei Wang, Huilei Zhao, Changmiao Guo, Qichang Meng and Yuan Wang). I really missed those happy times we enjoyed together!

In addition, I thank the help from Darlene McDonald, Clara Fernandes, Anna Vandendvrie, Barakat Misk, John Vanstone, Jon Aukema and Monica Chirigel.

Finally I would like to thank my parents for their love, understanding and unconditional support during the past two years.

Table of Contents

List of Figures

List of Tables

List of Abbreviations

TNT	Trinitrotoluene
RDC	1,3,5-trinitrohexahydro-1,3,5-triazine
HMX	1,3,5,7-tetranitro-1,3,5,7-tetrazacyclooctane
GPa	Giga-pascal
DAC	Diamond anvil cell
XRD	X-ray diffraction
DPSS	Diode pumped solid state
CCD	Charge-coupled device
FTIR	Fourier transform infrared
MCT	Mercury cadmium telluride
KB	Kirkpatrick-Baez
CL-20	Hexanitrohexaazaisowurtzitane
5-ATZ	5-aminotetrazole
5-MTZ	5-methyltetrazole
$BTA\cdot H_2O$	5, 5´-bis(1H-tetrazolyl)amine monohydrate
BTA	5, 5´-bis(1H-tetrazolyl)amine
CTA	Cyanuric triazide
Asym	Asymmetric
Sym	Symmetric
Fig.	Figure
Tet.	Tetrazole

Chapter 1 Introduction

1.1 Energetic materials and nitrogen-rich energetic materials

1.1.1 Energetic materials

Energetic materials are defined as those with high enthalpies of formation, which can release gases and energy stored within their molecular structures upon stimulus by heat, impact, shock, spark, etc.[1-3] Energetic materials have been used extensively for both civilian and military applications, such as air bags, fireworks, mining, munitions, anti-missile decoy flares.[4-8] Based on different functions, they may be broadly classified into three categories: pyrotechnics, propellants (including gas generators) and explosives. Pyrotechnics, which undergo combustion at visibly observable rates, usually generate coloured smoke/light and noise. Propellants undergo more rapid combustion than pyrotechnics but do not detonate, usually accompanied by a crackling sound and flames. Explosives involve fast detonation, giving rise to shock wave and the release of a large amount of energy.[2]

1.1.2 Nitrogen-rich energetic materials

Conventional energetic materials, such as trinitrotoluene (TNT), 1,3,5-trinitrohexahydro-1,3,5-triazine (RDX), 1,3,5,7-tetranitro-1,3,5,7-tetrazacyclooctane (HMX), which usually consist of a carbon-hydrogen fuel component and an oxygen-rich, nitro-oxidizing component, release most of their energy from oxidation of the carbon backbones.[9] Recently, growing scientific interests have been directed towards the design and synthesis of nitrogen-rich energetic materials,[10-13] which are made up with only nitrogen, carbon and hydrogen atoms. Such materials have the potential to release substantial energy during decomposition because they could convert the energetic N-N and C-N bonds to form molecular nitrogen, which pose significantly lower environment and safety hazards than conventional energetic materials.[14,15]

In 2004, Eremets *et al.*[16] synthesized the diamond-like nitrogen, in which all the nitrogen atoms were linked by single bonds, directly from nitrogen gas at temperatures above 2,000 K and pressures above 110 giga-pascal (GPa). This material could be considered energetic because there is a large energy difference between the single bonded and triple bonded nitrogen. Therefore, the high pressure technique provides a new and green way of synthesizing energetic materials. However, diamond-like nitrogen could not been recovered at ambient pressure and the experimental condition of synthesizing this material was too extreme. Based on this, it would be worthwhile to explore conditions of synthesizing materials with similar single bonded nitrogen network at lower temperature and pressure. Therefore, in the next several sections, I will discuss the principles of the high-pressure technique and its implications on the study of energetic materials.

1.2 High-pressure science and technology

1.2.1 High-pressure phenomena

Pressure, which could span over 60 orders of magnitude in the universe,[17] is a thermodynamic function of paramount importance for chemical equilibrium and chemical kinetics.[18] By reducing the volume available for the system, the free-energy change related to the compression can be in excess of 10 eV. Due to pressure-induced changes in chemical affinities, the reactivities of elements and compounds that we are familiar with at ambient conditions are completely altered, and totally new classes of materials with unusual chemical and physical properties can be formed.[19] For example, superhard material could be formed from carbon dioxide at high pressures,[20] iodine[21] and oxygen[22] will undergo the insulator-to-metal transition at high pressures. Moreover, the application of pressure provides an ideal method to delicately tune electronic, magnetic, structural, and vibrational properties for testing fundamental theory and a range of applications.[19]

1.2.2 Diamond anvil cell

In order to generate high pressure, devices, such as diamond anvil cells (DAC), which could generate pressures up to ~360 GPa, were developed and improved in the past two decades.[23,24] Diamonds are known as the hardest material in nature and could be used as anvils to generate high pressure. Moreover, diamonds are transparent to a wide spectral range of electromagnetic radiation, therefore, various probes, such as vibrational spectroscopy and X-ray diffraction, could be used to characterize properties of materials at high pressures *in situ*.[25]

The basic principle of the DAC is very simple and is shown in Fig. 1.1. A stainless steel gasket, which is drilled with a hole at the center and used to contain the sample, is sandwiched between a pair of identical and brilliant-cut diamond anvils, which are mounted on two tungsten carbide seats. The size of the tips of the diamond anvils are from 100 to 700 µm, which decide the maximum pressure the system could reach.

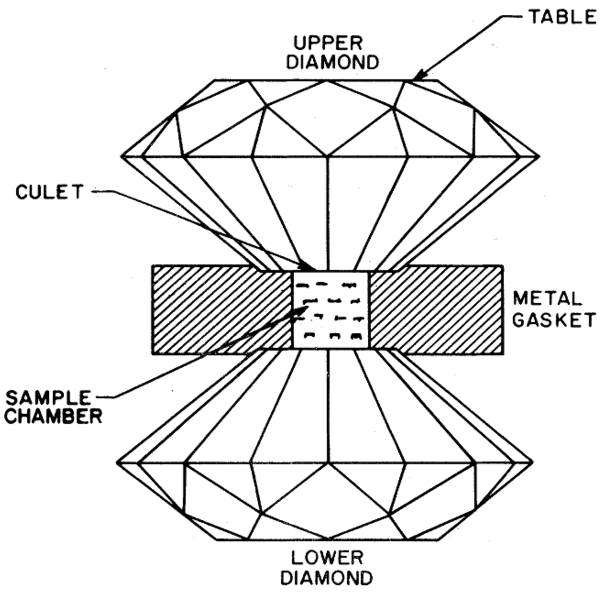

Fig. 1.1 Opposed diamond anvil configuration, with a metal gasket for sample confinement in a pressure medium; the basic part of the DAC. (Adapted form Ref. 23)

1.2.3 The ruby pressure gauge

In order to measure the pressure reliably and accurately, ruby fluorescence method is well established.[26-28] Ruby is Al_2O_3 doped with Cr^{3+}, which emits luminescent peaks R_1 and R_2 when excited by lasers. The position of R_1 peak is very sensitive to pressures and an equation can be used to describe the relationship between pressure and the wavelength of R_1 line.

$$P = \frac{1904}{B}\left[\left(1+\frac{\Delta\lambda}{694.24}\right)^{B} - 1\right] \qquad (1.1)$$

where P is the pressure in GPa and $\Delta\lambda$ is the difference between the wavelength of the ruby R_1 line at pressure P and that at ambient pressure. For example, the difference between the wavelength of ruby R_1 fluorescence spectra at 0 GPa and 4.9 GPa were used to determine the high pressure. (Fig. 1.2) The parameter B equals to 7.665 for quasi-hydrostatic conditions, and equals to 5 for non-hydrostatic conditions.[28] Using this method, the resolution of the pressure can be achieved to ± 0.05 GPa.

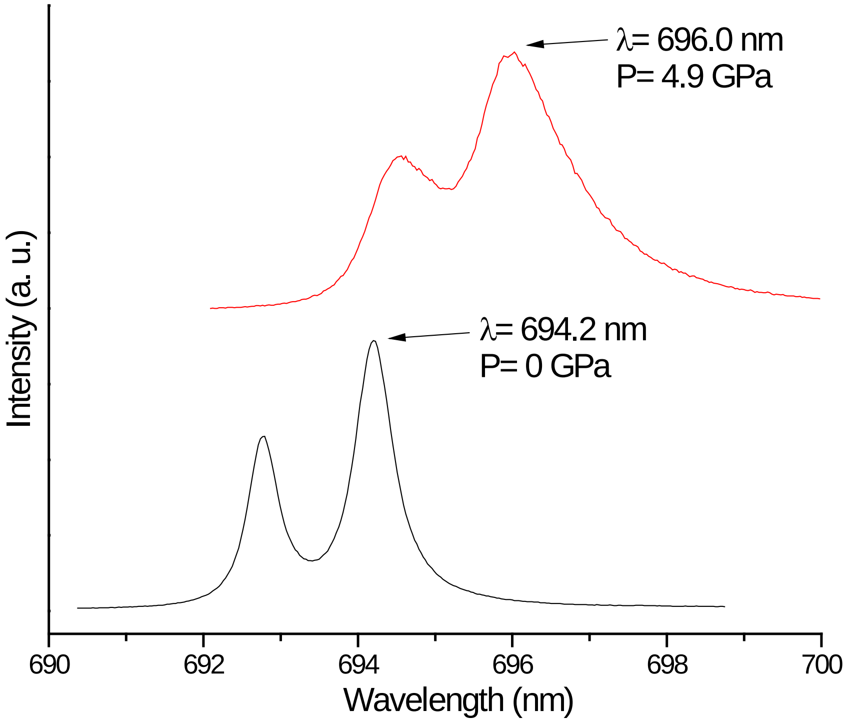

Fig. 1.2 Ruby R_1 fluorescence spectra at 0 GPa (in black) and at 4.9 GPa (in red) at room temperature.

1.2.4 High-pressure characterization tools

In this study, vibrational spectroscopy and powder X-ray diffraction are used to characterize the high-pressure properties of materials.

1.2.4.1 High-pressure vibrational spectroscopy

Both Raman and IR spectroscopy are very powerful tool in terms of providing information regarding molecular structures, chemical bonding and changes in the circumstances. However, they have different selection rules. Raman is based on the changes of polarizability of a molecule while IR depends on the changes of molecular dipole moment. So usually a mode could be either Raman-active or IR-active, or active to both probes. In very rare circumstances, it could be inactive to both Raman and IR. Therefore, for non-silent molecular vibrations, IR and Raman spectroscopy are supplementary to each other by providing a whole picture of molecular vibrations.

A customized Raman micro-spectroscopy system was used to collect the Raman spectra. The photo of this Raman system is shown in Fig. 1.3. A single longitudinal mode, diode pumped solid state (DPSS) green laser with wavelength 532.10 nm was used as the excitation source. The laser was focused to < 5 μm on the sample by a 20× Mitutoyo objective. The Raman signal was detected with backscattering geometry by the same objective lens. The Rayleigh scattering was removed by a pair of notch filters. The scattered light was then dispersed using an imaging spectrograph equipped with a 1200 lines/mm grating achieving a 0.1 cm^{-1} resolution. The Raman signal was recorded using an ultrasensitive, liquid nitrogen cooled, back-illuminated, charge-coupled device (CCD) detector from Acton. The system was calibrated by neon lines with an uncertainty of ± 1 cm^{-1}.[29]

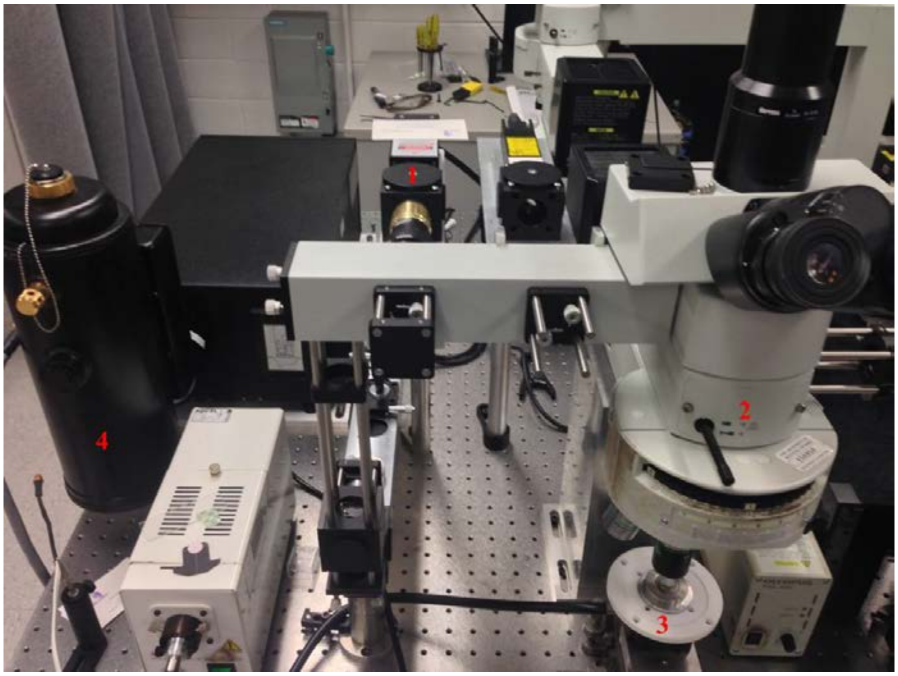

Fig. 1.3 Photo of the customized Raman micro-spectroscopy system. 1: DPSS green laser; 2: Mitutoyo objective; 3: sample stage; 4: CCD dectector.

A customized IR microspectroscopy system was used for all room-temperature IR absorption measurements. Figure 1.4 shows the schematic diagram of the system. A commercial Fourier transform infrared (FTIR) spectrometer from Bruker Optics Inc. (Model Vertex 80v) equipped with Globar mid-IR light source constituted the main component of the micro-IR system, which was operated under a vacuum of < 5 mbar, such that the absorption by H_2O and CO_2 was efficiently removed. A collimated IR beam was directed into a relay box through a KBr window on the spectrometer. The beam was then focused onto the sample in the DAC by an iris optics and 15× reflective objective lens with a numerical aperture of 0.4. The size of the IR beam was set to be identical to the entire sample size (e.g., ~ 130 μm) by a series of iris apertures. The transmitted IR beam was collected using another identical reflective objective as the condenser, and was directed to a wide-band mercury cadmium telluride (MCT) detector equipped with a ZnSe window that allows measurements in the spectral range of 600 to 12000 cm^{-1}. The customized spectroscopy system also allows IR measurements in the reflection mode using reflective optics via the optical path shown in Figure 1.4. All measurements were undertaken in transmission (or absorption) mode. A resolution of 4 cm^{-1} and 512 scans were applied for each spectrum measurement, achieving an excellent signal-to-noise ratio. The reference spectrum, i.e., the absorption of diamond anvils loaded with KBr but without any sample, was later divided as background from each sample spectrum to obtain the absorbance.[29]

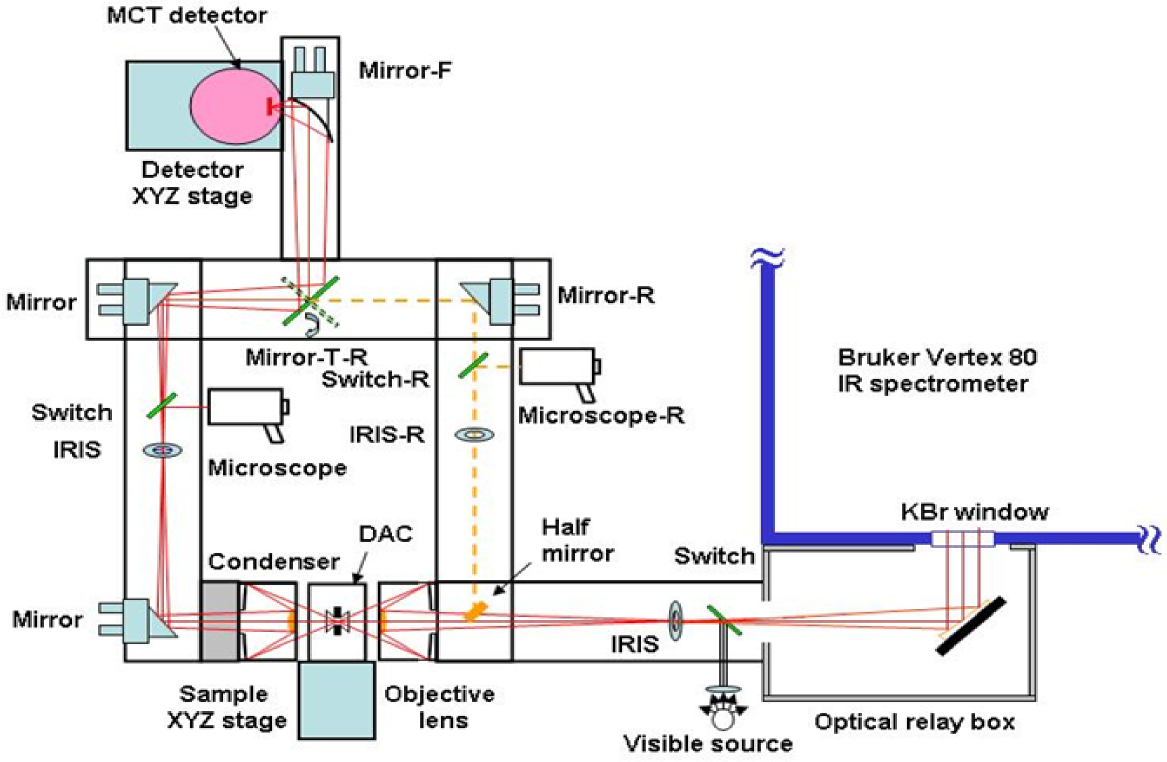

Fig. 1.4 Schematic diagram of the IR micro-spectroscopy system. All major optical components are labeled. (Adopted from Ref. 29)

1.2.4.2 High-pressure powder X-ray diffraction facility

Different from IR and Raman spectroscopy, which can provide us information on the molecular vibrations or the microenvironment changes, XRD focuses more on the crystal structure. In high-pressure studies, due to the anvils of DAC and small sample sizes, X-ray diffraction measurements can only be performed with intense high energy X-ray beam and very small beam size (e.g., tens of microns), which can hardly be achieved in local X-ray diffraction facilities using Co, Cu, and Mo as the excitation sources. Therefore, synchrotron radiation source becomes the best choice for high-pressure research due to its wide energy range, brightness and the fine beam size.[30]

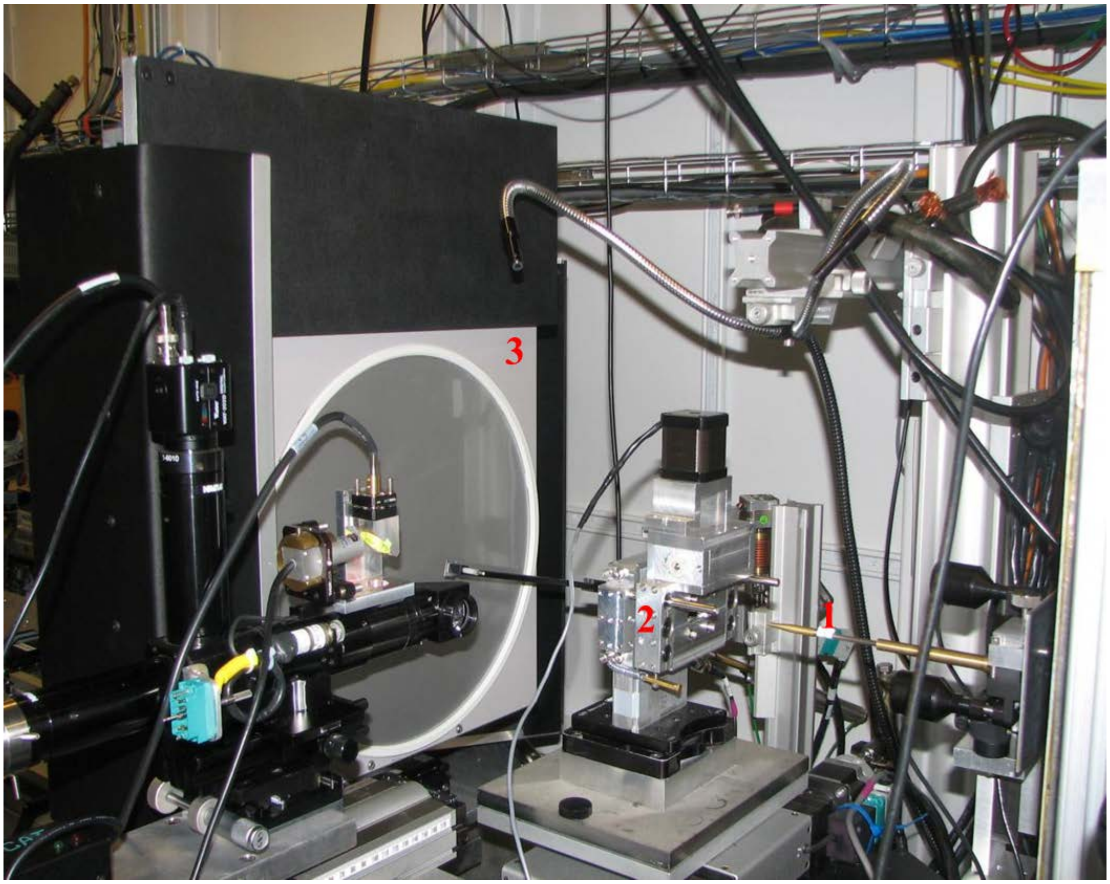

Fig. 1.5 Photo of the powder X-ray diffraction facility. 1: X-ray beam; 2: sample stage; 3: MAR3450 image plate.

The HPCAT 16-BM-D, shown in Fig. 1.5, is a general purpose x-ray diffraction beamline for samples under high pressure and high temperature, typically in DACs. The X-ray energy can be chosen by Si (111) double crystal monochromator from the APS bending magnet beam and the energy range covers 6-45 keV normally. The monochromatic X-ray beam is focused by Kirkpatrick-Baez (KB) type mirrors both in vertical and horizontal dimensions, which normally provide 5 mm (H) x 12 mm (V) beam size (FWHM) at the sample. Using a large area detector (typically MAR3450 Image Plate or MARCCD on request) powder and single crystal diffraction experiments are commonly conducted. On the precisely aligned diffractometer center within sub-micron to a micron precision, various types of DACs assemblies housed in cryostat and/or external resistive heater are mounted to provide precise diffraction information.[31]

1.3 High-pressure studies of energetic materials

Usually, the shock wave caused by the decomposition of energetic materials will lead to high pressure and high temperature, which will often induce solid phase transitions or initiate chemical reactions.[3] Thus, it is very important to model and understand their characteristics and behaviour under the extreme conditions of their operation.[32] Up to now, extensive papers of experimental and computational methods to characterize decomposition, combustion, and detonation of energetic materials have been published. Three general methods have been used to study these materials at high pressures, which are computational studies, dynamic shock-wave studies, and direct static compression, respectively. Allowing a wide range of pressures and temperatures to be explored easily, computational studies are particularly useful to the study of energetic materials, and could provide detailed information about reaction rates and possible mechanisms under extreme conditions. Shock-wave method involves the use of explosive charge or a gas gun that fires a high-velocity projectile at the material under study. Direct static compression typically involves compression of the sample in a DAC, and has the potential to provide information about changes in lattice parameters, equations of state, the response of intermolecular interactions to pressure,[33,34] which was employed in this thesis.

Conventional energetic materials, such as RDX[33,35,36], HMX[37,38] and hexanitrohexaazaisowurtzitane (CL-20)[1,39], have been studied under high pressure extensively during the past years. Most of them will undergo phase transformations under high pressure, and exhibit different sensitivity to stimulus, chemical reactivity, crystal density and thermal stability.[3] Recent high-pressure studies on nitrogen-rich energetic materials showed similar result that new polymorphs existed under high pressure.[9,14,40-43] For example, polymerization of nitrogen in sodium azide could take place at above 50 GPa.[44] Therefore, it is promising to synthesize new energetic materials with single-bonded nitrogen network using high pressure as a tool to tune the structure.

1.4 Objective and thesis structure

Among the many nitrogen-rich energetic materials mentioned above, four materials, 5-aminotetrazole (5-ATZ), 5-methyltetrazole (5-MTZ), 5, 5´-bis(1H-tetrazolyl)amine monohydrate ($BTA\cdot H_2O$), cyanuric triazide (CTA) were studied under high pressure by vibrational spectroscopy and powder X-ray diffraction. The main theme of my thesis is to examine the structures and properties of those four nitrogen-rich materials under high pressure to see whether those precursors will form polymeric nitrogens. All these four materials have been studied extensively for their decomposition mechanisms. However, the high-pressure behaviour of those four materials have not been examined and understood. Therefore, the understanding of the structures of those precursors is of great importance for the exploration of energetic materials.

Chapter 2 will mainly discuss the high-pressure studies of two tetrazole derivatives, 5-ATZ and 5-MTZ, respectively. Chapter 3 and chapter 4 focus on the high-pressure study of $BTA\cdot H_2O$ and CTA, respectively. In order to better understand the high-pressure behavior of CTA, s-triazine, which has the similar structure with CTA, was also studied in chapter 4.

1.5 References

(1) Millar, D. I. A.; Maynard-Casely, H. E.; Kleppe, A. K.; Marshall, W. G.; Pulham, C. R.; Cumming, A. S. *Cryst. Eng. Comm.* **2010**, *12*, 2524.

(2) Akhavan, J. *The Chemistry of Explosives*, Cambridge, UK: Royal Society of Chemistry, **2004**.

(3) Millar, D. I. A.; Marshall, W. G.; Oswald, I. D. H.; Pulham, C. R. *Crystallogr. Rev.* **2010**, *16*, 115.

(4) Gao, H.; Shreeve, J. M. *Chem. Rev.* **2011**, *111*, 7377.

(5) Li, Z.; Xie, S.; Zhang, J.; Feng, J.; Wang, K.; Zhang, T. *J. Chem. Eng. Data* **2012**, *57*, 729.

(6) Klapötke, T. M.; Stierstorfer, J. r.; Wallek, A. U. *Chem. Mater.* **2008**, *20*, 4519.

(7) Badgujar, D. M.; Talawar, M. B.; Asthana, S. N.; Mahulikar, P. P. *J. Hazard. Mater.* **2008**, *151*, 289.

(8) Huynh, M. H. V.; Hiskey, M. A.; Chavez, D. E.; Naud, D. L.; Gilardi, R. D. *J. Am. Chem. Soc.* **2005**, *127*, 12537.

(9) Ciezak, J. A. *Propellants Explos. Pyrotech.* **2010**, *35*, 550.

(10) Peiris, S. M.; Russell, T. P. *J. Phys. Chem. A* **2003**, *107*, 944.

(11) Klapötke, T. M.; Sabaté, C. M. *Chem. Mater.* **2008**, *20*, 1750.

(12) Srinivas, D.; Ghule, V. D.; Tewari, S. P.; Muralidharan, K. *Chem. Eur. J.* **2012**, *18*, 15031.

(13) Dippold, A. A.; Klapotke, T. M.; Oswald, M. *Dalton Trans.* **2013**, *42*, 11136.

(14) Behler, K. D.; Ciezak J., J. A.; Sausa, R. C. *J. Phys. Chem. A* **2013**, *117*, 1737.

(15) McWilliams, R. S.; Kadry, Y.; Mahmood, M. F.; Goncharov, A. F.; Ciezak J., J. *J. Chem. Phys.* **2012**, *137*, 054501.

(16) Eremets, M. I.; Gavriliuk, A. G.; Trojan, I. A.; Dzivenko, D. A.; Boehler, R. *Nat. Mater.* **2004**, *3*, 558.

(17) Weir, C. E.; Lippincott, E. R.; Valkenburg, A. V.; Bunting, E. N. In *J. Res. Natl. Bur. Stand.* **1959**, *63*, 55.

(18) Schettino, V.; Bini, R. *Phys. Chem. Chem. Phys.* **2003**, *5*, 1951.

(19) Hemley, R. J. *Annu. Rev. Phys. Chem.* **2000**, *51*, 763.

(20) Iota, V.; Yoo, C. S.; Cynn, H. *Science* **1999**, *283*, 1510.

(21) Riggleman, B. M.; Drickamer, H. G. *J. Chem. Phys.* **1963**, *38*, 2721.

(22) Akahama, Y.; Kawamura, H.; Häusermann, D.; Hanfland, M.; Shimomura, O. *Phys. Rev. Lett.* **1995**, *74*, 4690.

(23) Jayaraman, A. *Rev. Mod. Phys.* **1983**, *55*, 65.

(24) Jeanloz, R. *Aunu. Rev. Phys. Chem.* **1989**, *40*, 237.

(25) Tapper, R. J. *Rep. Prog. Phys.* **2000**, *63*, 1273.

(26) Mao, H. K. *Science* **1978**, *200*, 1145.

(27) Xu, J. A.; Mao, H. K.; Bell, P. M. *Science* **1986**, *232*, 1404.

(28) Mao, H. K.; Xu, J.; Bell, P. M. *J. Geophys. Res-Solid* **1986**, *91*, 4673.

(29) Dong, Z. *Ph. D. thesis*, **2012**.

(30) Hemley, R. J.; Mao, H. K.; Struzhkin, V. V. *J. Synchrot. Radiat.* **2005**, *12*, 135.

(31) HPCAT 16BMD User Manual.

(32) Pulham, C. R.; Millar, D. I. A.; Oswald, I. D. H.; Marshall, W. G. *High-Pressure Crystallography*: *From fundamental Phenomena to Technological Applications-NATO Science for Peace and Security Series B: Physics and Biophysics;* Springer, New York, 2010; pp 447-457.

(33) Fabbiani, F. P. A.; Pulham, C. R. *Chem. Soc. Rev.* **2006**, *35*, 932.

(34) Shaw, R. W.; Brill, T. B.; Thompson, D. L. *In Overviews Of Recent Research On Energetic Materials*, Advanced Series in Physical Chemistry, World Publishing, Singapore, Vol. 16, 2005.

(35) Oswald, I. D. H.; Millar, D. I. A.; Davidson, A. J.; Francis, D. J.; Marshall, W. G.; Pulham, C. R.; Cumming, A.; Lennie, A. R.; Warren, J. E. *High Pressure Res.* **2010**, *30*, 280.

(36) Dreger, Z. A.; Gupta, Y. M. *J. Phys. Chem. B* **2007**, *111*, 3893.

(37) Yoo, C.-S.; Cynn, H. *J. Chem. Phys.* **1999**, *111*, 10229.

(38) Sorescu, D. C.; Rice, B. M.; Thompson, D. L. *J. Phys. Chem. A* **1999**, *103*, 989.

(39) Russell, T. P.; Miller, P. J.; Piermarini, G. J.; Block, S. J. Phys. Chem. **1993**, 97, 1993.

(40) Ciezak, J. A. *Propellants Explos. Pyrotech.* **2010**, *35*, 373.

(41) Ciezak, J. A. *Propellants Explos. Pyrotech.* **2010**, *35*, 24.

(42) Ciezak, J. A. *Propellants Explos. Pyrotech.* **2011**, *36*, 446.

(43) Ciezak, J. A. *AIP Conf. Proc.* **2012**, *1426*, 1424.

(44) Eremets, M. I.; Popov, M. Y.; Trojan, I. A.; Denisov, V. N.; Boehler, R.; Hemley, R. J. *J. Chem. Phys.* **2004**, *120*, 10618.

Chapter 2 *In situ* high-pressure study of 5-aminotetrazole and 5-methyltetrazole by Raman and IR spectroscopy

2.1 Introduction

Diamond-like polymeric nitrogen network, in which all the nitrogen atoms were linked by the N-N single bonds, was synthesized directly from molecular nitrogen at pressures above 110 GPa and temperatures above 2,000 K by M. Eremets *et al.*[1]. It is considered as a high energy density material because different nitrogen allotropes exhibit a uniquely large difference in energy between the single bond and the triple bond, and therefore, a large amount of energy will be released by transformation from the single-bonded form to N_2. However, the polymeric nitrogen phase is only metastable under the above mentioned extreme conditions such that it transforms back to molecular nitrogen at ambient conditions. Therefore, efforts have been made to synthesize the recoverable polymeric nitrogens using different precursors under different conditions.[2-4]

Recent years, new energetic materials, especially nitrogen-rich or polynitrogen compounds[5-9], such as tetrazole-containing compounds or tetrazole salts[10-13] have attracted increasing attention. Due to their own aromatic ring systems, tetrazoles often release large amounts of energy by decomposition and have good thermal stability as well as the high nitrogen content.[14] Thus, the tetrazole ring could allow the preparation of primary[15,16] and secondary[12,13] explosives with high performance. In addition, tetrazoles produce more nitrogen gas per gram than most of the high energy materials, resulting in inherently cooler combustion products, which is an attractive feature for gun propellants and gas generators.[17]

Containing 82.3% nitrogen by weight and used as gas generator agent for air bag inflator[18,19] and solid propellant[20], 5-aminotetrazole (5-ATZ) has received extensive experimental and theoretical studies about its decomposition mechanism at high temperature[21-25]. However, the existing experimental data on the thermal decomposition of the 5-ATZ are often contradictory. Under ambient pressure, three phases of 5-ATZ have been known up to its melting point, among which only one phase has been structurally characterized. Phase I was determined by Fujihisa *et al.*[26] by powder XRD, Rietveld analysis and density functional theory calculation, because of the difficulty of getting single crystal of anhydrous 5-ATZ. It crystallizes into an orthorhombic cell under ambient conditions with space group $P2_12_12_1$ (D_2^4) and cell parameters a = 5.088 Å, b = 3.664 Å, c = 18.040 Å, and V = 336.3 Å^3, with molecular structure shown in Fig. 2.1 (A). Different from the 5-ATZ molecules in gas phase, which are mainly in 2H-form[27,28], molecules in the crystal are in 1H-form[26], consistent with previous published papers[29] and is shown in Fig. 2.2. Moreover, 5-ATZ molecules are also known to be linked by extensive hydrogen bonds, which have a great influence on the stability and density for energetic materials. When 5-ATZ had been heated at 448 K after 13 h and 100 h, phase II and phase III could be observed by powder XRD, but the structures had not been solved.[30]

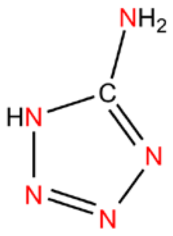

Fig. 2.1 (A) Molecular structure of 5-ATZ

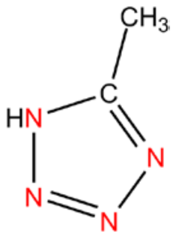

Fig. 2.1 (B) Molecular structure of 5-MTZ

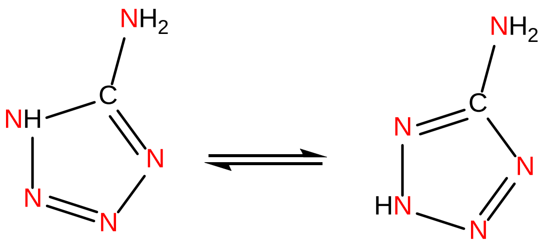

Fig. 2.2 1H-form and 2H-form of 5-ATZ

Previous research on materials with hydrogen bond networks showed that hydrogen bonds played an important role in altering the compressibility, stability as well as the reactiveness under high pressure.[31-33] In order to minimize the effect of hydrogen bonds on the high pressure behavior of tetrazole ring, another tetrazole derivative 5-methyltetrazole (5-MTZ), which replaces the amino group in 5-ATZ by a methyl group and has weaker hydrogen bonds, was studied as a comparison. Under ambient conditions, 5-MTZ crystallizes into a monoclinic cell with space group Cc and cell parameters a = 4.586 Å, b = 12.843 Å, c = 9.767 Å, and V = 413.9 Å^3.[34] Its molecular structure is shown in Fig. 2.1 (B).

Since high-pressure technique has been demonstrated an effective approach in greatly increasing the electronic density so as to trigger chemical reactions, especially when unsaturated chemical bonds are present[35]. Therefore, we could use high pressure as a driving force to break the N=N bonds and form N-N bonds between adjacent molecules in order to synthesize polymeric nitrogens. In this study, we report the first *in situ* high-pressure Raman and IR measurements on 5-ATZ and 5-MTZ, which were compressed up to about 57 GPa in DACs. Interestingly, no phase transitions were found for 5-ATZ while four phase transitions were observed for 5-MTZ during the whole investigated pressure range.

2.2 Experimental Section

2.2.1 Sample preparation

5-ATZ with ~98% purity was purchased from Santa Cruz Biotechnology, and 5-MTZ with ~97% purity was purchased from Sigma-Aldrich. Both chemicals were used without further purification. A symmetrical DAC with two type-I diamonds with 250 μm culets was used for the high-pressure Raman measurements, while a pair of type-II diamonds with a culet size of 350 μm was used for the IR measurements. 5-ATZ was loaded in a MBraun LAB Master 130 glovebox filled with N_2 atmosphere (< 10 ppm O_2 and H_2O) and without any fluid pressure-transmitting medium to accommodate the hygroscopicity of the material. One ruby (Cr^{3+} doped α-Al_2O_3) chip as the pressure calibrant was carefully placed inside the sample chamber before the sample was loaded. The pressure was determined by using the R_1 ruby fluorescence line shift with an accuracy of ± 0.05 GPa under quasi-hydrostatic conditions.[36] For IR measurements, spectral quality KBr powders were also loaded into the DAC used both as pressure transmitting medium and to dilute the sample.

2.2.2 High-pressure Raman measurements

A customized Raman micro-spectroscopy system was used to collect the Raman spectra. A single longitudinal mode, diode pumped solid state (DPSS) green laser with wavelength 532.10 nm was used as the excitation source. The laser was focused to < 5 μm on the sample by a 20× Mitutoyo objective. The Raman signal was detected with backscattering geometry by the same objective lens. The Rayleigh scattering was removed by a pair of notch filters. The scattered light was then dispersed using an imaging spectrograph equipped with a 1200 lines/mm grating achieving a 0.1 cm^{-1} resolution. The Raman signal was recorded using an ultrasensitive, liquid nitrogen cooled, back-illuminated, charge-coupled device (CCD) detector from Acton. The system was calibrated by neon lines with an uncertainty of ± 1 cm^{-1}. To avoid the strong first-order Raman mode of diamond at 1334 cm^{-1}, the spectra were collected in ranges of 0-1300 cm^{-1} and 1350-3400 cm^{-1} in several collection windows. For each spectrum, a collection time of 30 s was employed, and the average laser power on the sample was maintained at ~ 30 mW.

2.2.3 High-pressure IR measurements

A customized IR microspectroscopy system was used for all room-temperature IR absorption measurements. A commercial Fourier transform infrared (FTIR) spectrometer from Bruker Optics Inc. (Model Vertex 80v) equipped with Globar mid-IR light source constituted the main component of the micro-IR system, which was operated under a vacuum of < 5 mbar, such that the absorption by H_2O and CO_2 was efficiently removed. A collimated IR beam was directed into a relay box through a KBr window on the spectrometer. The beam was then focused onto the sample in the DAC by an iris optics and 15× reflective objective lens with a numerical aperture of 0.4. The size of the IR beam was set to be identical to the entire sample size (~ 130 μm) by a series of iris apertures. The transmitted IR beam was collected using another identical reflective objective as the condenser, and was directed to a wide-band mercury cadmium telluride (MCT) detector equipped with a ZnSe window that allows measurements in the spectral range of 600 to 12000 cm^{-1}. All measurements were undertaken in transmission (or absorption) mode. A resolution of 4 cm^{-1} and 512 scans were applied for each spectrum measurement, achieving an excellent signal-to-noise ratio. The reference spectrum, i.e., the absorption of diamond anvils loaded with KBr but without any sample, was later divided as background from each sample spectrum to obtain the absorbance.

2.3 Results

2.3.1 5-ATZ

2.3.1.1 Ambient-pressure Raman and IR spectra

Raman and IR spectra were collected at ambient conditions as the starting point and are shown in Fig. 2.3. Compared to the IR study by Jonassen *et al.*[37] and Levchik *et al.*[38] on condensed phase and standard spectrum[39] of 5-ATZ, our measurements are in close agreement with theirs as can be seen from Table 2.1. We followed the assignment proposed by Jonassen *et al.*[37] and labeled the modes accordingly in Table 2.1. In addition, we also observed five Raman bands at 76, 93, 123, 138 and 147 cm^{-1} in the lattice region.

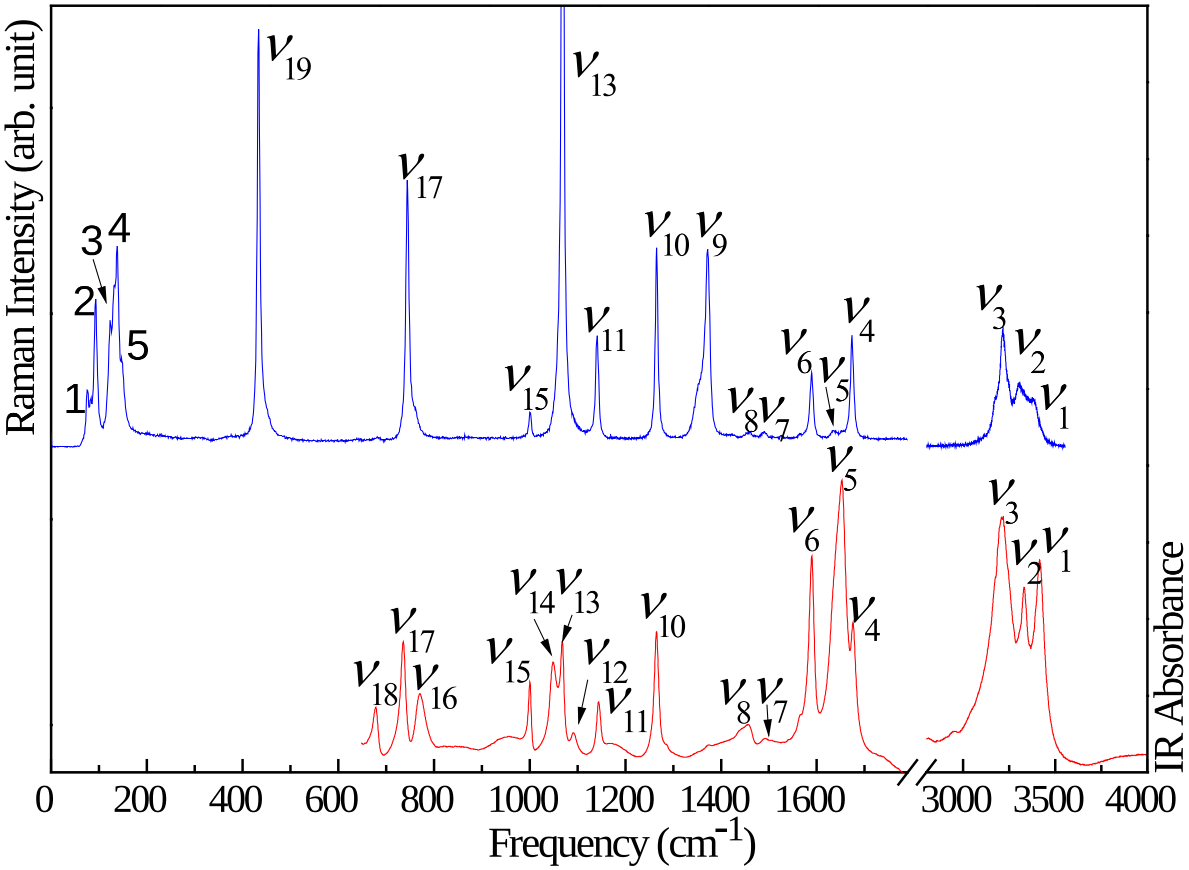

Fig. 2.3 Raman spectrum of 5-ATZ (top) in comparison with IR spectrum (bottom) in the spectral region 0-4000 cm^{-1}, both collected at near ambient pressure and room temperature. The omitted spectral regions are due to the lack of spectroscopic features. The assignment of the vibrational modes is labeled above each.

Table 2.1 Assignment and frequencies (cm^{-1}) of observed Raman and IR internal modes of 5-ATZ in comparison with reference values.

Mode	Description	This work		References	
		Raman	IR	IR[37]	IR[38]
v_1	N-H stretch	3382	3416	3390	3420
v_2	N-H stretch	3306	3331	3311	3350
v_3	Ring N-H stretch	3216	3212	3175	3200
v_4	N-H bending	1673	1675		1680
v_5	N-H bending		1652	1631	1655
v_6	Endo C=N stretch [a]	1589	1590	1585	1590
v_7	?	1490	1491		1490
v_8	N=N ring stretch	1457	1456	1439	1455
v_9	?	1372	1373		
v_{10}	Exo C-N stretch [b]	1265	1265	1263	1265
v_{11}	Ring vibration	1141	1144	1140	1145
v_{12}	Ring vibration		1092	1087	1070
v_{13}	Ring vibration	1069	1068	1064	1050
v_{14}	Ring vibration		1049	1043	
v_{15}	?	1001	1000		1000
v_{16}	N-H rocking		771	766	775
v_{17}	N-H rocking	744	736	734	740
v_{18}	?		678		
v_{19}	?	433			
5	Lattice mode	147			
4	Lattice mode	138			
3	Lattice mode	123			
2	Lattice mode	93			
1	Lattice mode	76			

[a] Endo C=N stretch refers to the CN stretching mode inside the aromatic ring.

[b] Exo C-N stretch refers to the CN stretching mode attached to the aromatic ring.

2.3.1.2 Raman spectra on compression

Starting from ambient pressure, Raman spectra of 5-ATZ were collected upon compression to 56.7 GPa with selected spectra depicted in Fig. 2.4. As can be seen, upon compression to 2.7 GPa, the intensity of mode 2 in the lattice region was strengthened slightly and mode 4 was found to split into a doublet, labeled as 4_A and 4_B, respectively. At the same time, a very weak peak (labeled as v_{13A}) appeared in the range of ring vibration modes, which was likely caused by the modification of ring structures during compression. With further compression, at 13.7 GPa, all the modes were weakened and a new mode, possibly corresponding to N-H bending v_5, began to appear. Upon subsequent compression to 19.3 GPa, all the lattice modes were significantly weakened and broadened, indicating that the structure had been disordered. In addition, above 19.3 GPa, mode v_{19} was found to split with the intensity increase of mode v_5. At the highest pressure, 56.7 GPa, the significantly weakened and broadened feature of lattice modes suggest the lattice structure had been amorphous. In addition, the ring vibration modes still persisted but other internal modes were completely depleted.

2.3.1.3 IR spectra on compression

Mid-IR spectra of 5-ATZ were collected on compression to 37.7 GPa. Selected absorption spectra as a function of pressure in the spectral region of 600-3600 cm^{-1} are depicted in Fig. 2.5 (A). Because of the weak absorbance of mode v_8 and v_9, thicker sample was used to monitor the changes in the spectral region of 1310-1590 cm^{-1} during compression, shown in Fig. 2.5 (B). At low pressures, IR patterns in the region of 600-1800 cm^{-1} showed no prominent changes upon compression. At 3.4 GPa, as can be seen from Fig. 2.5 (B), mode v_9 was strengthened significantly with increasing intensity until 19.0 GPa, accompanied by the splitting of N=N stretching mode v_8 at 8.3 GPa and subsequent weakening. All of the above evidence strongly indicated that the N=N bond was weakened by the delocalization of electrons in the tetrazole ring upon compression. With further compression to the highest pressure, at 37.7 GPa, the ring vibration features still existed but with more broadened and weakened profiles.

The most dramatic changes were observed in the region of 2400-3600 cm^{-1} for N-H stretching vibrations. Upon compression, mode v_1 and v_3, corresponding to the amino N-H stretching and ring N-H stretching mode, respectively, shifted to lower frequency. At 1.8

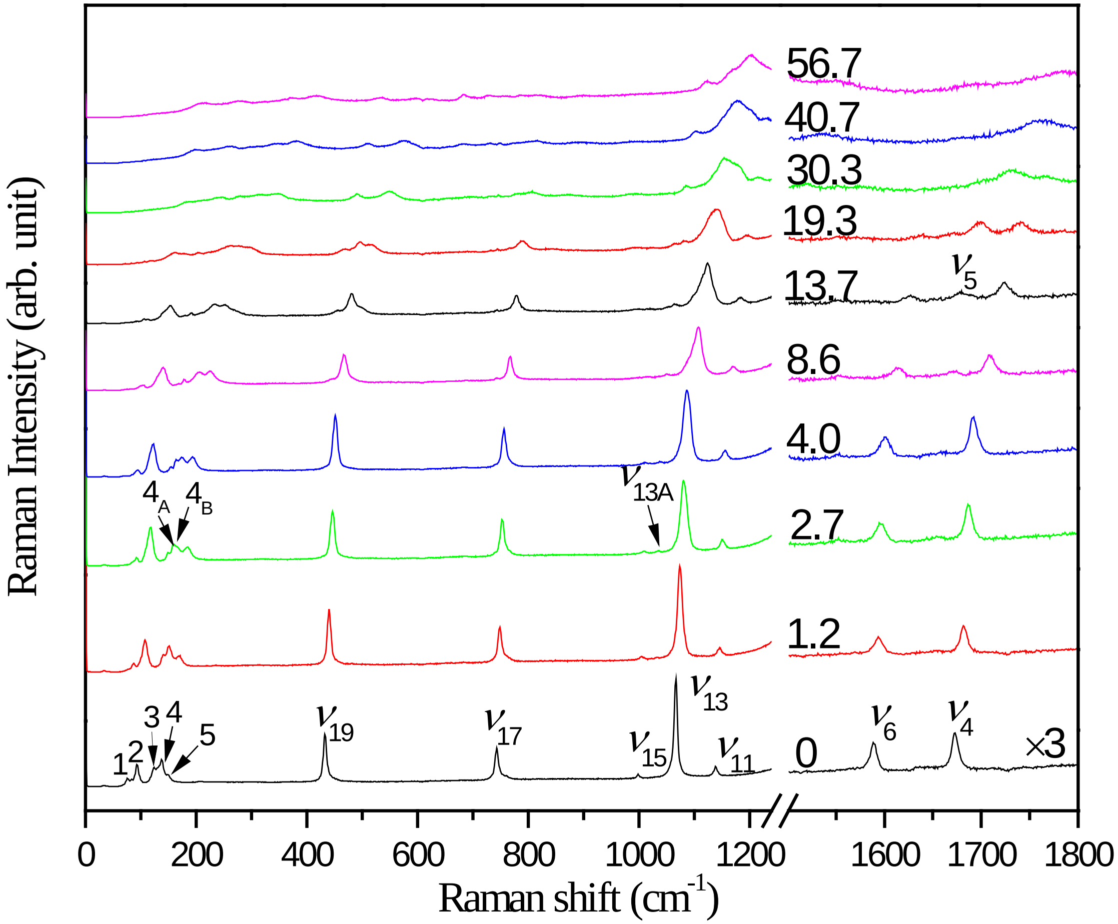

Fig. 2.4 Selected Raman spectra of 5-ATZ collected at room temperature upon compression in the region of 0-1800 cm^{-1} at pressures of 0-56.7 GPa. The spectra ranging from 1800-3600 cm^{-1} were omitted because of the weak intensity. The pressures in GPa are labeled for each spectrum. The assignments are labeled for Raman modes (see text).

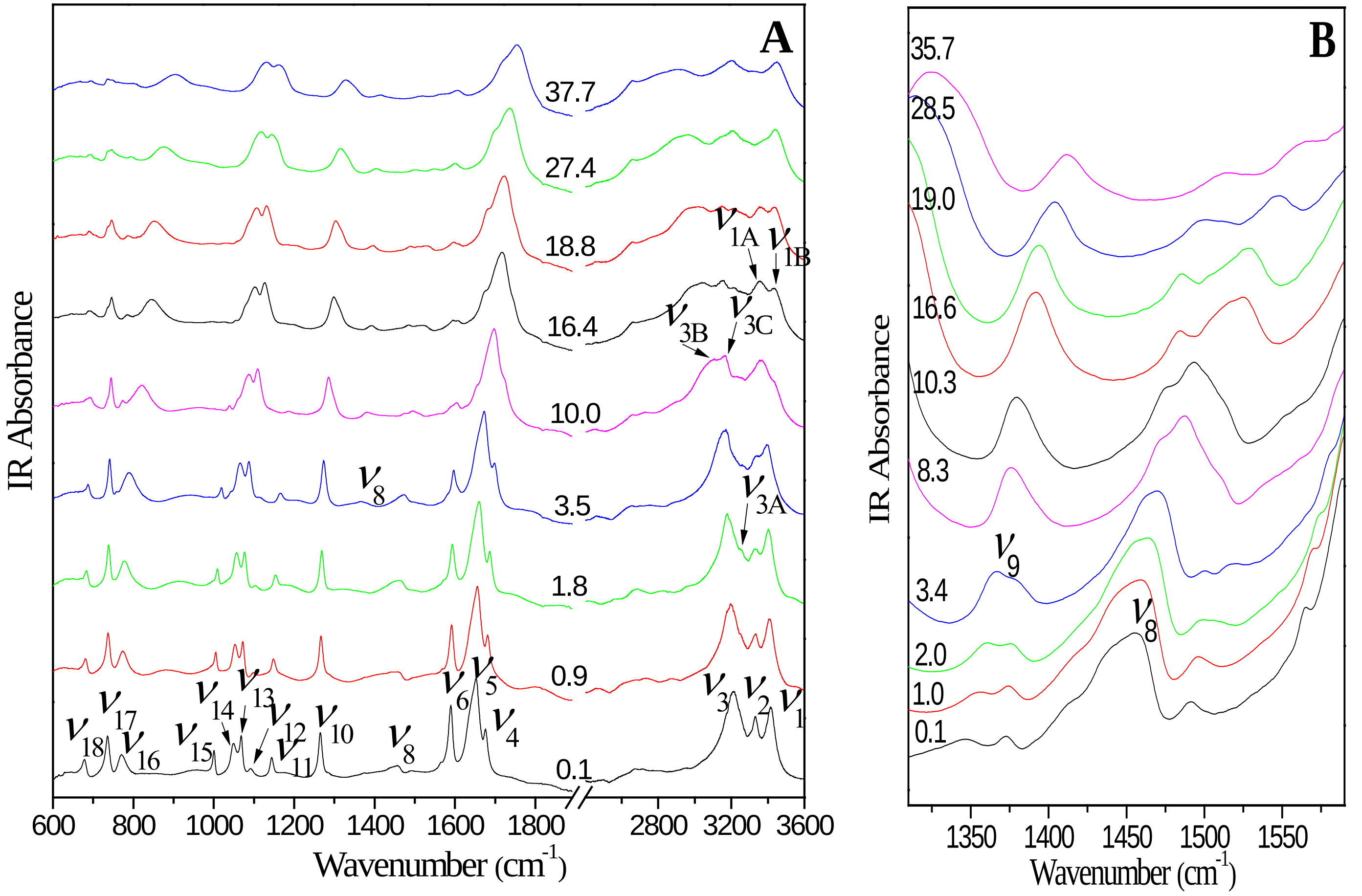

Fig. 2.5 Selected IR spectra of 5-ATZ collected at room temperature on compression in the spectral region of 600-3600 cm^{-1} (A) in the pressure region of 0.1-37.7 GPa and 1310-1590 cm^{-1} (B) in the pressure region of 0.1-35.7 GPa. The pressures in GPa are labeled for each spectrum. The assignments are labeled for IR modes (see text).

GPa, a new mode v_{3A} appeared on the shoulder of v_3. With further compression, mode v_3 was found to split into a doublet (v_{3B}/v_{3C}) and v_{3c} merged with v_{3A} at 27.4 GPa. Then v_{3B} shifted to lower frequency with pressure. Compared to the red shift of mode v_1 and v_3, mode v_2 didn't shift at first and merged with mode v_1 into a singlet at 10.0 GPa, which then split into a doublet (v_{1A}/v_{1B}) at 16.4 GPa. Above 16.4 GPa, the frequency of v_{1A} didn't change at the beginning and then slight blue shift could be observed with the decrease in intensity until it totally disappeared at 27.4 GPa. One of the components of the N-H stretching mode v_{1B}, however, shifted to higher frequency to the highest pressure.

2.3.1.4 Pressure effects on Raman and IR modes

The pressure dependence of the observed Raman and IR modes of 5-ATZ were examined by plotting the vibrational frequencies as a function of pressure as shown in Fig. 2.6 and 2.7. Generally, in the range of 0-2000 cm^{-1} all the Raman and IR modes exhibited pressure-induced blue shifts, consistent with that the bonds become stiffened upon compression. For the internal modes in this region, the frequency of these modes increased linearly with increasing pressure, indicating there were no phase transitions during compression. At the same time, the splitting of some modes was observed during compression, which was likely caused by the change of molecular orientation or the enhanced interaction between molecules within the unit cell. For the modes in the range of 2400-3600 cm^{-1}, very obvious red shifts of the ring N-H vibration mode and the amino N-H stretching mode were caused by the strengthening of intermolecular hydrogen bonds during compression. According to Fujihisa *et al.*'s XRD results and theoretical calculations of 5-ATZ[26], under high pressure, the ring N-H bond length displayed the highest increasing rate, and the amino N-H bond length increased at the beginning but almost ceased to change at 11.6 GPa, which were precisely consistent with red shifts of N-H stretching mode in this work. Then the N-H stretching modes v_{1A} and v_{1B} shifted to higher frequency, indicating that the intermolecular hydrogen bonds became weaker and the N-H bond length became shorter. Overall, the Raman and IR spectra collectively suggested that no phase transitions and chemical reactions during whole investigated pressure range.

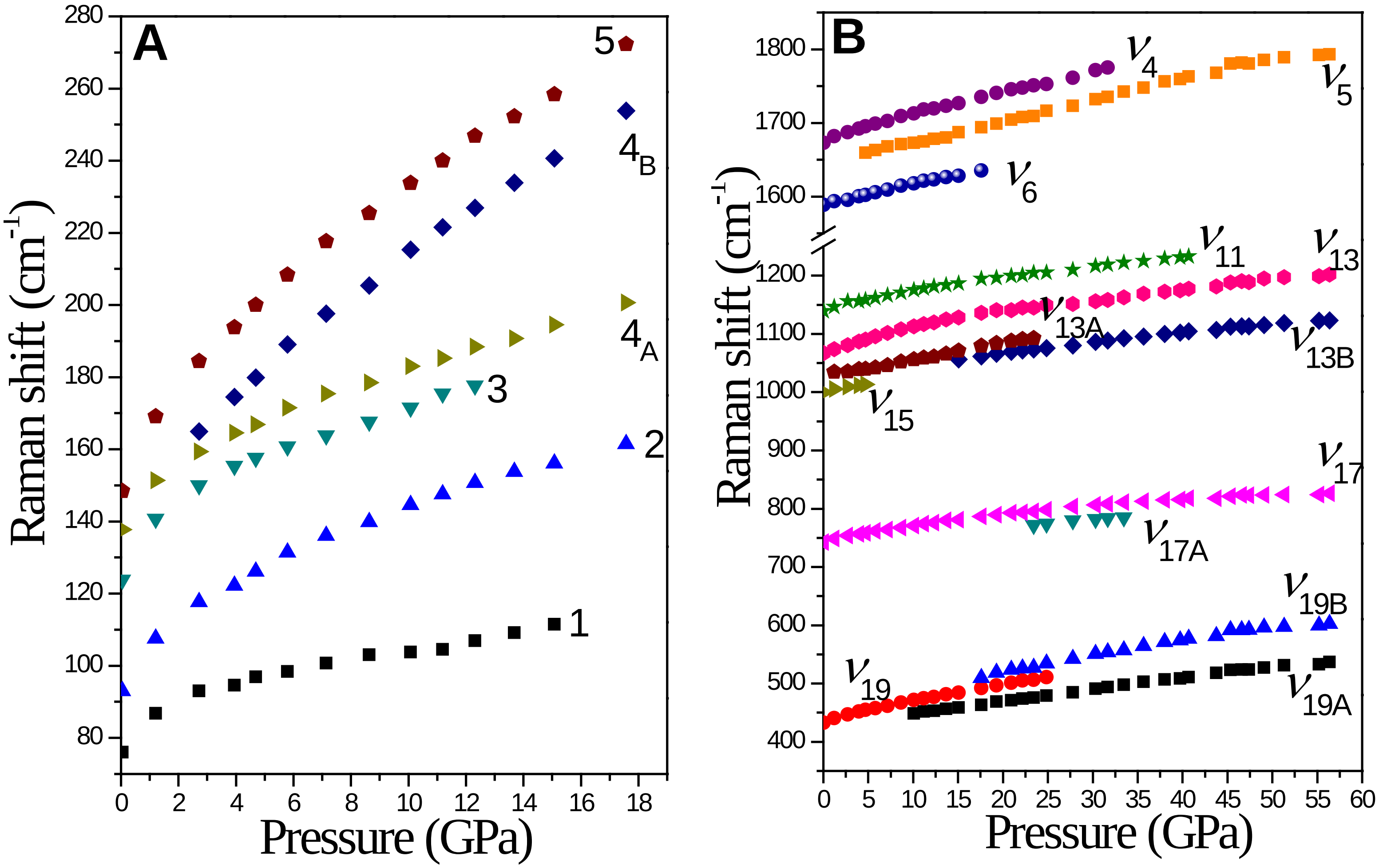

Fig. 2.6 Pressure dependence of Raman lattice modes (A) and internal modes (B) of 5-ATZ on compression. Different symbols represent Raman modes with different origins with assignments labeled.

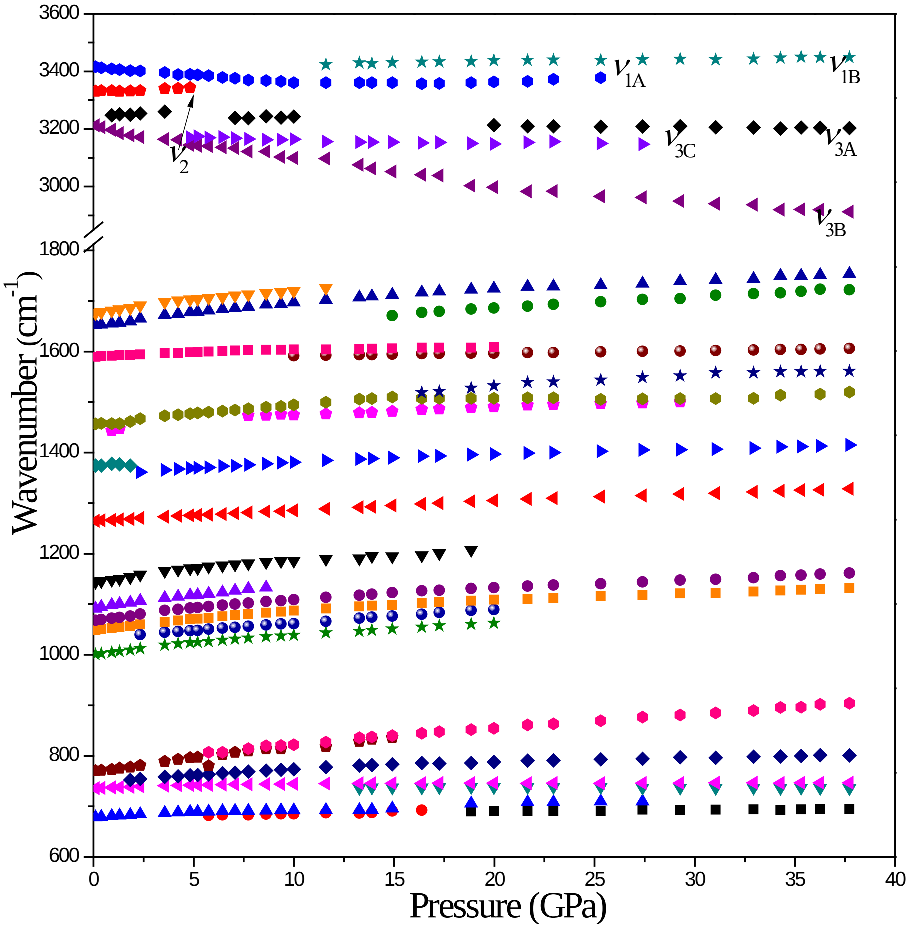

Fig. 2.7 Pressure dependence of IR modes of 5-ATZ on compression. Different symbols represent IR modes with different origins of assignments.

2.3.1.5 Raman and IR spectra on decompression

Raman and IR spectra were also collected on decompression all the way down to near-ambient pressure in order to better understand the pressure-induced structural evolutions and the high-pressure stability of 5-ATZ. Starting from 56.7 GPa, Raman spectra of 5-ATZ were collected upon decompression to near-ambient with selected spectra depicted in Fig. 2.8. Mid-IR spectra of 5-ATZ were collected from 37.7 GPa to near ambient pressure, with selected absorption spectra as a function of pressure in the spectral region of 600-3600 cm^{-1} depicted in Fig. 2.9. During decompression, very strong hysteresis could be observed and lattice modes were not recovered upon decompression to near-ambient pressure, meaning that lattice during the compression/decompression cycle was irreversible in the pressure range of 0-57 GPa. More importantly, all other modes, including the ring vibration modes, were recovered, with the difference being that the peaks were broadened and the intensity was lower, which could be associated with the disordering of crystal structures during compression. And ν_{13A}, first appeared in the compression process, didn't vanish after decompression, which was very likely due to the modification of ring structures by the high pressures.

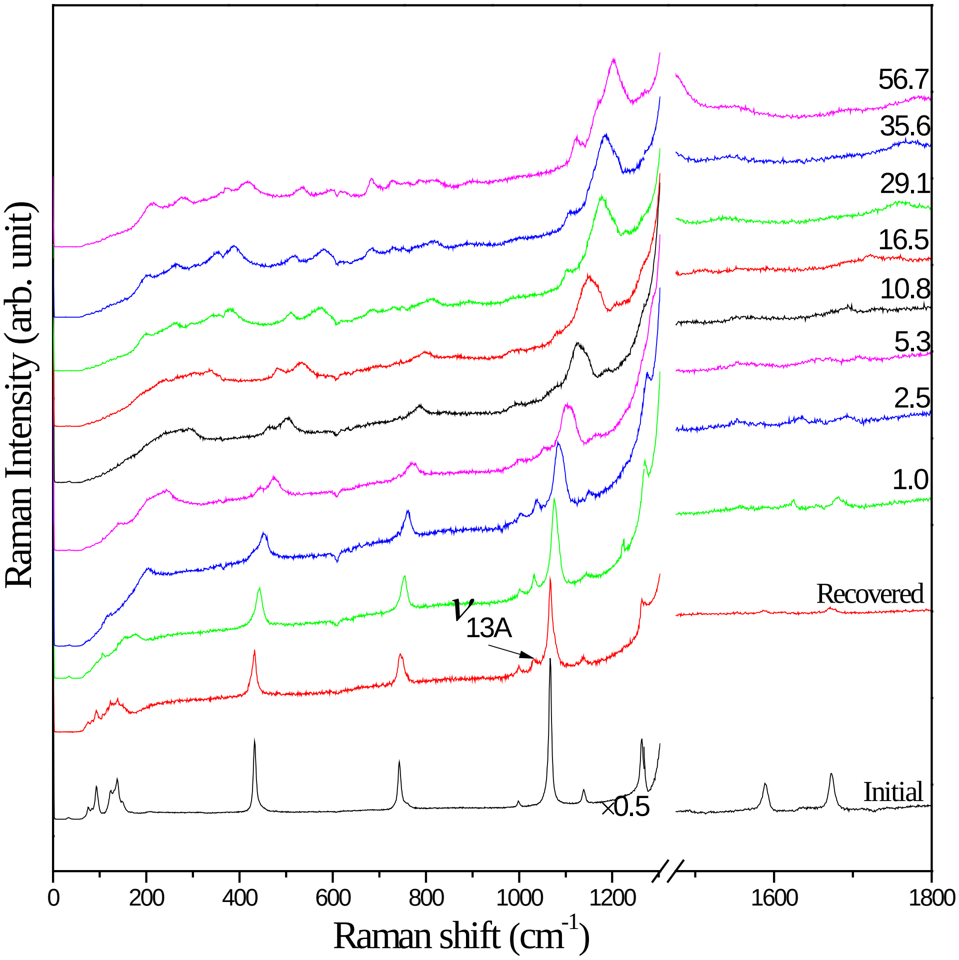

Fig. 2.8 Selected Raman spectra of 5-ATZ collected at room temperature on decompression in the region of 0-1800 cm^{-1} at pressures of 0-56.7 GPa. The pressures in GPa are labeled for each spectrum.

Similar to the Raman spectra, very strong hysteresis could be observed in the IR spectra during decompression, shown in Fig. 2.9. Compared to the compression process, at 16.1 GPa, two small new peaks (ν_{15A}/ν_{15B}) appeared at about 1000 cm^{-1} and merged to a singlet at 1.0 GPa, which may be caused by the change of orientation of 5-ATZ molecules and the weakening of hydrogen bonds during decompression. The different IR band shape and intensity could be associated with the modification of the sample thickness in the compression/decompression cycle.

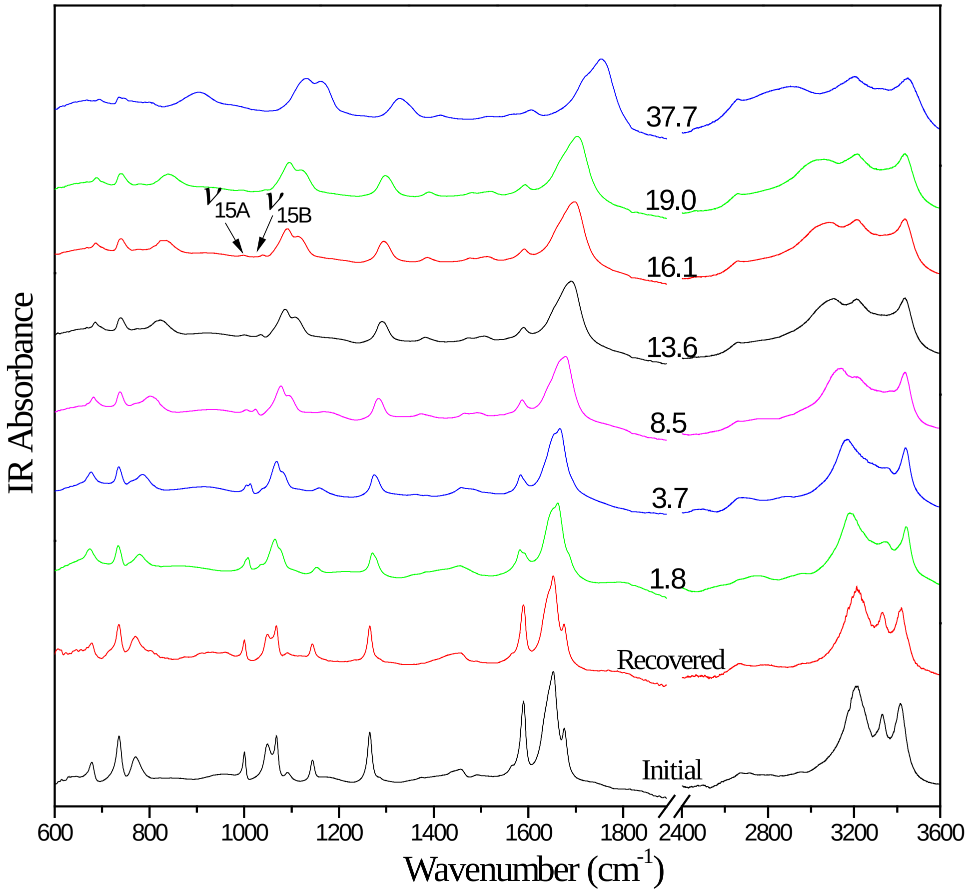

Fig. 2.9 Selected IR spectra of 5-ATZ collected at room temperature on decompression in the spectral region of 600-3600 cm^{-1} in the pressure region of 0.3-37.7 GPa. The pressures in GPa are labeled for each spectrum.

2.3.2 5-MTZ

2.3.2.1 Ambient-pressure Raman and IR spectra

Raman and IR spectra were collected at ambient conditions as the starting point and shown in Fig. 2.10. We followed the assignment proposed by Matveeva *et al.*[40] and labeled some assigned modes accordingly in Table 2.2. As can be seen, N-H stretching mode is very weak in both Raman and IR spectra, consistent with that the hydrogen bonds network is much weaker in 5-MTZ than that in 5-ATZ. As a result, in IR measurements only spectra below 1800 cm^{-1} were collected.

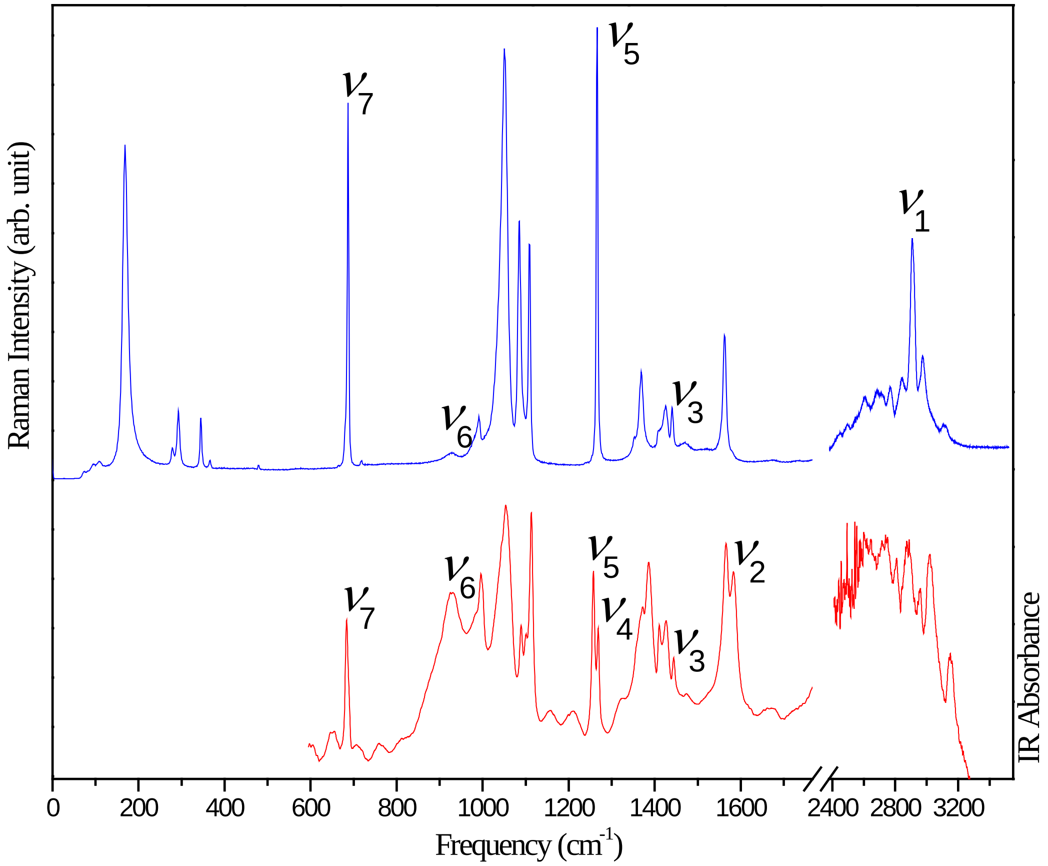

Fig. 2.10 Raman spectrum of 5-MTZ (top) in comparison with IR spectrum (bottom) in the spectral region 0-3550 cm^{-1} both collected at ambient conditions. The omitted spectral regions are due to the lack of spectroscopic features. The assignment of the vibrational modes is labeled above each.

Table 2.2 Assignment and frequencies (cm^{-1}) of observed Raman and IR internal modes of 5-MTZ in comparison with reference values.

Mode	Description	This work		References	
		Raman	IR	IR[1]	Theory[1]
ν_1	C-H stretch	2943			
ν_2	C=N stretch		1583	1580	1582
ν_3	N=N stretch	1441	1444	1440	1445
ν_4	C-N and N-N stretch,	1266	1268	1260	1261
ν_5	N-H deformation		1257	1250	1250
ν_6	N-H off-plane	929	928	920	933
ν_7	N-H off-plane	689	684	675	675

2.3.2.2 Raman spectra on compression

Starting from ambient pressure, Raman spectra of 5-MTZ were collected upon compression to 57.9 GPa with selected spectra depicted in Figs. 2.11 and 2.12 in the lattice modes region and internal modes region, respectively. As can be seen, in the lattice region, no lattice modes were observed at ambient pressure. Upon further compression, a total of five Raman modes were observed in the lattice region, labeled from 1 to 5 from low to high frequencies. When compressed to 0.8 GPa, two lattice modes at 72 and 92 cm^{-1} (labeled as 2 and 3) appeared, among which mode 3 disappeared upon compression to 2.6 GPa. Further compression to 6.6 GPa resulted in the appearance of another two lattice modes at 116 and 181 cm^{-1} (labeled as 1 and 4). Additional lattice mode at 252 cm^{-1} (labeled as 5) was observed upon subsequent compression to 29.7 GPa. Each of the occurrences of a new lattice mode indicates a possible phase transition. For the internal modes in Fig. 2.12 (A), when compressed to 0.8 GPa, a new mode (labeled as v_{7A}) appeared on the shoulder of the N-H off-plane stretching mode v_7. Then at 3.9 GPa, v_{7A} split into a doublet (labeled as v_{7B} and v_{7C}), followed by the splitting of v_7 (labeled as v_{7D} and v_{7E}) at 5.8 GPa. The similar splitting also occurred to N=N stretching mode v_3 and C-H stretching mode v_1. The N=N stretching mode v_3 first split into a doublet (labeled as v_{3A} and v_{3B}) at 2.6 GPa, among which v_{3A} disappeared upon further compression to 5.8 GPa, accompanied by the splitting of v_{3B} into a doublet (labeled as v_{3C} and v_{3D}) at the same time. Then both the doulet v_{3C} and v_{3D} gained intensity and persisted to the highest pressure 57.9 GPa. For the C-H stretching mode v_1, a broad peak labeled as v_{1A} evolved on its shoulder at 2.6 GPa and then split into a doublet (labeled as v_{1B} and v_{1C}) at 3.9 GPa. At the highest pressure 57.9 GPa, all the internal modes were significantly weakened and with broadened profiles.

2.3.2.3 Pressure dependence of lattice modes

The observed evolutions of the Raman profile in both the lattice and internal mode regions indicate pressure-induced phase transitions. By plotting the pressure dependence (dv/dP) of the lattice mode, the transition boundaries as well as the transition mechanism may be better understood. The pressure dependence of the Raman shifts of the lattice modes of 5-MTZ is presented in Fig. 2.13 and Table 2.3. The slopes of Raman shifts were determined by linear regressions. In different regions, the lattice mode blueshifted with different slopes with

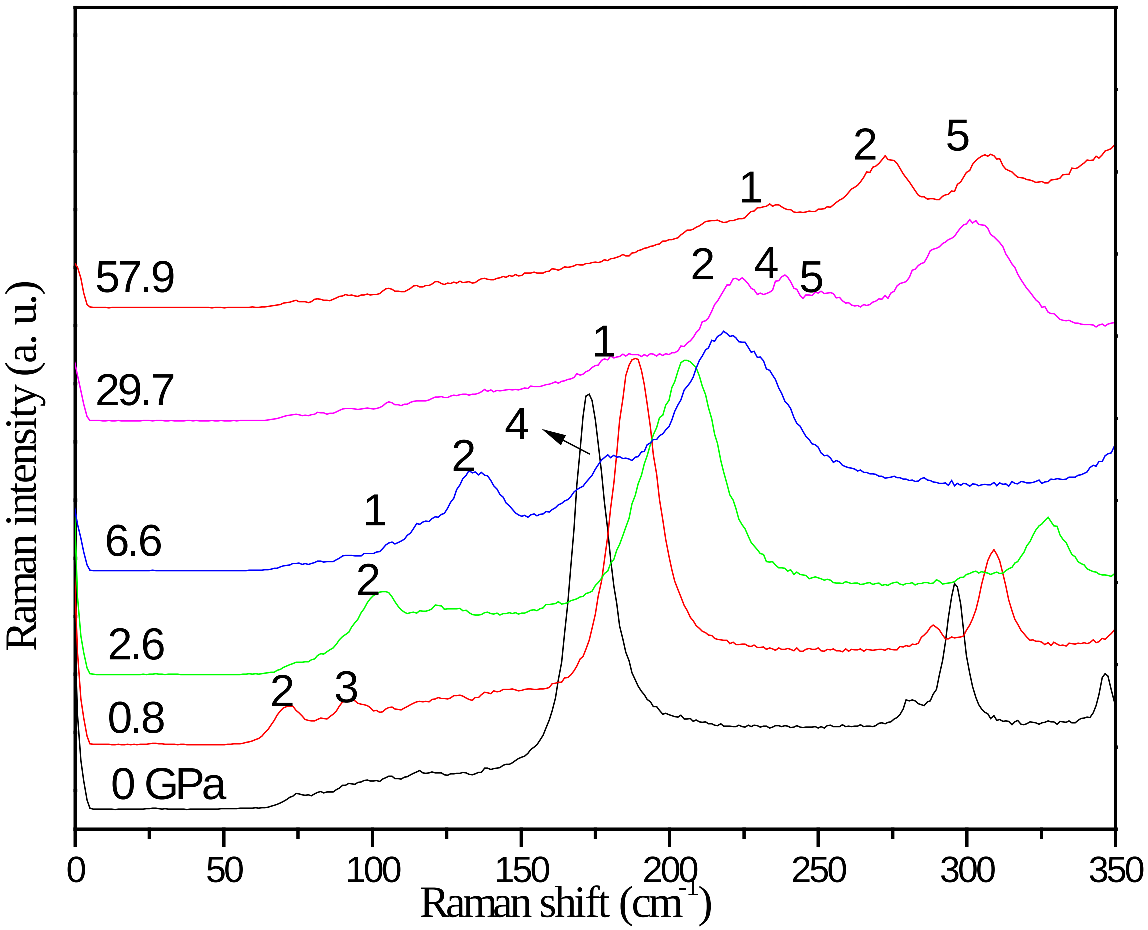

Fig. 2.11 Selected Raman spectra of 5-MTZ collected at room temperature upon compression in the lattice region of 0-350 cm^{-1}. The pressures in GPa are labeled for each spectrum. The assignments are labeled for Raman lattice modes (see text).

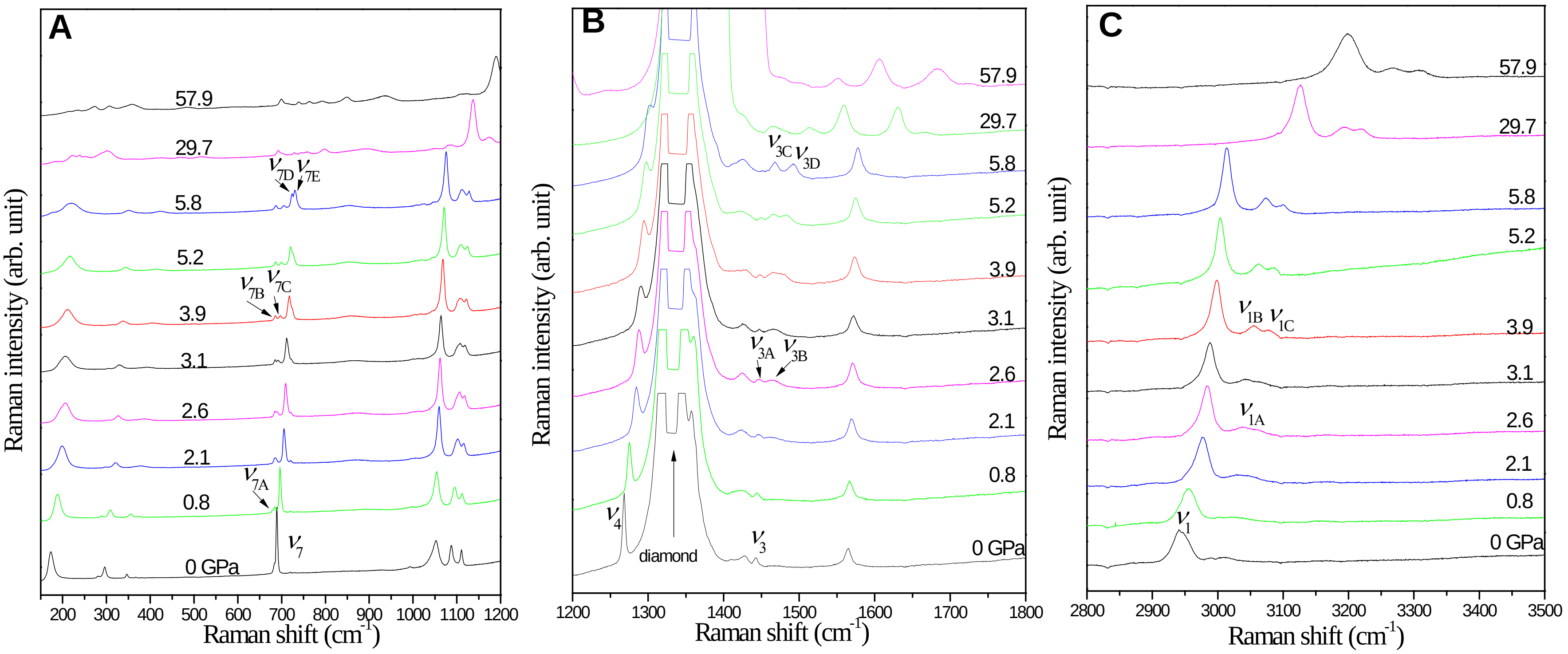

Fig. 2.12 Selected Raman spectra of 5-MTZ collected at room temperature on compression in the spectral region of 150-1200 cm^{-1} (A), 1200-1800 cm^{-1} (B), 2800-3500 cm^{-1} (C) in the pressure region of 0-57.9 GPa. The spectra ranging from 1800-2600 cm^{-1} were omitted because of the weak intensity. The pressures in GPa are labeled for each spectrum. The assignments are labeled for Raman modes (see text).

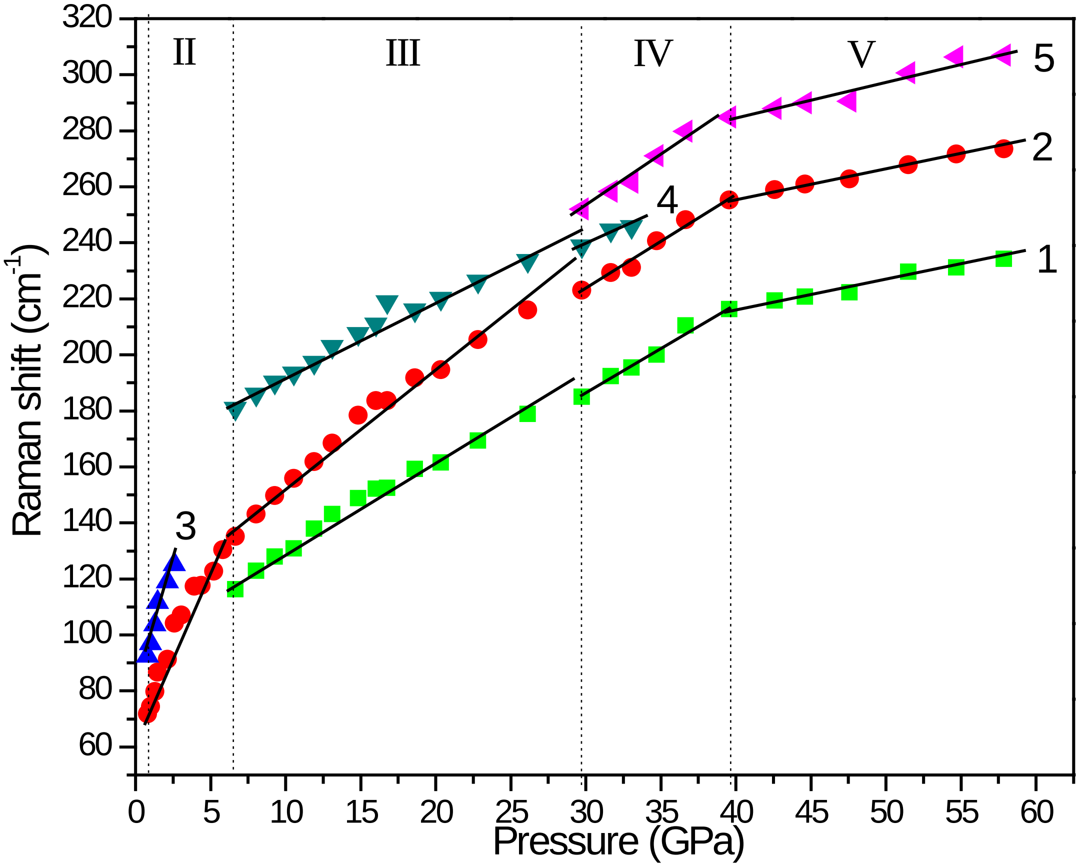

Fig. 2.13 (Color online) Raman shift of 5-MTZ as a function of pressure on compression in the lattice mode region. Solid straight lines are linear fits to the data. Vertical dashed lines marked the suggested phase transition boundaries. Different symbols denote lattice modes with different origins with numbers labeled from low to high frequencies. See text and Fig. 2.11.

Table 2.3 Pressure dependence (*dv*/*dP*) of the Raman lattice modes for different phases.

Lattice mode	Raman shift (cm^{-1})	Pressure (GPa) [a]	*dv*/*dP* (cm^{-1}/GPa)			
			Phase II (0.8-7 GPa)	Phase III (7-30 GPa)	Phase IV (30-40 GPa)	Phase V (40-58 GPa)
1	116	6.7		4.0	3.5	1.1
2	72	0.8	11.8	4.4	3.4	1.1
3	92	0.8	22.4			
4	181	6.7		3.5	3.0	
5	252	29.7			3.9	1.4

[a] The pressure at which the lattice mode was initially observed.

increasing pressure, which clearly outlined the phase boundaries (labeled as I, II, III, IV and V).

2.3.2.4 IR spectra on compression

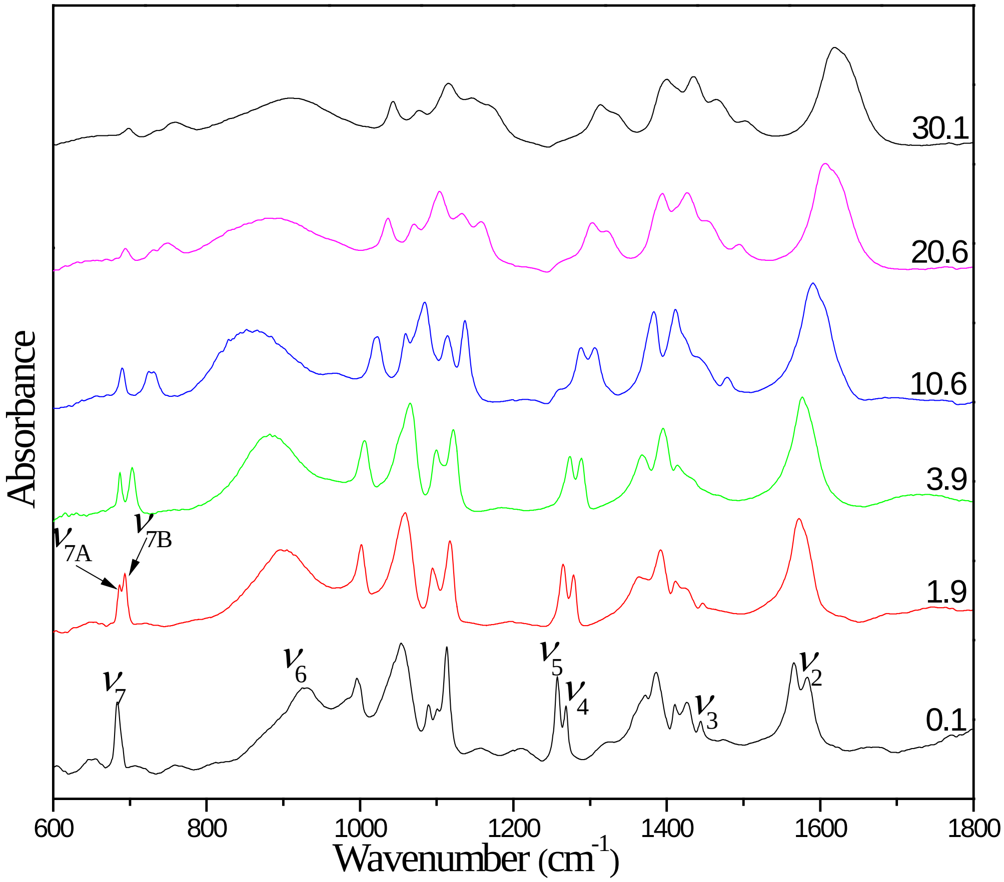

Fig. 2.14 Selected IR spectra of 5-MTZ collected at room temperature on compression in the spectral region of 600-1800 cm^{-1} in the pressure region of 0.1-30.1 GPa. The pressures in GPa are labeled for each spectrum. The assignments are labeled for IR modes (see text).

Mid-IR spectra of 5-MTZ were collected on compression to 30.1 GPa. Selected absorption spectra as a function of pressure in the spectral region of 600-1800 cm^{-1} are depicted in Fig. 2.14. Similar to the Raman measurements, the ν_7 mode began to split into a doublet labeled as ν_{7A} and ν_{7B} at 1.9 GPa. The discrepancy of the splitting pressure in Raman and IR measurements was likely due to the different origin of the doublets. Then with increasing pressure, all the modes became broadened and were weakened. In addition, the ν_6 mode, corresponding to the N-H off-plane mode, behaved unusually by shifting to lower frequency first, and then shifted to higher frequency, which was likely due to the strengthening and weakening of hydrogen bonds in different respective pressure regions. At the highest pressure 30.1 GPa, the IR profile changed significantly, indicating possible transitions occurred during compression.

2.3.2.5 Pressure effects on IR N-H off-plane mode

Since hydrogen bonds play an important role in altering the compressibility, stability as well as the reactiveness of energetic materials under high pressure,[31-33] tracing the changes of hydrogen bonds in 5-MTZ may help explain the high-pressure behavior as well as the possible transition mechanism. The pressure dependence of the N-H off-plane mode v_6 of 5-MTZ were examined by plotting wavenumbers as a function of pressure as shown in Fig. 2.15. As can be seen, the change of mode v_6 could be divided into two stages. First it redshifted with increasing pressure until 12.5 GPa, which could be interpreted as the strengthening of the hydrogen bond. Then followed by the blueshift to 30.1 GPa, suggesting the hydrogen bond was weakened.

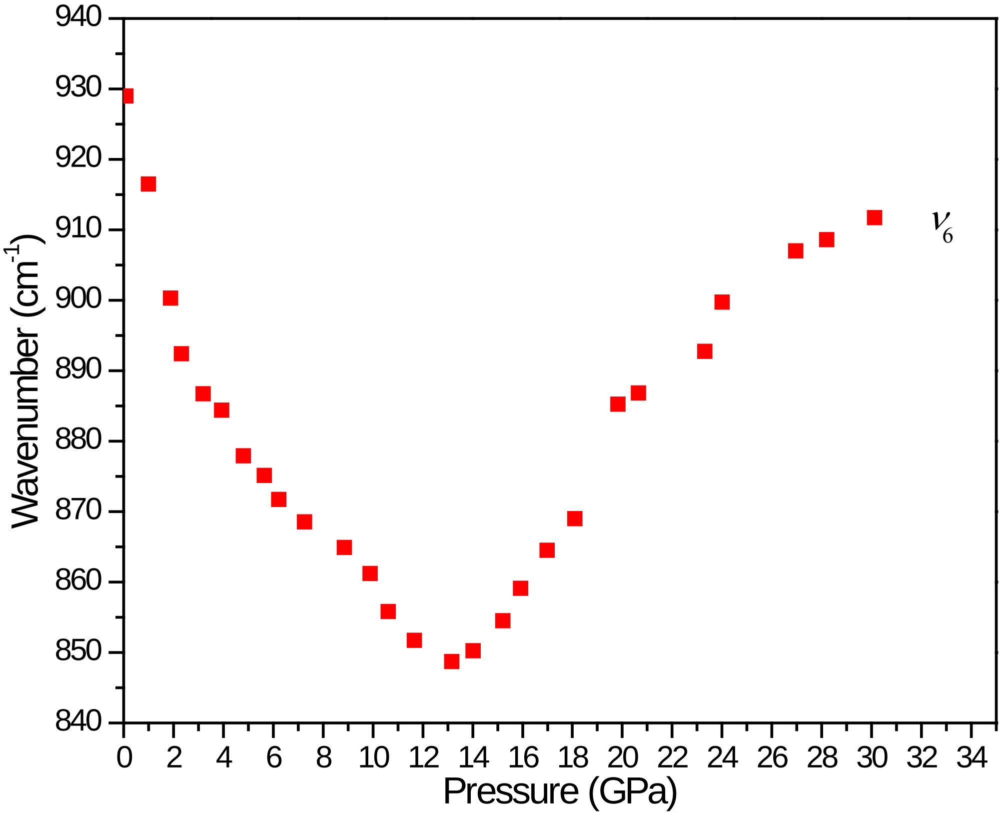

Fig. 2.15 Pressure dependence of the N-H off-plane mode v_6.

2.3.2.6 Raman and IR spectra on decompression

Raman and IR spectra were also collected on decompression all the way down to near-ambient pressure, shown in Fig. 2.16, in order to better understand the pressure-induced structural evolutions and the high-pressure stability of 5-MTZ. During decompression, similar back transformations in both Raman and IR spectra were observed, indicating very minor hysteresis. More importantly, as can been seen in Fig. 2.16, all modes observed before compression at ambient pressure were completely recovered upon decompression to near-ambient pressure, meaning that the tetrazole ring was stable even at 58 GPa. The difference in Raman shift before and after compression could be due to the different pressures under which the spectra were collected whereas the different IR band shape and band intensity could be associated with the modification of the sample thickness in the compression/decompression cycle. All these observations suggest that the pressure-induced structural transformations of 5-MTZ are reversible, and 5-MTZ is chemically stable in the entire pressure region in this study.

2.4 Discussion

Our Raman and IR measurements collectively indicated that for 5-ATZ there were no phase transitions in the pressure range of 0-57 GPa and 0-38 GPa, respectively. In strong contrast, several distinct phases with boundaries at around 0.8, 7, 30 and 40 GPa were observed for 5-MTZ during compression. While the transition at 0.8 GPa can be characterized as the removal of the orientational disorder for no lattice modes existed at ambient conditions, the subsequent transitions are associated with changes in crystal lattices or molecular structures. The difference of the phase transitions between 5-ATZ and 5-MTZ could possibly due to the number and strength of the hydrogen bonds existing in those materials. For 5-ATZ, the two N-H in the amino group and the N-H within the tetrazole ring could form three different hydrogen bonds, whereas in 5-MTZ only the N-H within the tetrazole ring could form a hydrogen bond with adjacent molecules. Moreover, as can be seen from Fig. 2.7, the ring N-H distance displayed the highest decreasing rate and this trend did not stop even at around 38 GPa, whereas the amino N-H distance increased until 11.6 GPa and then followed by the slight decrease of the distance, which made the ring N-H···N the dominant hydrogen bonds in 5-ATZ. However, in 5-MTZ, the ring N-H···N was strengthened and then was weakened

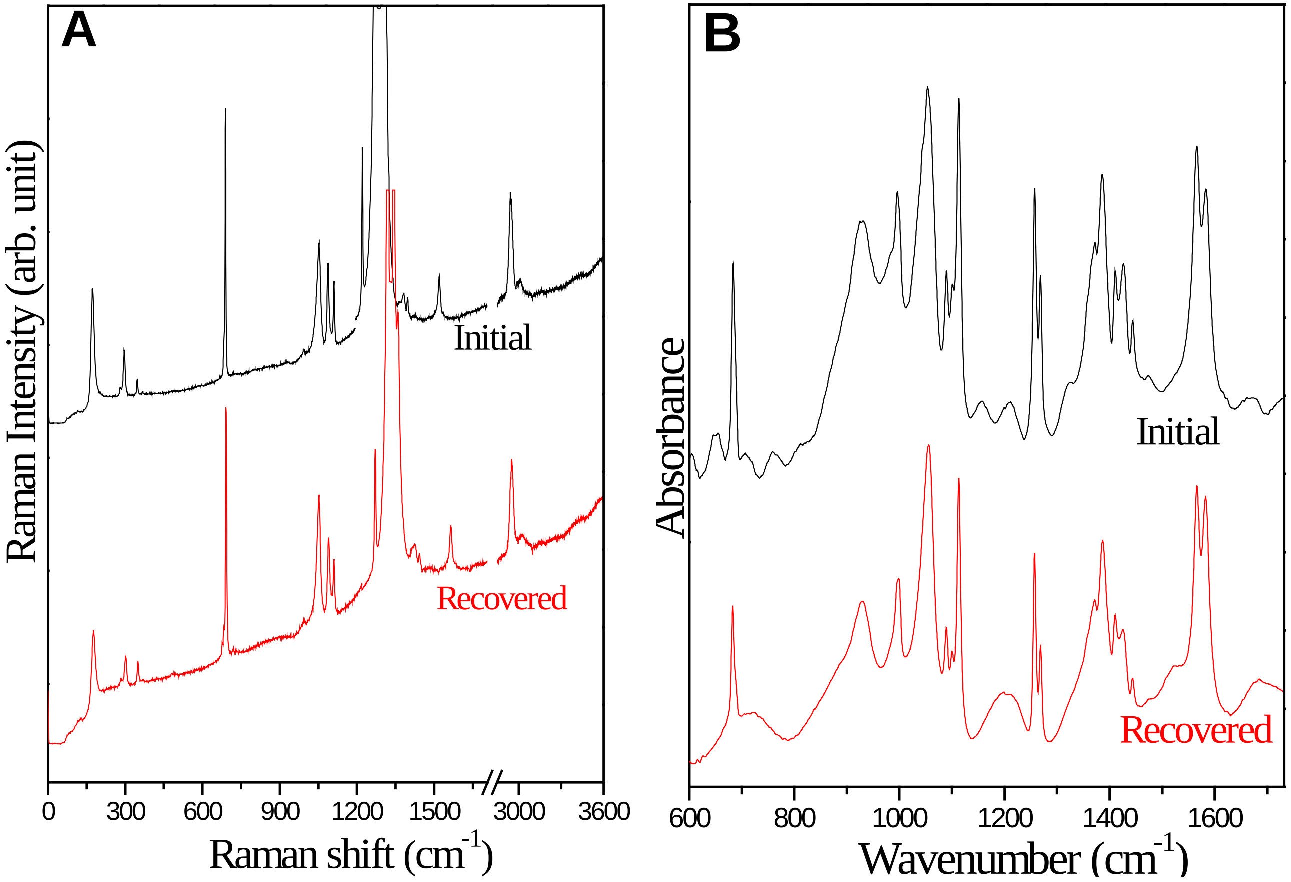

Fig. 2.16 Raman (A) and IR (B) spectra of recovered 5-MTZ upon decompression in comparison with those respective near ambient-pressure spectra before compression.

when compressed to 12.5 GPa, from which we could know the compressibility of the hydrogen bond in 5-MTZ is much weaker than that in 5-ATZ. Due to the fact that the hydrogen bonds played as the role of buffer to reduce the intermolecular interactions and thus the occurrence of new lattice modes and splitting of internal modes caused by the pressure-enhanced intermolecular interactions could happen more likely in 5-MTZ. Moreover, since the hydrogens in the amino group are hydrogen bonded to adjacent molecules, the conformational change caused by the functional group rotation is restricted. However, the methyl group in 5-MTZ could freely rotate at low pressures, which might be another reason of causing the multiple phase transitions and the peak splitting.

Since the internal strain of the five-membered aromatic rings that makes the molecules less stable than six-membered counterparts, usually the transition is expected to occur at lower pressures.[41] For example, furan had two phases in the 1.2–12 GPa pressure range and started to have ring-opening reaction above 12 GPa.[41] Similarly, thiophene underwent a solid-to-solid phase transformation at 6 GPa and then an irreversible reaction at 16 GPa.[42] However, when decompressed to ambient pressure, all the tetrazole ring vibration modes in both 5-ATZ and 5-MTZ were recovered from around 57 GPa, which was unusual for five-member aromatic ring at such high pressures without chemical reactions taking place. Apart from the influence of hydrogen bonds, other reason might lead to the extraordinary stability of the tetrazole ring. According to West[43], polymerization reaction is favored if multiple bonds are parallel and no further than 4 Å apart. For example, when compressed to 16 GPa, C=C bonds in adjacent thiophene molecules are parallel and the shortest C···C distances between adjacent molecules is 3.16 Å[42], making the formation of a chain polymer possible. Therefore, we could infer that the packing of tetrazole ring in both 5-ATZ and 5-MTZ under high pressure is inefficient, mainly due to the orientation of the ring. Another possible reason is that the steric hindrance of the functional group, which may weaken the intermolecular interactions of the unsaturated bonds and thus impede the polymerization. Although the tetrazole rings in both compounds were not destroyed under high pressure, electronics within the ring may be redistributed, evidenced by the splitting and intensity change of N=N stretching mode of both compounds during compression. So we could speculate that tautomerism, shown in Figs. 2.2 and 2.17, might occur in both 5-ATZ[27,28] and 5-MTZ[44] during compression, although the possible mechanisms are still unknown.

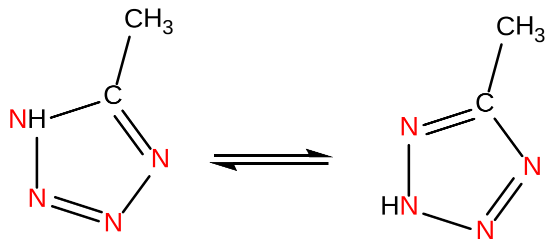

Fig. 2.17 1H-form and 2H-form of 5-MTZ

Based on former high-pressure studies on several tetrazole-containing derivatives[45-49], our results are in close agreement with theirs on the stability of the tetrazole ring. Therefore, we can draw the conclusion that 5-ATZ and 5-MTZ are not suitable precursors for the high-pressure synthesis of polymeric nitrogens.

2.5 Conclusion

Using *in situ* Raman and FTIR spectroscopy, we investigated high-pressure properties of 5-ATZ and 5-MTZ up to around 57 GPa. No phase transitions were found for 5-ATZ in the entire pressure range. After decompression, the lattice modes were not recovered but the internal modes were fully recovered. For 5-MTZ, four phase transitions were observed at around 0.8, 7, 30 and 40 GPa, evidenced by the appearance of new lattice modes, the change in peak profiles as well as the pressure dependence of Raman lattice modes over different pressure ranges. In addition, the transition was identified reversible for all the modes were recovered. The unusual high stability of the tetrazole ring in both 5-ATZ and 5-MTZ could possibly due to the hydrogen bonds on the one hand, which played as the stabilizer to reduce the intermolecular interactions. On the other hand, the packing of the tetrazole ring under high pressure may be unfavorable for polymerization, thus lead to the extraordinary high stability of the ring. Besides, tautomerism may also occur during compression, which may contribute to the high-pressre stability of the ring. Combined with the previous investigation on tetrazole or tetrazole-containing derivatives, changing the pressure only cannot trigger the polymerization of 5-ATZ and 5-MTZ easily. Other techniques, such as high-temperature, should be combined with high-pressure technique in order to make the polymerization occur at mild conditions.

2.6 Acknowledgements

The authors acknowledge funding support from a Research Tools and Instruments Grant from the National Science and Engineering Research Council of Canada, a Leaders Opportunity Fund from the Canadian Foundation for Innovation, an Early Researcher Award from the Ontario Ministry of Research and Innovation and a Petro-Canada Young Innovator Award from the University of Western Ontario.

2.7 References

(1) Eremets, M. I.; Gavriliuk, A. G.; Trojan, I. A.; Dzivenko, D. A.; Boehler, R. *Nat. Mater.* **2004**, *3*, 558.

(2) Eremets, M. I.; Popov, M. Y.; Trojan, I. A.; Denisov, V. N.; Boehler, R.; Hemley, R. J. *J. Chem. Phys.* **2004**, *120*, 10618.

(3) Klapötke, T. M. *Struct. Bond.* **2007**, *125*, 85.

(4) Medvedev, S. A.; Trojan, I. A.; Eremets, M. I.; Palasyuk, T.; Klapötke, T. M.; Evers, J. *J. Phys. : Condens. Matter* **2009**, *21*, 195404.

(5) Nguyen, M. T. *Coordin. Chem. Rev.* **2003**, *244*, 93.

(6) Wilson, W. W.; Vij, A.; Vij, V.; Bernhardt, E.; Christe, K. O. *Chem. Eur. J.* **2003**, *9*, 2840.

(7) Klapötke, T. M.; Sabaté, C. M. *Chem. Mater.* **2008**, *20*, 3629.

(8) Li, Y.-C.; Qi, C.; Li, S.-H.; Zhang, H.-J.; Sun, C.-H.; Yu, Y.-Z.; Pang, S.-P. *J. Am. Chem. Soc.* **2010**, *132*, 12172.

(9) Klapötke, T. M.; Piercey, D. G. *Inorg. Chem.* **2011**, *50*, 2732.

(10) Sivabalan, R.; Anniyappan, M.; Pawar, S. J.; Talawar, M. B.; Gore, G. M.; Venugopalan, S.; Gandhe, B. R. *J. Hazard. Mater.* **2006**, *137*, 672.

(11) Karaghiosoff, K.; Klapotke, T. M.; Mayer, P.; Sabate, C. M.; Penger, A.; Welch, J. M. *Inorg. Chem.* **2007**, *47*, 1007.

(12) Fendt, T.; Fischer, N.; Klapötke, T. M.; Stierstorfer, J. R. *Inorg. Chem.* **2011**, *50*, 1447.

(13) Klapötke, T. M.; Stierstorfer, J. *Helv. Chim. Acta* **2007**, *90*, 2132.

(14) Fischer, N.; Klapötke, T. M.; Stierstorfer, J.; Wiedemann, C. *Polyhedron* **2011**, *30*, 2374.

(15) Huynh, M. H. V.; Coburn, M. D.; Meyer, T. J.; Wetzler, M. *Proc. Natl. Acad. Sci.* **2006**, *103*, 10322.

(16) Delalu, H.; Karaghiosoff, K.; Klapotke, T. M.; Sabate, C. M. *Cent. Eur. J. Energ. Mater.* **2010**, *7*, 197.

(17) Sivabalan, R.; Talawar, M.; Senthilkumar, N.; Kavitha, B.; Asthana, S. *J. Therm. Anal. Calorim* **2004**, *78*, 781.

(18) Ramaswamy, C. P. *US Pat.* 5661261, 1997.

(19) Lund, G. K.; Blau, R. J. *US Pat.* 5500059, 1995.

(20) Fallis, S.; Reed, R. In *Proceedings of Halon Options Technical Working Conference* **2000**, 361.

(21) Gao, A.; Oyumi, Y.; Brill, T. B. *Combust. Flame.* **1991**, *83*, 345.

(22) Lesnikovich, A. I.; Ivashkevich, O. A.; Levchik, S. V.; Balabanovich, A. I.; Gaponik, P. N.; Kulak, A. A. *Thermochim. Acta* **2002**, *388*, 233.

(23) Brill, T. B.; Ramanathan, H. *Combust. Flame.* **2000**, *122*, 165.

(24) Paletsky, A. A.; Budachev, N. V.; Korobeinichev, O. P. *Kinet. Catal.* **2009**, *50*, 627.

(25) Kiselev, V. G.; Gritsan, N. P. *J. Phys. Chem. A* **2009**, *113*, 3677.

(26) Fujihisa, H.; Honda, K.; Obata, S.; Yamawaki, H.; Takeya, S.; Gotoh, Y.; Matsunaga, T. *Cryst. Eng. Comm.* **2011**, *13*, 99.

(27) Pinto, R. M.; Dias, A. A.; Coreno, M.; de Simone, M.; Giuliano, B. M.; Santos, J. P.; Costa, M. L. *J. Electron. Spectrosc. Relat. Phenom.* **2012**, *185*, 13.

(28) Pinto, R. M.; Dias, A. A.; Costa, M. L. *Chem. Phys.* **2011**, *381*, 49.

(29) Murphy, D. B.; Picard, J. P. *J. Org. Chem.* **1954**, *19*, 1807.

(30) Obata, S.; Takeya, S.; Fujihisa, H.; Honda, K.; Gotoh, Y. *J. Phys. Chem. B* **2010**, *114*, 12572.

(31) Boldyreva, E. V. *J. Mol. Struct.* **2004**, *700*, 151.

(32) Mushayakarara, E. C.; Wong, P. T. T.; Mantsch, H. H. *Biochem. Bioph. Res. Co.* **1986**, *134*, 140.

(33) Aoki, K.; Kakudate, Y.; Yoshida, M.; Usuba, S.; Fujiwara, S. *J. Chem. Phys.* **1989**, *91*, 2814.

(34) Ohno, Y.; Akutsu, Y.; Arai, M.; Tamura, M.; Matsunaga, T. *Acta Crystallogr., Sect. C* **1999**, *55*, 1014.

(35) Schettino, V.; Bini, R. *Phys. Chem. Chem. Phys.* **2003**, *5*, 1951.

(36) Jayaraman, A. *Rev. Sci. Instrum.* **1986**, *57*, 1013.

(37) Jonassen, H. B.; Paukert, T.; Henry, R. A. *Appl. Spectrosc.* **1967**, *21*, 89.

(38) Levchik, S. V.; Ivashkevich, O. A.; Balabanovich, A. I.; Lesnikovich, A. I.; Gaponik, P. N.; Costa, L. *Thermochim. Acta* **1992**, *207*, 115.

(39) Masahiro Murotani, T.; Hajime Mura, U.; Makoto Takeda, T.; Hiroshi Shibafuchi, U. *US Pat.* 5594146, 1997.

(40) Matveeva, N.; Suschko, N.; Makarevich, N.; Gaponik, P.; Ivashkevich, O.; Koren, A. *J. Appl. Spectrosc.* **1992**, *57*, 845.

(41) Ceppatelli, M.; Santoro, M.; Bini, R.; Schettino, V. *J. Chem. Phys.* **2003**, *118*, 1499.

(42) Pruzan, P.; Chervin, J. C.; Forgerit, J. P. *J. Chem. Phys.* **1992**, *96*, 761.

(43) West, A. R.. Solid State Chemistry and Its Applications, Wiley, New York, 1984.

(44) Pinto, R. M.; Dias, A. A.; Coreno, M.; Simone, M. d.; Giuliano, B. M.; Santos, J. P.; Costa, M. L. *Chem. Phys. Lett.* **2011**, *516*, 149.

(45) Ciezak, J. A. *Propellants Explos. Pyrotech.* **2010**, *35*, 550.

(46) Ciezak, J. A. *Propellants Explos. Pyrotech.* **2010**, *35*, 373.

(47) Ciezak, J. A. *Propellants Explos. Pyrotech.* **2010**, *35*, 24.

(48) Ciezak, J. A. *Propellants Explos. Pyrotech.* **2011**, *36*, 446.

(49) Ciezak, J. A. *AIP Conf. Proc.* **2012**, *1426*, 1424.

Chapter 3 *In situ* high-pressure study of 5, 5´-bis(2-methyltetrazolyl)amine monohydrate by vibrational spectroscopy and X-ray diffraction

3.1 Introduction

Recent years, compounds containing the backbone of directly linked nitrogen atoms are of great interests because they could generate molecular nitrogen as the final product, during which a large amount of energy will be released due to the energy difference between the N-N or N=N and N≡N bonds. Besides, the end-product nitrogen is also highly desired in terms of avoiding environmental pollutions and health risks.[1-4] In 2004, Eremets *et al.*[5] synthesized the diamond-like polymeric nitrogen, which was considered a novel energetic material, directly from molecular nitrogen at pressures above 110 GPa and temperatures above 2,000 K. However, the problem is that the pressure and temperature of synthesizing this material is too extreme and it could not be recovered at ambient conditions. Therefore, searching for proper precursors to synthesize the polymeric nitrogens at lower pressures and temperatures is of great interest.[6-8]

In the past few years, great efforts have been directed towards the synthesis of nitrogen-rich or polynitrogen compounds,[9-13] among which tetrazole-containing compounds and tetrazole salts are of great interest because of their high nitrogen contents, heat of formation as well as good thermal stabilities.[14] 5, 5´-bis(1H-tetrazolyl)amine (BTA) is such a compound composed of two tetrazole rings linked by one nitrogen atom and containing 82.5% nitrogen by weight. However, according to the UN Recommendations for the "Transport of Dangerous Goods", BTA is classified as sensitive due to its impact (30J) and friction sensitivity (300N),[11] which makes it less interested for industrial applications and researches. As its monohydrated form, $BTA\cdot H_2O$ is sensitive towards neither impact (<100 J) nor friction (<360 N),[11] which makes it an ideal replacement to study the properties of BTA, although the nitrogen content is a little bit lower (73.7%). Under ambient conditions it crystallizes into a monoclinic cell with space group $P2_1/C$ and cell parameters a = 9.367 Å, b = 10.531 Å, c = 6.808 Å, and V = 671.6 Å^3.[15] Its molecular structure is shown in Fig. 3.1, among which the oxygen atom in the water is attached to the N2 within the tetrazole ring.

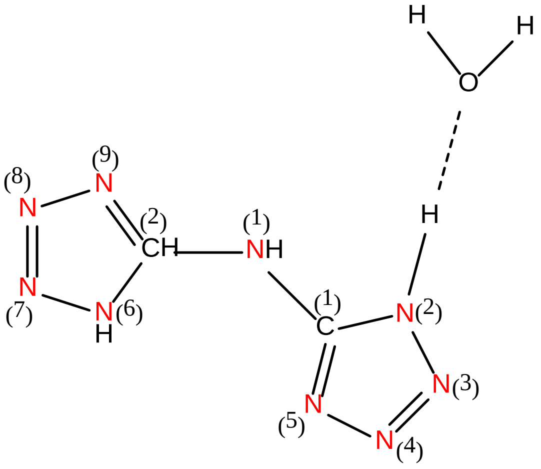

Fig. 3.1 Molecular structure of BTA·H_2O

Since high-pressure technique is a useful tool in terms of reducing the available volume and increasing the electronic density, therefore, it could be used as a driving force to trigger chemical reactions, especially when unsaturated chemical bonds are present.[16] Therefore, we could use high-pressure to break the N=N bond and form N-N bonds between adjacent molecules in order to synthesize polymeric nitrogens. In this study, we report the first *in situ* high-pressure Raman and IR measurements on BTA·H_2O, which were compressed up to about 25 GPa in diamond anvil cells.

3.2 Experimental Section

3.2.1 Sample preparation

BTA·H_2O was synthesized[15] at University of Ottawa and the purity was checked before experiments. A symmetrical DAC with two type-I diamonds with 250 μm culets was used for the high-pressure Raman measurements, while a pair of type-II diamonds with a culet size of 350 μm was used for the IR measurements. One ruby (Cr^{3+} doped α-Al_2O_3) chip as the pressure calibrant was carefully placed inside the sample chamber before the sample was loaded. The pressure was determined by using the R_1 ruby fluorescence line shift with an accuracy of ± 0.05 GPa under quasi-hydrostatic conditions[17]. For IR measurements, spectral quality KBr powders were also loaded into the DAC used both as pressure transmitting medium and to dilute the sample.

3.2.2 High-pressure Raman and IR measurements

The apparatuses used for Raman and IR measurements are the same with chapter 2. For each Raman spectrum of BTA·H_2O, a collection time of 15 s was employed, and the average laser power on the sample was maintained at ~ 20 mW.

3.2.3 High-pressure XRD measurements

In situ angle-dispersive X-ray diffraction measurements were carried out at room temperature using the 16-BM-D beamline of the HPCAT at the Advanced Photon Source. The incident wavelength of the monochromatic beam was 0.424603 Å with a beam size of 5 × 12 μm^2 focused at the sample. The diffraction data were recorded on a MAR345 imaging plate with an exposure time of 240 s. Then, the 2D Debye-Scherrer diffraction patterns were integrated by using the Fit2D program.

3.3 Results

3.3.1 Raman and IR spectra of BTA·H_2O at ambient-pressure

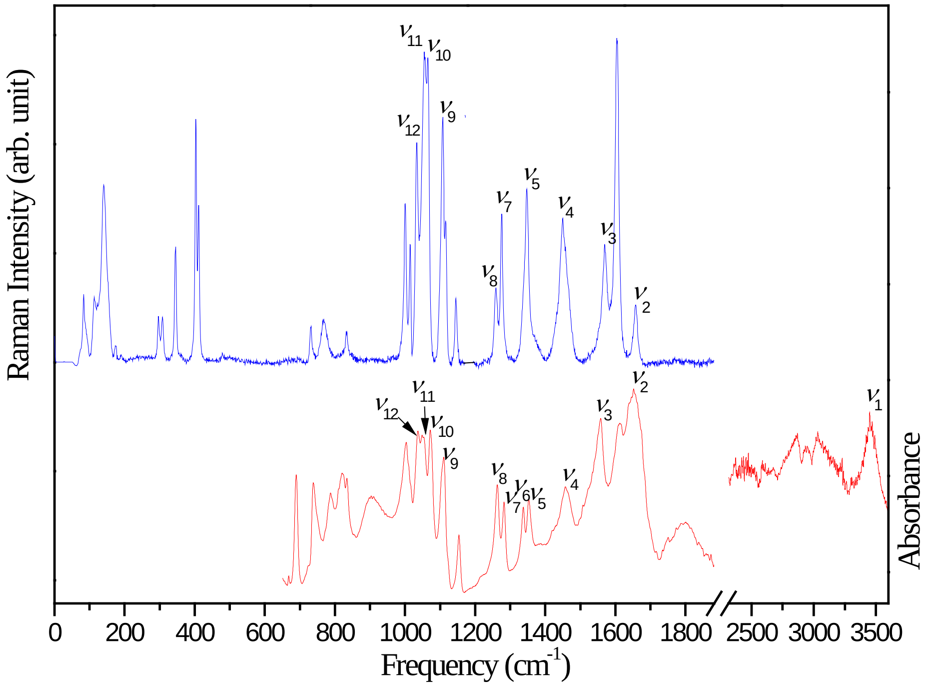

Fig. 3.2 Raman spectrum of BTA·H_2O (top) in comparison with IR spectrum (bottom) in the spectral region 0-3600 cm^{-1} both collected at near ambient pressure and room temperature. The omitted spectral regions are due to the lack of spectroscopic features. The assignment of the vibrational modes is labeled above each.

Raman and IR spectra were collected at ambient conditions as the starting point and are shown in Fig. 3.2. Compared to the Raman and IR study by Thomas *et al*.[15] on condensed phase of BTA·H_2O, our measurements are in close agreement with theirs. We followed the assignment proposed by Thomas[15] and labeled only some tetrazole ring vibration modes in Table 3.1 due to the complexity of the assignment.

Table 3.1 Assignment and frequencies (cm^{-1}) of observed Raman and IR internal modes of BTA·H_2O in comparison with reference values.

Mode	Description	This work		References	
		Raman	IR	Raman[15]	IR[15]
v_1	N_{tet}-H stretch		3459		3456
v_2	C_{tet}-N-C_{tet} asym	1658	1655	1649	1656
v_3	C_{tet}-N-C_{tet} sym	1570	1560	1552	1556
v_4	N=N stretch	1451	1456	1455	1454
v_5	C=N stretch	1347	1352	1346	1352
v_6	C=N stretch		1338		1337
v_7	N-N stretch	1276	1282		1282
v_8	N-N stretch	1259	1263	1267	1263
$^*v_9$	Ring vibration	1108	1108		
$^*v_{10}$	Ring vibration	1065	1072		
$^*v_{11}$	Ring vibration	1055	1053		
$^*v_{12}$	Ring vibration	1033	1036		

*The assignments of those modes were based on the vibrational study on 5-aminotetrazole.[26]

3.3.2 Raman spectra on compression

Starting from ambient pressure, Raman spectra of BTA·H_2O were collected upon compression to 25.4 GPa with selected spectra depicted in Fig. 3.3. Upon compression, all the peaks became broadened and were weakened, especially for the ring vibration modes in the range of 1000-1150 cm^{-1}. Then with increasing pressure, the profile of ring vibration modes changed, accompanied by the strengthening of the C_{tet}-N-C_{tet} symmetric stretching mode v_3 and the weakening of the N=N stretching mode v_5. Moreover, the N-N stretching modes v_8 nd v_9 began to merge into a broadened singlet at 4.6 GPa. Upon subsequent

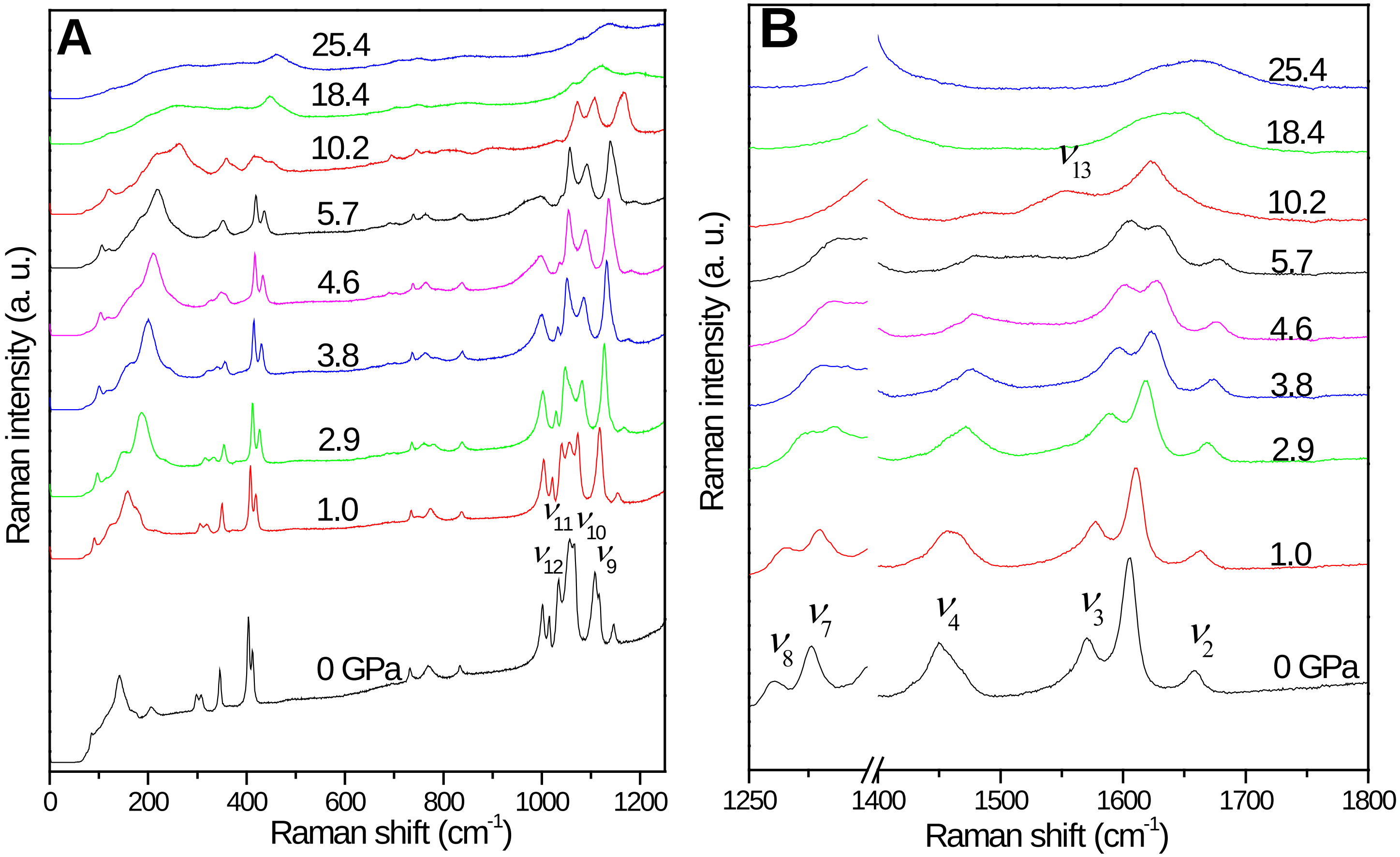

Fig. 3.3 Selected Raman spectra of BTA·H_2O collected at room temperature on compression in the spectral region of 0-1250 cm^{-1} (A), 1250-1800 cm^{-1} (B) in the pressure region of 0-25.4 GPa. The pressures in GPa are labeled for each spectrum. The assignments are labeled for Raman modes (see text).

compression to 10.2 GPa, all the modes were significantly weakened, together with the disappearance of N=N stretching mode ν_5 and N-N stretching mode ν_8 and ν_9, and the appearance of a new peak located at 1553 cm^{-1} (labeled as ν_{13}). At the same time, the C_{tet}-N-C_{tet} symmetric stretching mode ν_3 merged with its adjacent peak located at 1605 cm^{-1}. When compressed to 18.4 GPa, the lattice modes disappeared, indicating the structure was amorphous. In addition, nearly all the peaks disappeared except for three broad bands located at 448, 1122 and 1644 cm^{-1}, which even persisted at the highest pressure 25.4 GPa.

3.3.3 IR spectra on compression

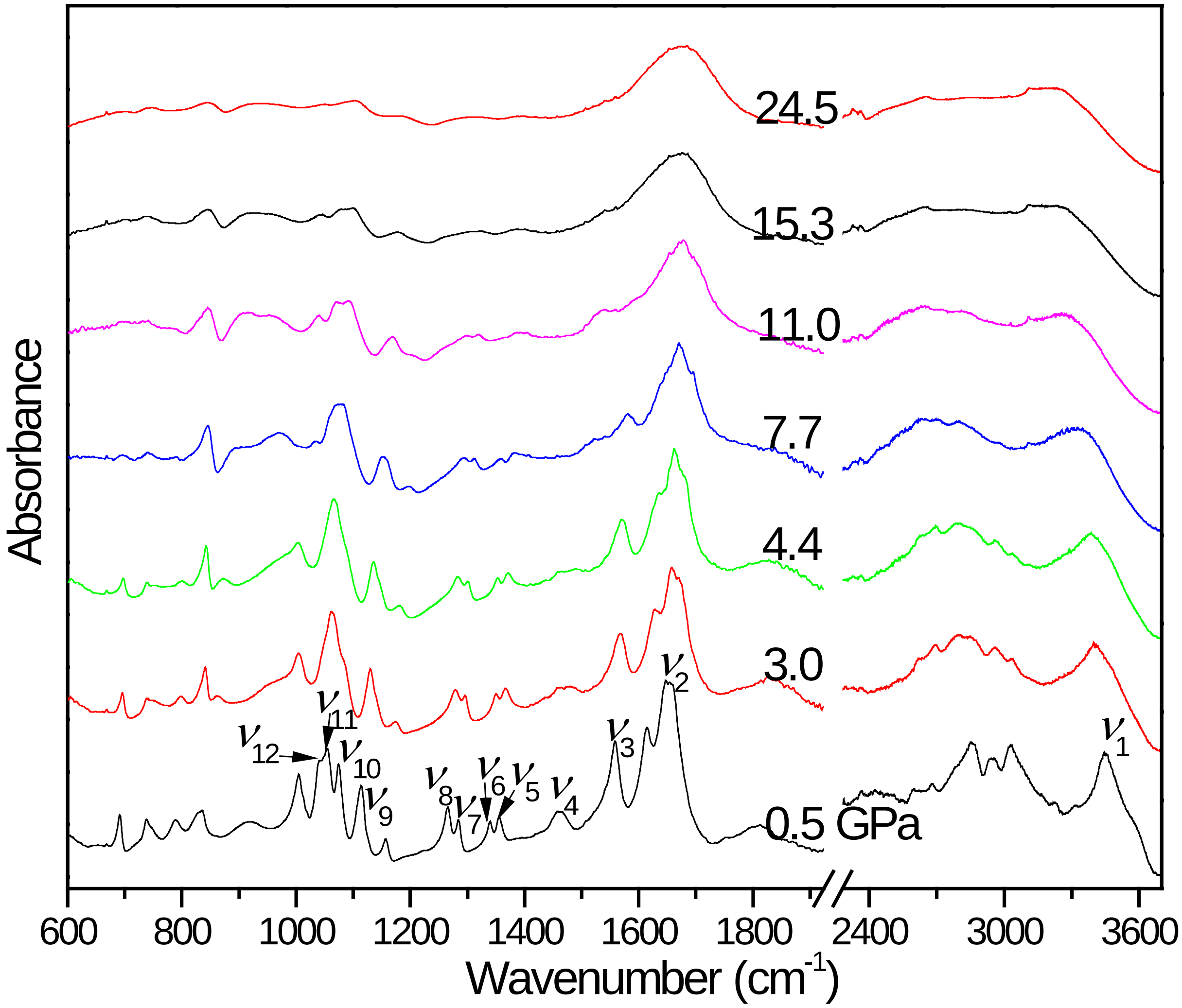

Fig. 3.4 Selected IR spectra of BTA·H_2O collected at room temperature on compression in the spectral region of 600-3700 cm^{-1} in the pressure region of 0.5-24.5 GPa. The pressures in GPa are labeled for each spectrum. The assignments are labeled for IR modes (see text).

Mid-IR spectra of BTA·H_2O were collected on compression to 24.5 GPa. Selected absorption spectra as a function of pressure in the spectral region of 600-3700 cm^{-1} are depicted in Fig. 3.4. Similar to the Raman spectra, upon compression the profile of ring vibration modes started to change, accompanied by the splitting and weakening of the N=N stretching mode v_4, which then disappeared when compressed to around 7.7 GPa. At the same time, the C=N stretching mode v_5 and v_6 as well as N-N stretching mode v_7 and v_8 began to merge and evolved to a broadened band at 11.0 GPa. Upon subsequent compression, all the internal modes were significantly broadened with weakened absorption. At the highest pressure, only the ring vibration modes, C_{tet}-N-C_{tet} stretching mode v_2 as well as few unlabeled peaks located around 800 cm^{-1} existed.

The most interesting change happened in the range of 2400-3600 cm^{-1}, where existing the N_{tet}-H stretching mode v_1 and water stretching modes. However, the water stretching modes cannot be resolved due to the low absorption and broad features. With increasing pressure, the N_{tet}-H stretching mode v_1 shifted to lower frequency, and then followed by the stabilization of the frequency. At the highest pressure 24.5 GPa, it still existed but with more broadened features and weakened absorbance.

3.3.4 Pressure effects on Raman and IR modes

The pressure dependence of the observed Raman and IR modes of BTA·H_2O were examined by plotting the vibrational frequencies as a function of pressure as shown in Fig. 3.5 (A) and 3.5 (B). In general, in the range of 0-1800 cm^{-1} all the Raman and IR modes exhibited pressure-induced blue shifts, indicating that bonds became stiffened upon compression. The linear increasing of these modes with increasing pressure suggested that no phase transitions occurred during compression. Moreover, the splitting of some internal modes was observed, which was likely caused by the pressure-enhanced intermolecular interactions or the change of ring orientation. For the N_{tet}-H stretching mode in 3200-3500 cm^{-1}, very obvious red shift could be seen upon compression. Then it ceased to shift to lower frequency at around 12 GPa and kept almost unchanged to the highest pressure, which suggested the strengthening and stabilization of intermolecular hydrogen bonds. Overall, the Raman and IR spectra indicated that no phase transitions and chemical reaction occurred during compression, though the interaction between molecules might be enhanced or the ring orientation may change.

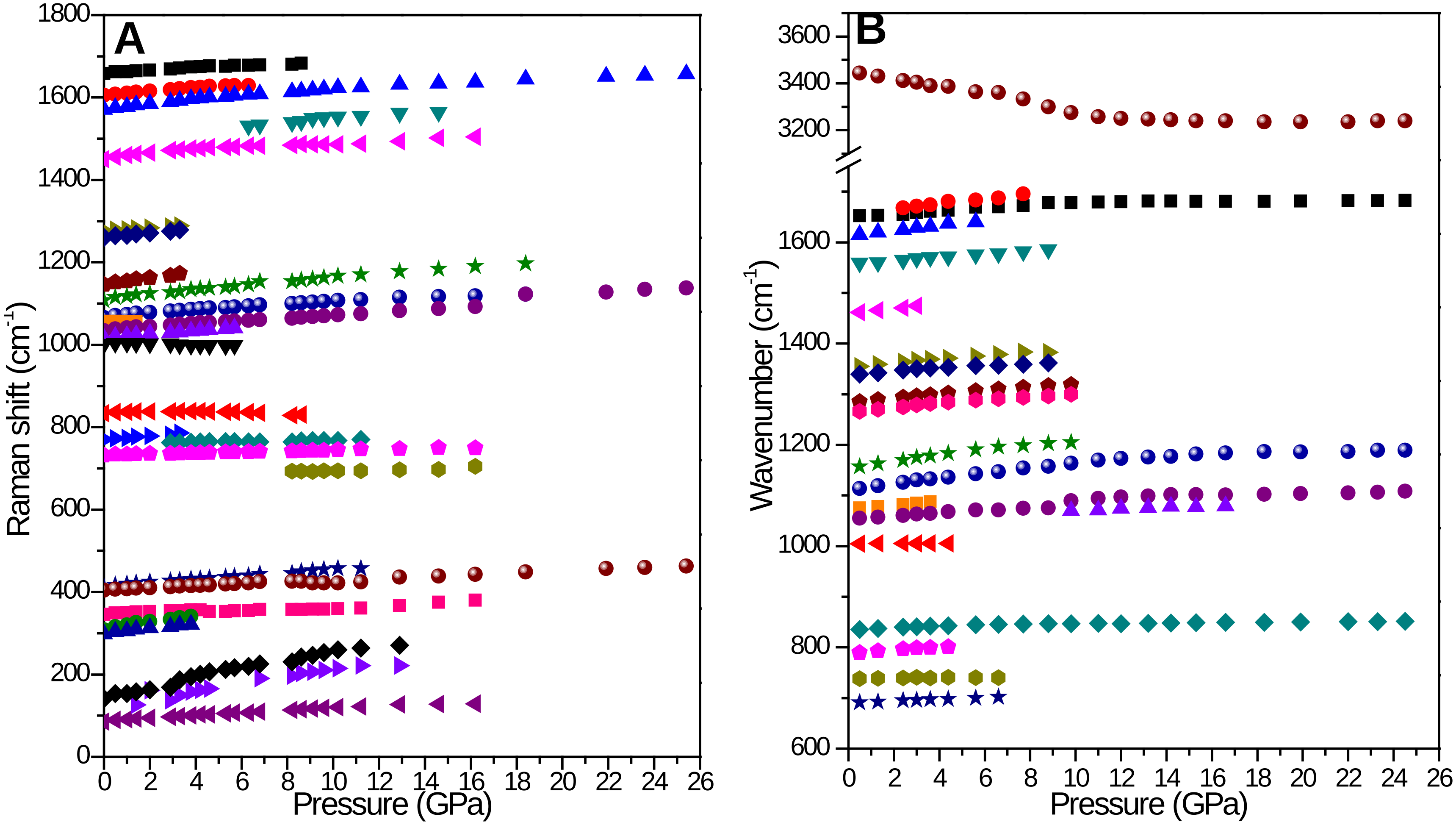

Fig. 3.5 Pressure dependence of Raman shifts (A) and IR modes (B) of BTA·H_2O on compression. Different symbols represent modes with different origins of assignments.

3.3.5 Raman and IR spectra on decompression

Raman and IR spectra were collected on decompression all the way down to near-ambient pressure in order to better understand the high-pressure stability of BTA·H_2O. Starting from 25.4 GPa, Raman spectra of BTA·H_2O were collected upon decompression to near-ambient with selected spectra depicted in Fig. 3.6. During decompression, very strong hysteresis was observed, which was likely caused by the hydrogen bonds, and all the modes were recovered upon decompression to ambient pressure, indicating that the lattice was reversible in the 0-25.4 GPa compression/decompression cycle and the tetrazole ring was stable at 25.4 GPa. In addition, the peaks were broadened and weakened, which could be due to the disordering of crystal structures during decompression.

Mid-IR spectra of BTA·H_2O were collected from 24.5 GPa to near ambient pressure. Selected absorption spectra as a function of pressure in the spectral region of 600-3700 cm^{-1} are depicted in Fig. 3.7. In agreement with the Raman spectra, during decompression very strong hysteresis could also be seen in the IR spectra. Upon decompression to ambient pressure, all the modes were recovered, with difference being that the absorbance was lower, which was likely caused by the modification of the sample thickness in the compression/decompression cycle.

3.3.6 XRD patterns on compression and decompression

Supplementary to the Raman and IR results, XRD pattern of BTA·H_2O upon compression and decompression were collected with selected XRD pattern shown in Fig. 3.8. The diffraction pattern at near ambient pressure can be indexed with a monoclinic structure with cell parameters consistent with the previous diffraction measurement of BTA·H_2O.[15] Then upon compression, all the reflections persisted from 0.1 GPa to the highest pressure 16.8 GPa, during which no new reflections appeared, indicating no phase transitions occurred in the whole investigated pressure range. When decompressed to ambient pressure, all the reflections were recovered upon decompression, suggesting the crystal structure is reversible in the pressure range of 0-16.8 GPa.

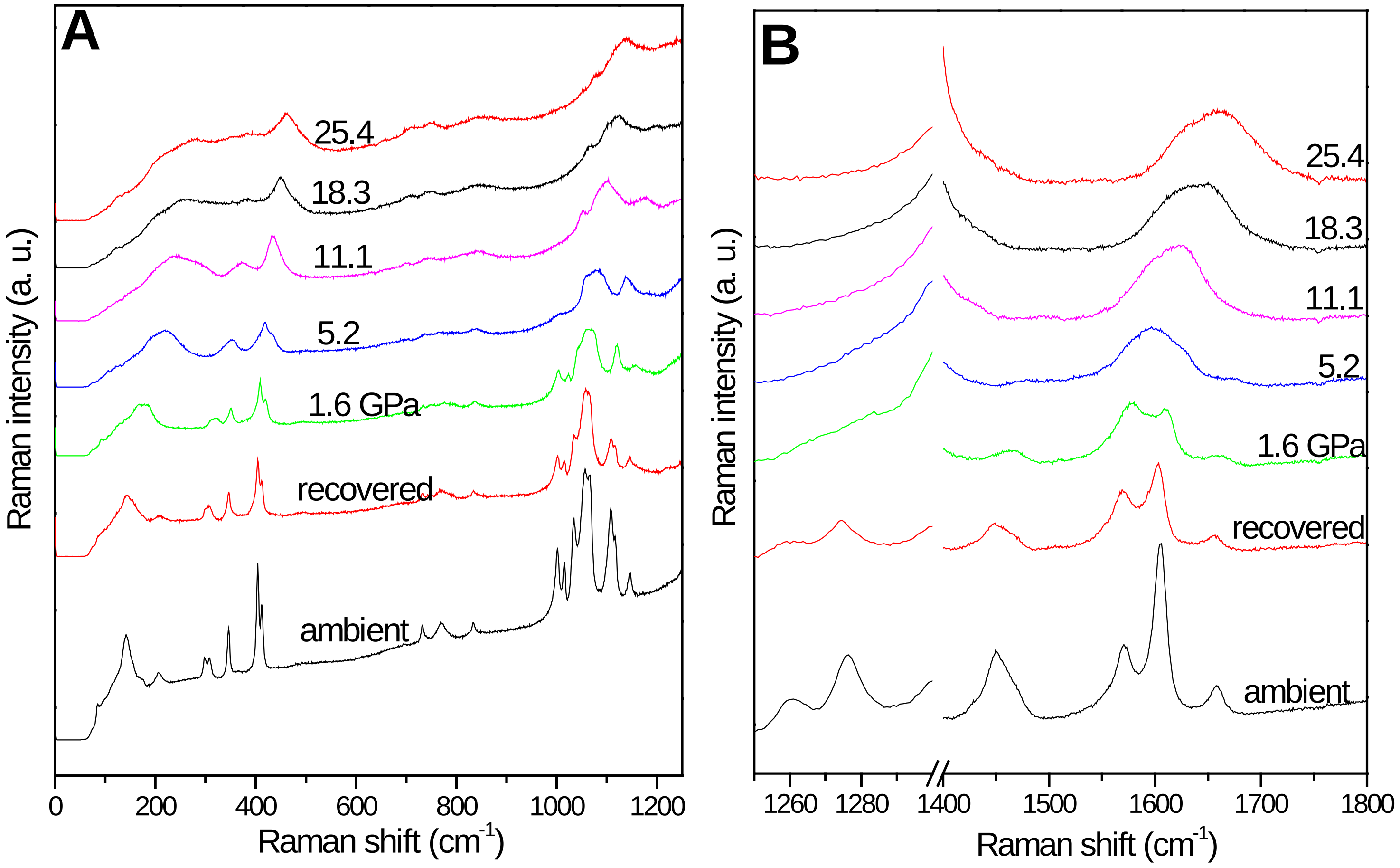

Fig. 3.6 Selected Raman spectra of BTA·H_2O collected at room temperature on decompression in the spectral region of 0-1250 cm^{-1} (A), 1250-1800 cm^{-1} (B) in the pressure region of 0-25.4 GPa. The pressures in GPa are labeled for each spectrum.

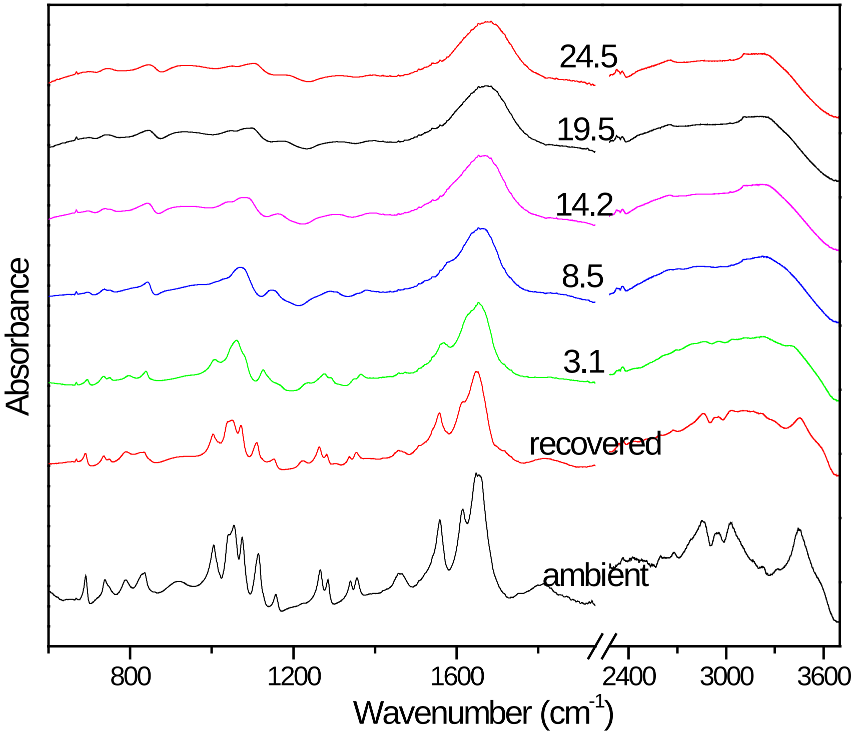

Fig. 3.7 Selected IR spectra of BTA·H_2O collected at room temperature on decompression in the spectral region of 600-3700 cm^{-1} in the pressure region of 0-24.5 GPa. The pressures in GPa are labeled for each spectrum.

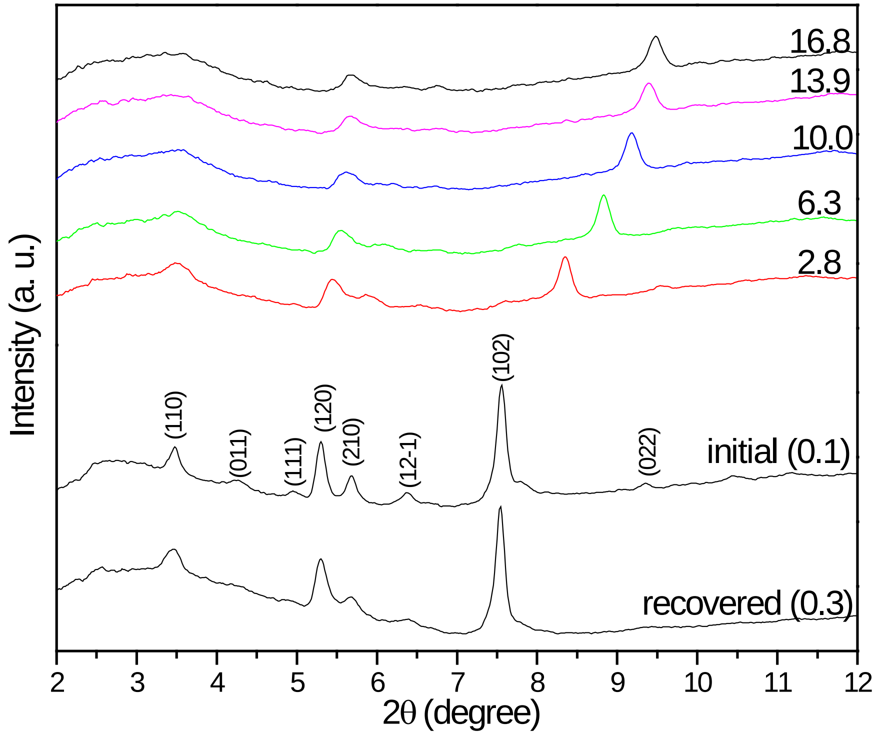

Fig. 3.8 Selected XRD patterns of BTA·H_2O collected at room temperature on compression and decompression in the pressure region of 0-16.8 GPa. The pressures in GPa are labeled for each spectrum.

3.4 Discussion

Our extensive high-pressure Raman and IR results and XRD measurements of $BTA{\cdot}H_2O$ collectively and consistently suggested that no phase transitions occurred in the pressure range of 0-25 GPa. During compression, several interesting phenomenon were observed. Firstly, with increasing pressure, the redshift of the N_{tet}-H stretching mode in 0-12 GPa and the immobilization of the frequency in 12-24.5 GPa indicated the hydrogen bonds was strengthened and stabilized in different pressure regions. Combined with the ambient crystal structure of $BTA{\cdot}H_2O$, we could speculate that the hydrogen atom attached to the tetrazole ring was transferring to the water molecule during compression, and thus formed the $[H_3O]^+$ and the related BTA anion when the hydrogen atom was enough far away from the N atom, which was consistent with Hu's[18] predictions. Then the deprotonated N_{tet} atom had one more extra pair of electrons, which made the tetrazole ring electronic rich. Moreover, according to Thomas *et al.*[15], at ambient conditions, the bond distances of N1-C1 (1.37 Å) and N1-C2 (1.36 Å) (atoms are labeled in Fig. 3.1) are significantly shorter than the C-N single bonds, indicating that there is a delocalization of the amine lone pair and the lone pair is more delocalized on N1-C2 due to the fact that the N1-C1 is a little bit longer than N1-C2. Since the tetrazole ring is electronic rich and the N1-C1 electronic deficient, the electrons may flow from the deprotonated N_{tet} to the N1-C1 bond, which may also contribute to the stability of the tetrazole ring because aromatic rings usually are more stable. All of these possible changes may cause the profile changes of tetrazole ring as well as the appearance of new peaks, such as v_{13}. Apart from $O\text{-}H{\cdots}N_{tet}$, several weaker hydrogen bonds could also be formed between adjacent molecules, which worked as springs to reduce intermolecular interactions, but their intensity was too low to be resolved in Raman and IR spectra. In addition, from the rapid shift of reflection (102) we could know certain axes were compressed rapidly. More detailed and thorough analyses on the Rietveld refinement are needed to figure out the changes and possible mechanisms.

During decompression, very strong hysteresis could be observed, mainly due to the influence of hydrogen bonds. When decompressed to ambient pressure, the spectra of $BTA{\cdot}H_2O$ was fully recovered, which was unusual for five-member heteroaromatic rings[19,20] without chemical reactions taking place at such high pressures. For example, thiophene had two phases in 0-10 GPa and an irreversible incomplete transition occurred at 16 GPa.[20] Furan started the ring-opening reactions at 12 GPa.[19] Apart from that the fact of lacking in hydrogen bonds in those materials, both the furan and thiophene ring would stack in a parallel configuration along a crystalline axis of the cell, and thus favor an efficient overlapping of the π electron densities of the nearest neighbor molecules.[19] Therefore we may infer the tetrazole rings of $BTA\cdot H_2O$ under high pressure may stack in a fashion that is unfavourable for the polymerization, probably due to the orientation of the ring and the intermolecular hydrogen bonds.

Combined with previous work and researches on tetrazole derivatives or tetrazole-containing derivatives[21-25], we could know that nearly all the tetrazole rings have very high stability. Changing the pressure only may not trigger the polymerization easily, other methods such as high pressure and high temperature may promote the synthesis of polymeric nitrogens.

3.5 Conclusion

In situ high-pressure Raman and IR results and XRD patterns collectively proved there were no phase transitions for $BTA\cdot H_2O$ during the compression/decompression cycle in the pressure range of 0-25 GPa. The recovery of the tetrazole ring under high pressure was likely due to the hydrogen bonds, which acted as springs to reduce the stimuli to the crystal or molecules. On the other hand, it was probably due to the orientation and the stack of the tetrazole rings. Through the high-pressure study of $BTA\cdot H_2O$, more understanding of the properties of tetrazole compounds responding to high pressure is known, which will guide the future design and synthesis of energetic materials.

3.6 Acknowledgements

The authors acknowledge funding support from a Research Tools and Instruments Grant from the National Science and Engineering Research Council of Canada, a Leaders Opportunity Fund from the Canadian Foundation for Innovation, an Early Researcher Award from the Ontario Ministry of Research and Innovation and a Petro-Canada Young Innovator Award from the University of Western Ontario, a grant from Defense Research and Development Canada at Suffield.

3.7 References

(1) Vij, A.; Pavlovich, J. G.; Wilson, W. W.; Vij, V.; Christe, K. O. *Angew. Chem. Int. Ed.* **2002**, *41*, 3051.

(2) Dixon, D. A.; Feller, D.; Christe, K. O.; Wilson, W. W.; Vij, A.; Vij, V.; Jenkins, H. D. B.; Olson, R. M.; Gordon, M. S. *J. Am. Chem. Soc.* **2003**, *126*, 834.

(3) Huynh, M.-H. V.; Hiskey, M. A.; Hartline, E. L.; Montoya, D. P.; Gilardi, R. *Angew. Chem. Int. Ed.* **2004**, *43*, 4924.

(4) Klapötke, T. M.; Mayer, P.; Schulz, A.; Weigand, J. J. *J. Am. Chem. Soc.* **2005**, *127*, 2032.

(5) Eremets, M. I.; Gavriliuk, A. G.; Trojan, I. A.; Dzivenko, D. A.; Boehler, R. *Nat. Mater.* **2004**, *3*, 558.

(6) Eremets, M. I.; Popov, M. Y.; Trojan, I. A.; Denisov, V. N.; Boehler, R.; Hemley, R. J. *J. Chem. Phys.* **2004**, *120*, 10618.

(7) Klapötke, T. M. *Struct. Bond.* **2007**, *125*, 85.

(8) Medvedev, S. A.; Trojan, I. A.; Eremets, M. I.; Palasyuk, T.; Klapötke, T. M.; Evers, J. *J. Phys. : Condens. Matter* **2009**, *21*.

(9) Nguyen, M. T. *Coordin. Chem. Rev.* **2003**, *244*, 93.

(10) Wilson, W. W.; Vij, A.; Vij, V.; Bernhardt, E.; Christe, K. O. *Chem. Eur. J.* **2003**, *9*, 2840.

(11) Klapötke, T. M.; Sabaté, C. M. *Chem. Mater.* **2008**, *20*, 3629.

(12) Li, Y.-C.; Qi, C.; Li, S.-H.; Zhang, H.-J.; Sun, C.-H.; Yu, Y.-Z.; Pang, S.-P. *J. Am. Chem. Soc.* **2010**, *132*, 12172.

(13) Klapötke, T. M.; Piercey, D. G. *Inorg. Chem.* **2011**, *50*, 2732.

(14) Fischer, N.; Klapötke, T. M.; Stierstorfer, J.; Wiedemann, C. *Polyhedron* **2011**, *30*, 2374.

(15) Klapotke, T. M.; Mayer, P.; Stierstorfer, J.; Weigand, J. J. *J. Mater. Chem.* **2008**, *18*, 5248.

(16) Schettino, V.; Bini, R. *Phys. Chem. Chem. Phys.* **2003**, *5*, 1951.

(17) Jayaraman, A. *Rev. Sci. Instrum.* **1986**, *57*, 1013.

(18) Hu, A.; Song, Y.; Zhou, L. 2012 private communication.

(19) Ceppatelli, M.; Santoro, M.; Bini, R.; Schettino, V. *J. Chem. Phys.* **2003**, *118*, 1499.

(20) Pruzan, P.; Chervin, J. C.; Forgerit, J. P. *J. Chem. Phys.* **1992**, *96*, 761.

(21) Ciezak, J. A. *Propellants Explos. Pyrotech.* **2010**, *35*, 550.

(22) Ciezak, J. A. *Propellants Explos. Pyrotech.* **2010**, *35*, 373.

(23) Ciezak, J. A. *Propellants Explos. Pyrotech.* **2010**, *35*, 24.

(24) Ciezak, J. A. *Propellants Explos. Pyrotech.* **2011**, *36*, 446.

(25) Ciezak, J. A. *AIP Conf. Proc.* **2012**, *1426*, 1424.

(26) Jonassen, H. B.; Paukert, T.; Henry, R. A. *Appl. Spectrosc.* **1967**, *21*, 89.

Chapter 4 *In situ* high-pressure study of s-triazine and cyanuric triazide by vibrational spectroscopy and X-ray diffraction

4.1 Introduction

Polynitrogen or nitrogen-rich compounds are of particular interests recent years for the large amount of energy they could release during decomposition or detonation, as well as the environmental friendly nitrogen gas as the end-product.[1-4] Compared to the conventional energetic materials, which generate most of their energy by oxidizing the carbon backbones, the energy of the new energetic materials comes from the large energy difference between the N-N or N=N and N≡N bonds. Since high-pressure technique has been proved an effective approach to change the distance between the atoms so as to change the atomic infinity, therefore, it could be used to break the unsaturated bonds and trigger polymerization reaction. The discovery of diamond-like nitrogen, synthesized directly from molecular nitrogen by Eremets *et al.*[5] at pressures above 110 GPa and temperatures above 2,000 K, provided a new and greener way of generating energetic materials by changing pressure and temperature, if compared to the conventional chemical reactions. However, the temperature and pressure of synthesizing the diamond-like nitrogen was too extreme. Moreover, this material could not be recovered at ambient conditions. Accordingly, finding the proper precursor would be the key to synthesize the recoverable polymeric nitrogens.

Based on the previous researches on tetrazole-derivatives[6-10], we could know that they are not favorable to the synthesis of polymeric nitrogens at low pressure and ambient temperature. Therefore, compounds with easier broken unsaturated nitrogen bonds as well as high nitrogen content are favorable. According to the previous high-pressure study on six-member ring systems, such as benzene[11] and pyridine[12], those compounds have ring-opening reactions at about 23 and 22 GPa, respectively. So it could be reasonable to infer that compounds with isoelectric six-member rings could have ring-opening reaction and then further polymerization at lower pressure. In this case, cyanuric triazide (CTA) was chosen as the precursor to study its high-pressure behaviour.

Having the similar ring structure of CTA, s-triazine is a six-membered carbon-nitrogen ring with the nitrogen and carbon atoms alternating and its molecular structure is shown in Fig.

4.1 (A). Having in-depth understanding of the high-pressure behaviour of s-triazine would facilitate the recognition and the explanation of the high-pressure behaviour of CTA. Under ambient pressure, two known phases have been known up to the room temperature. S-triazine has the monoclinic symmetry with space group $C2/c$ below 199 K and upon warm up it transforms to the rhombohedral structure with space group $R\bar{3}c$.[13] When s-triazine is compressed at the room temperature, a phase transition is observed at around 0.4 GPa, evidenced by the discontinuity of the pressure dependence of Raman shifts[14]. Other than this study, the structures and stabilities of s-triazine are completely unknown above 4 GPa.

Containing 82.3% nitrogen by weight, CTA is much more energetic than s-triazine. Under ambient conditions, it crystalizes into a trigonal cell with space group $P\bar{3}$ (C_{3i}^1) and cell parameters $a = b = 8.7456$ Å, $c = 5.8945$ Å, and $V = 390.4$ Å^3.[15] Its molecular structure is shown in Fig. 4.1 (B). Previous computational study predicted that the tri-tetrazole isomer will form at around 27 GPa and a new carbon nitride solid-like cg-N could be formed at 80 GPa and 2,000K.[16] However, no experimental data about the high pressure behavior of CTA are available up to now.

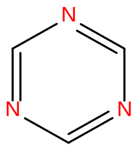

Fig. 4.1 (A) Molecular structure of s-triazine

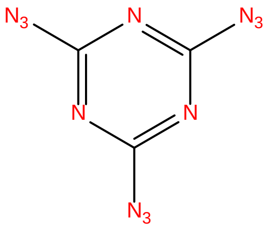

Fig. 4.1 (B) Molecular structure of CTA

Here, we report the *in situ* high-pressure study by Raman and IR measurements on s-triazine and CTA, which were compressed up to 22 GPa and 38 GPa, respectively. Moreover, high-pressure XRD measurement was also performed on CTA in the pressure range of 0-26 GPa. We identified four phase transitions and one irreversible transition for s-triazine, and one partially irreversible transition for CTA during the investigated pressure range.

4.2 Experimental Section

4.2.1 Sample preparation

S-triazine with 97% purity was purchased from Santa Cruz Biotechnology and used without further purification. CTA was synthesized at the University of Ottawa and kept in acetone solution. CTA powder was obtained by evaporating the acetone and the purity was checked before measurements. A symmetrical DAC with two type-I diamonds with 250 μm culets was used for the high-pressure Raman measurements, while a pair of type-II diamonds with a culet size of 350 μm was used for the IR measurements. One ruby (Cr^{3+} doped α-Al_2O_3) chip as the pressure calibrant was carefully placed inside the sample chamber before the sample was loaded. The pressure was determined by using the R_1 ruby fluorescence line shift with an accuracy of ± 0.05 GPa under quasi-hydrostatic conditions[17]. For IR measurements, spectral quality KBr powders were also loaded into the DAC used both as pressure transmitting medium and to dilute the sample.

4.2.2 High-pressure vibrational spectroscopy and XRD measurements

The apparatuses used for Raman, IR and XRD measurements are the same with chapter 2. For each Raman spectrum of s-triazine, a collection time of 30 s was employed, and the average laser power on the sample was maintained at ~ 10 mW. While for CTA, a collection time of 40 s was employed for each Raman spectrum, and the average laser power on the sample was maintained at ~ 5 mW.

4.3 Results

4.3.1 S-triazine

4.3.1.1 Near ambient-pressure Raman and IR spectra

Raman and IR spectra were collected at near ambient conditions as the starting point and are shown in Fig. 4.2. Compared to the IR and Raman study by Larkin *et al.*[18] and Daunt *et al.*[19] on condensed phase of s-triazine, our measurements are in close agreement with theirs as can be seen from Table 4.1. We followed the assignment proposed by Larkin *et al.*[18] and labeled the modes accordingly in Table 4.1. In addition, we also observed two Raman bands at 79 and 108 cm^{-1} in the lattice region, agreed with previous study[14].

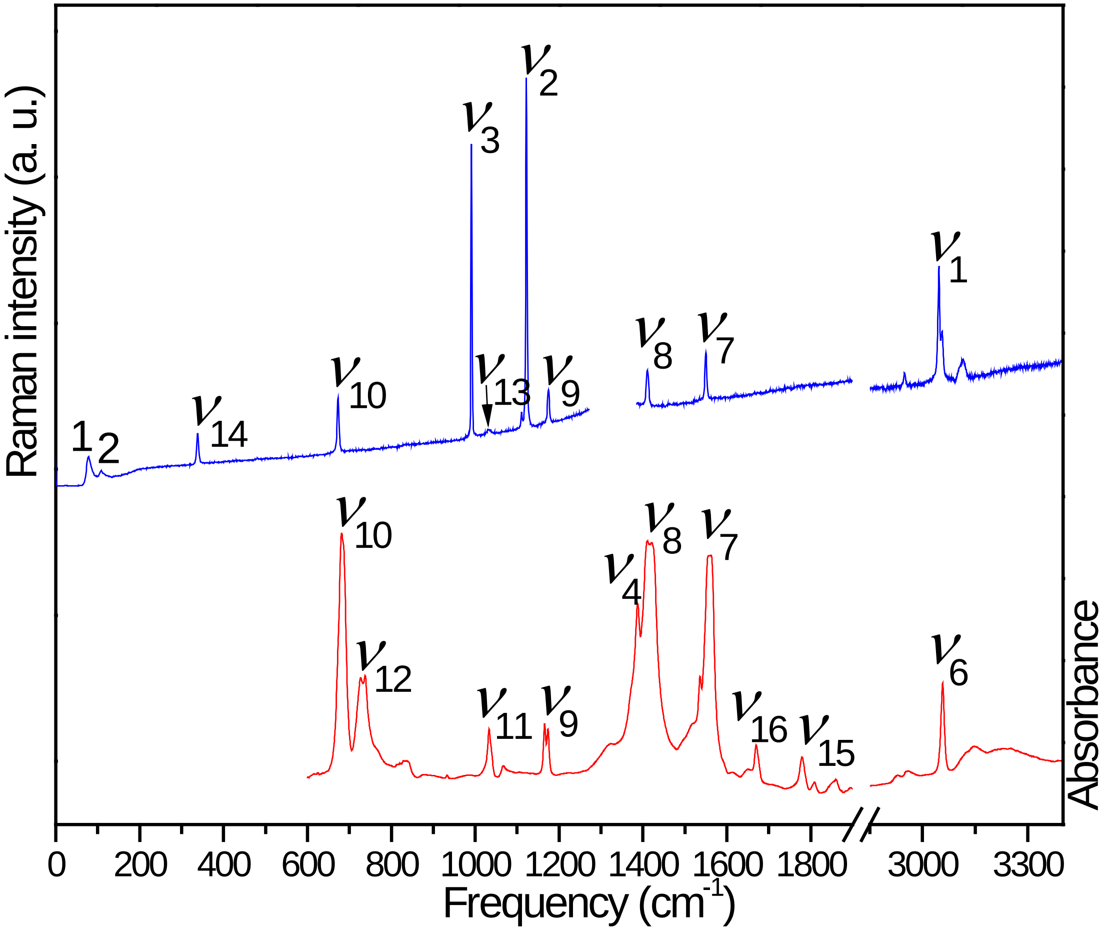

Fig. 4.2 Raman spectrum of s-triazine (top) in comparison with IR spectrum (bottom) in the spectral region 0-3400 cm^{-1} both collected at near ambient pressure and room temperature. The omitted spectral regions are due to the lack of spectroscopic features. The assignment of the vibrational modes is labeled above each.

Table 4.1 Assignment and frequencies (cm^{-1}) of observed Raman and IR internal modes of s-triazine in comparison with reference values.

Mode	Symmetry	Description	This work		References[18]	
			Raman [a]	IR [b]	Raman	IR
v_6	E'	CH stretch (out of phase)	3055	3064	-	3057
v_1	A'_1	CH stretch (in phase)	3046	-	3043	-
v_{15}	?	?	-	1778	-	-
v_{16}	?	?	-	1671	-	-
v_7	E'	Quadrant stretch, ring+CH rocking	1550	1563	1548	1557
v_8	E'	CH rocking + ring semi-circle stretch	1410	1419	1404	1410
v_4	A'_2	CH rocking, in-phase	-	1389	1358	1367
v_9	E'	Semi-circle stretch, ring+CH rocking	1175	1165	1171	1172
v_2	A'_1	C radial (in phase)	1122	-	1123	-
v_{13}	E''	CH wag, (out of phase)	1033	-	1031	-
v_3	A'_1	N-radial (in phase)	991	-	991	-
v_{11}	A''_2	Sextant out-of-plane bend +CH wag	-	1033	-	927
v_{12}	A''_2	Sextant out-of-plane bend, ring	-	740	-	737
v_{10}	E'	Quadrant in-plane bend, ring	673	682	675	676
v_{14}	E''	Quadrant out-of-plane bend, ring	338	-	338	-
2		Lattice mode	108	-	-	-
1		Lattice mode	79	-	-	-

[a] Raman spectrum was obtained at 0.6 GPa.

[b] IR spectrum was obtained at 0.3 GPa.

[c] Mode v_{16} was assigned based on 5-aminotetrazole[20].

4.3.1.2 Raman spectra on compression

We collected Raman spectra of s-triazine upon compression to 17.7 GPa with selected spectra shown in Fig. 4.3 (A). When compressed to 0.9 GPa, a new mode labeled as 3 at 82 cm^{-1} appeared in the lattice region, suggesting a possible transition. Further compression to 1.8 GPa resulted in the appearance of another lattice mode at 112 cm^{-1} (labeled as 4). Then mode 1 disappeared upon subsequent compression to 5.1 GPa. With increasing pressure to 14.7 GPa the remaining lattice modes disappeared, indicating the amorphization of the

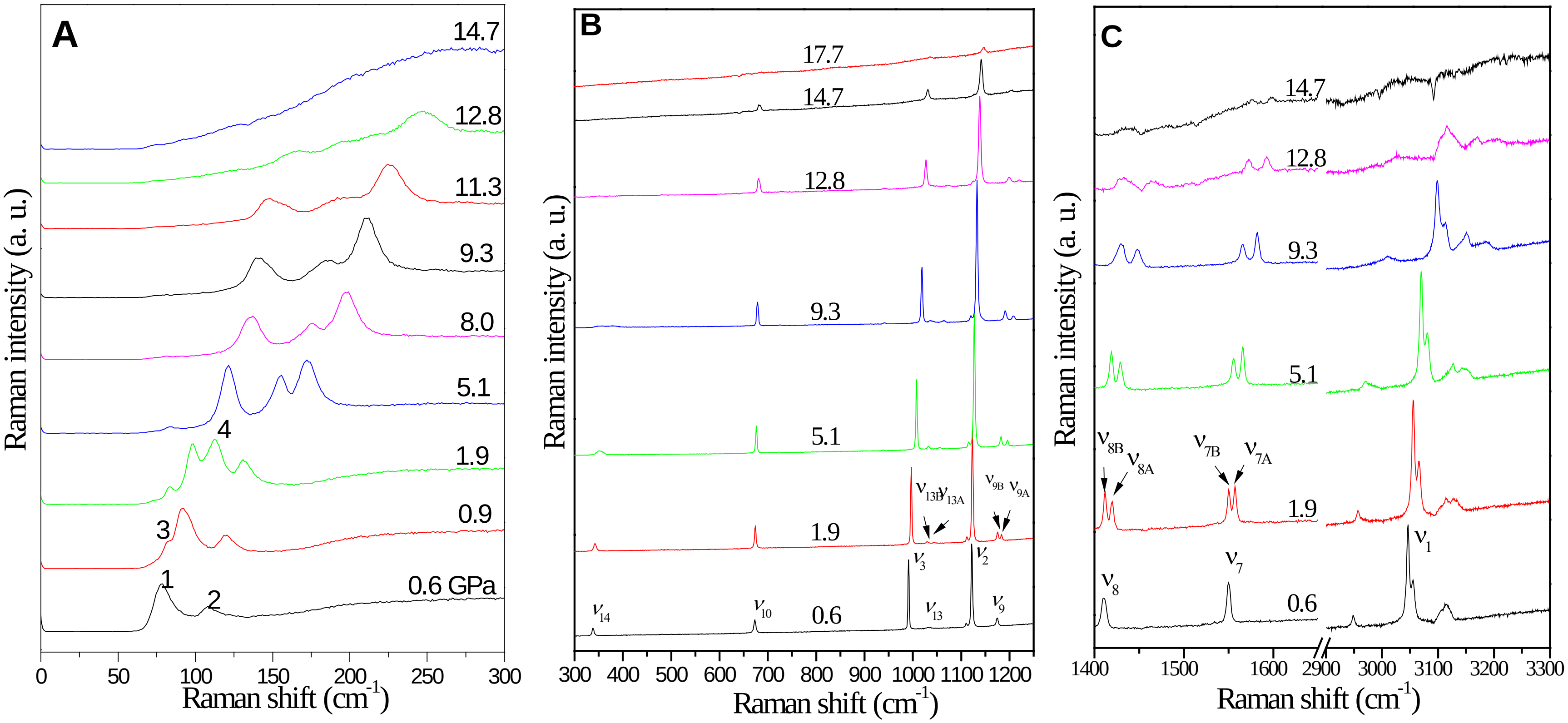

Fig. 4.3 Selected Raman spectra of s-triazine collected at room temperature upon compression in the region of 0-300 cm^{-1} (A), 300-1250 cm^{-1} (B), 1400-3300 cm^{-1} (C). The pressures in GPa are labeled for each spectrum. The assignments are labeled for Raman modes (see text).

material. Each of the change of the lattice modes may suggest a possible phase transition.

In the internal region of 300-1250 cm^{-1} and 1400-3300 cm^{-1}, shown in Fig. 4.3 (B) and 4.3 (C), the Raman spectra showed no prominent changes upon compression. Then splitting of ring vibration related modes v_7, v_8, v_9 and v_{13} were observed when compressed to 1.9 GPa. Upon further compression to 5.1 GPa, the peak intensity of v_2 and v_{10} increased significantly, and ceased to grow at 9.3 GPa. Above 12.8 GPa, all modes exhibited significant weakening, leaving only three bands, v_2, v_3 and v_{10} observable in the spectral region. Among those three modes only mode v_2 persisted to the highest pressure 17.7 GPa.

4.3.1.3 Pressure depndence of Raman lattice modes

The observed changes of the Raman lattice modes clearly indicate pressure-induced phase transitions. By examining the pressure dependences (dv/dP) of the lattice modes the transition boundaries may be better understood. The pressure dependence of the Raman shifts of the lattice modes of s-triazine is shown in Fig. 4.4 and Table 4.2. The slopes of Raman shifts were determined by linear regressions. In general, the frequencies of all lattice modes blueshifted with increasing pressure, but in different regions the slopes were different, as can be seen from Table 4.2. The different shift slopes clearly clarify the phase boundaries of new phases (labeled as I, II, III, IV, and V).

4.3.1.4 IR spectra on compression

Supplementary to the Raman measurements, we collected mid-IR spectra for s-triazine upon compression in the pressure range of 0-22 GPa, as shown in Fig. 4.5. When compressed to 2.0 GPa, splitting was observed for modes v_9, v_{11} and v_{12}. Then at 4.4 GPa, two new modes (labeled as v_{17} and v_{18}) located at 1142 and 935 cm^{-1} appeared, accompanied by the splitting of the mode v_7. At the same time, the CH stretch mode v_6 was strengthened and became prominent at 6.2 GPa, which then split into a doublet upon further compression to 10.9 GPa. With increasing pressure, the doublet of the mode v_{12} (v_{12A} and v_{12B}) began to merge. At the highest pressure 22.2 GPa, the C=N stretching mode v_{16} evolved into a broad band on the shoulder of the mode v_{7A}, and all the ring vibration modes existed but were significantly weakened and with broadened profiles.

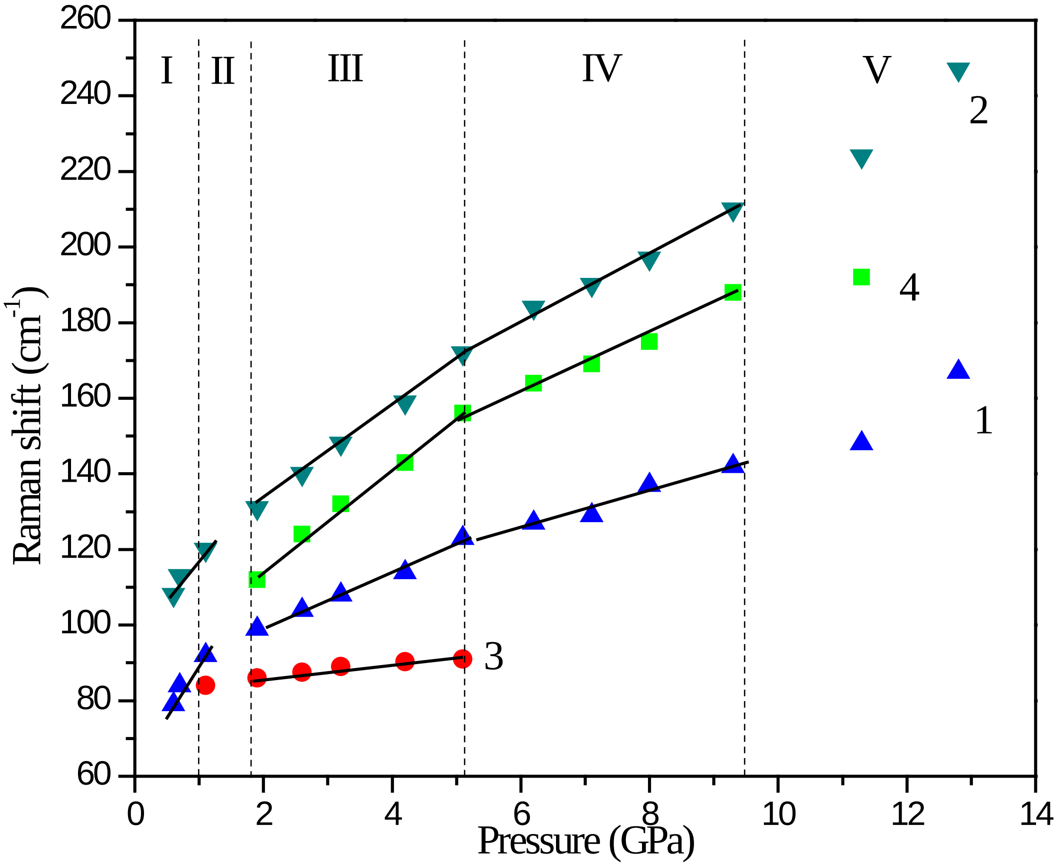

Fig. 4.4 (Color online) Raman shift of s-triazine as a function of pressure on compression in the lattice modes region. Solid straight lines are linear fits to the data. Vertical dashed lines marked the suggested phase transition boundaries. Different symbols denote lattice modes with different origins with numbers labeled from low to high frequencies. See text and Fig. 4.3 (A).

Table 4.2 Pressure dependence (*dv*/*dP*) of the Raman lattice modes for different phases.

	dv/*dP* (cm^{-1}/GPa)				
	Phase I	Phase II	Phase III	Phase IV	Phase V
Lattice mode	(0-0.9 GPa)	(0.9-1.9 GPa)	(1.9-5 GPa)	(5-9 GPa)	(9-15 GPa)
1	23.0		5.9	4.5	7.1
2	28.2		12.8	9.0	10.6
3			1.6	2	
4			13.8	7.6	

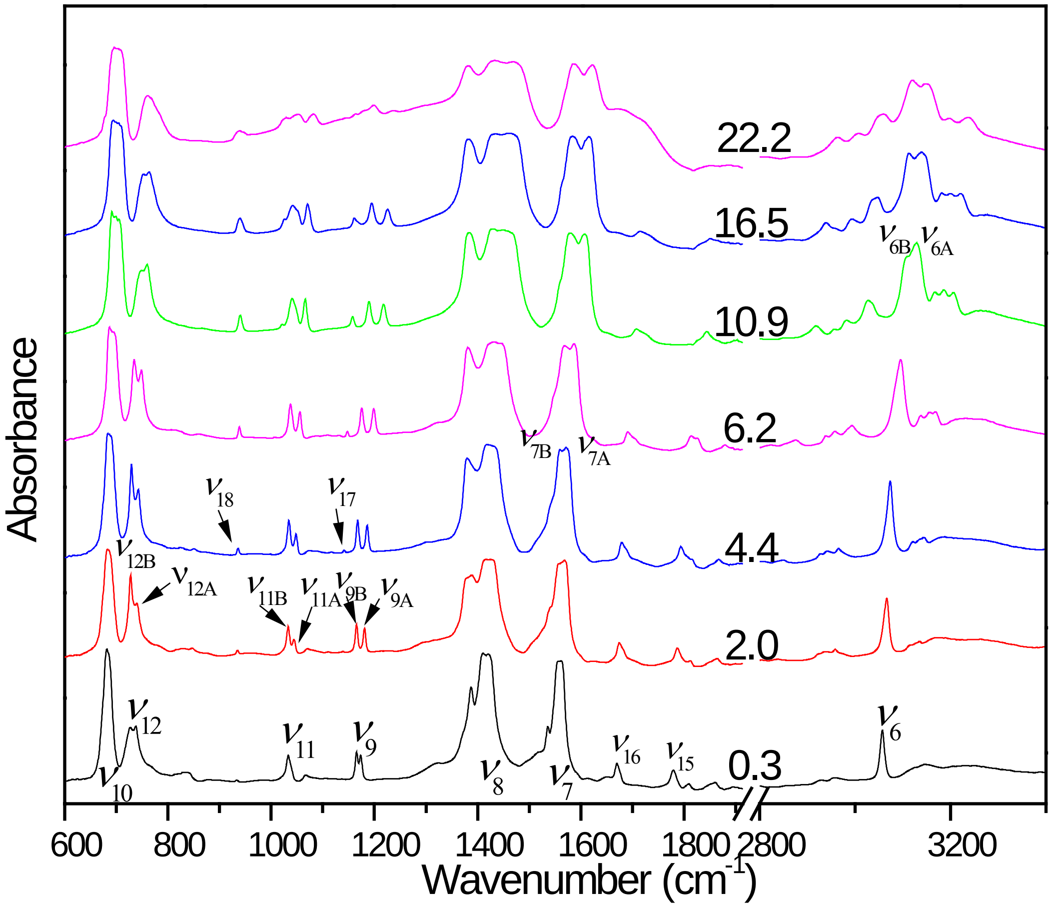

Fig. 4.5 Selected IR spectra of s-triazine collected at room temperature on compression in the spectral region of 600-3400 cm^{-1} in the pressure region of 0.3-22.2 GPa. The pressures in GPa are labeled for each spectrum. The assignments are labeled for IR modes (see text).

4.3.1.5 Raman and IR spectra on decompression

Raman and IR spectra were also collected on decompression all the way down to near-ambient pressure in order to better understand the pressure-induced structural evolutions and the high-pressure stability of s-triazine. Fig. 4.6 (A) and 4.6 (B) were selected Raman and IR spectra of s-triazine, respectively. As can be seen from the Raman spectra, lattice modes were not recovered upon decompression to near-ambient pressure, indicating that the transformation was irreversible in the compression/decompression cycle. For the Raman internal modes, only modes ν_2, ν_3 and ν_{10} were recovered. However, nearly all the modes were recovered in the IR spectra, with the difference being that the C=N stretching mode ν_{16} was not recovered, replaced by a broad band located at 1630 cm^{-1}. The discrepancy between

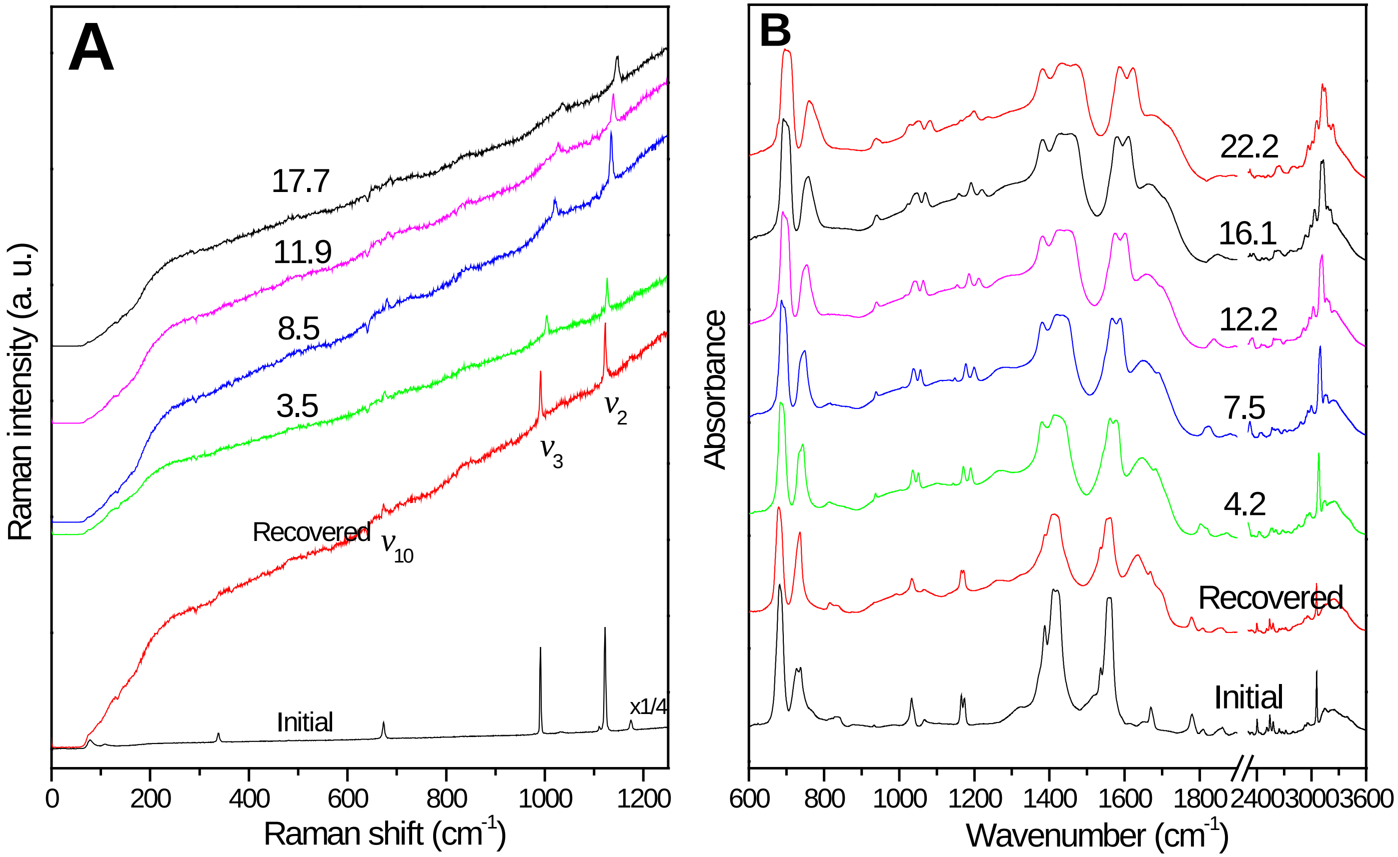

Fig. 4.6 **(A)** Selected Raman spectra of s-triazine collected at room temperature on decompression in the region of 0-1250 cm^{-1} at pressures of 0.5-17.7 GPa. The spectra in the region of 1250-3300 cm^{-1} were omitted because of the lack of Raman features. **(B)** Selected IR spectra of s-triazine collected at room temperature on decompression in the spectral region of 600-3600 cm^{-1} in the pressure region of 0.6-22.2 GPa. The pressures in GPa are labeled for each spectrum. The assignments are labeled for each mode (see text).

the Raman and IR recovered spectra may due to that the ring is destroyed at high pressure to form disordered structure but the yield of the ring-opening reaction is low. And the disordered form has no prominent Raman freatures, but its functional groups may be similar to s-triazine, and thus contribute to the similar IR absorption.

4.3.2 CTA

4.3.2.1 Ambient-pressure Raman and IR spectra

Raman and IR spectra were collected at ambient conditions as the starting point and are shown in Fig. 4.7. Compared to results of Shearer *et al.*[21], our results are in very good agreement as can be seen from Table 4.3.

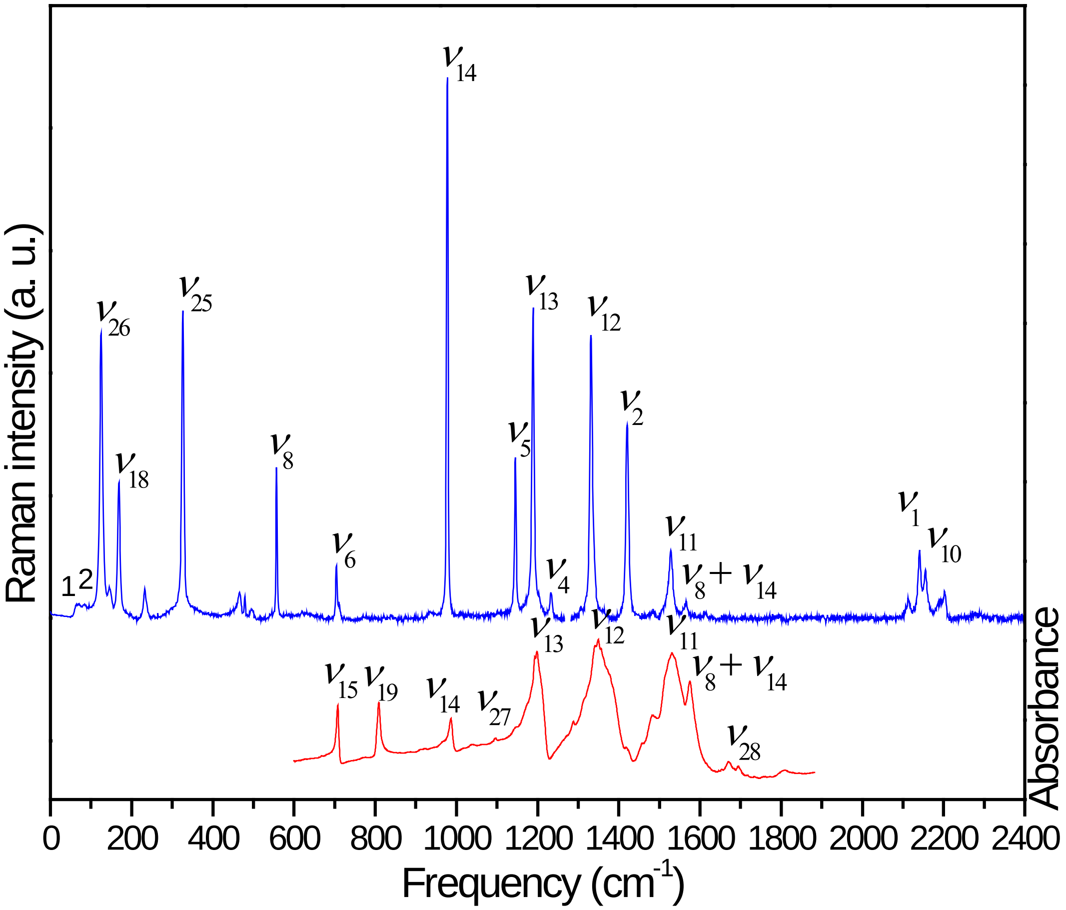

Fig. 4.7 Raman (top) and IR (bottom) spectra of CTA in the spectral region 0-2400 cm^{-1} were both collected at near ambient conditions. The omitted spectral regions are due to the lack of spectroscopic features. The assignment of the vibrational modes is labeled above each.

Table 4.3 Assignment and frequencies (cm^{-1}) of observed Raman and IR internal modes of CTA in comparison with reference values.

Mode	Description	Symmetry	This work		References[21]	
			Raman	IR	Raman	IR
$v_4 + v_{14}$			2203	-	2213	2190
v_{10}	N_3 asym stretch	A"	2157	-	2167	2150
v_1	N_3 asym stretch	A'	2142	-	2154	-
$v_5 + v_{14}$			2117	-	2130	2110
v_{28}	C=N stretch	?	-	1675	-	-
$v_8 + v_{14}$			1529	1572	1543	1570
v_{11}	Ring deformation	E'	-	1532	-	1525
v_2	Ring stretch	A'	1422	-	1437	-
v_{12}	Ring deformation	E'	-	1351	1346	1342
v_4	N_3 sym stretch	A'	1234	-	1227	-
v_{13}	N_3 sym stretch	E'	1190	1197	1204	1194
v_5	Ring deformation	A'	1146	-	1162	-
v_{27}	?	?	1096	-	-	-
v_{14}	Ring-N stretch	E'	979	985	993	980
v_{19}	Ring deformation	A"	-	809	-	804
v_6	Ring twist	A'	706	-	723	-
v_{15}	Ring deformation	E'	-	707	-	703
v_8	Ring breathing	A'	559	-	570	-
v_{25}	N_3 wag	E"	327	-	340	-
v_{18}	CN_3 bend	E'	170	-	183	-
v_9	CN_3 bend	A'	148	-	157	-
v_{26}	N_3 twist	E"	126	-	142	-
2	Lattice mode		82	-	100	-
1	Lattice mode		67	-	77	-

4.3.2.2 Raman spectra on compression

Starting from ambient pressure, Raman spectra of CTA were collected upon compression to 39 GPa with selected spectra depicted in Fig. 4.9. Upon compression to 0.4 GPa, modes 1 and 2 in the lattice region were strengthened and became prominent at 3.5 GPa, whereas modes v_{14}, v_{18} and v_{26} were significantly weakened. Then at 6.9 GPa, splitting was observed for the ring twist mode v_6 and the N_3 symmetric stretching mode v_{13}, which was likely due to pressure-enhanced intermolecular interactions. With increasing pressure to 14.2 GPa, the lattice modes were drastically weakened and broadened, accompanied by the merge of modes v_5 and v_{13}. Then upon subsequent compression to 18.1 GPa, lattice modes were completely depleted, indicating CTA had been amorphous. Moreover, only modes v_{14} and v_{25} persisted at

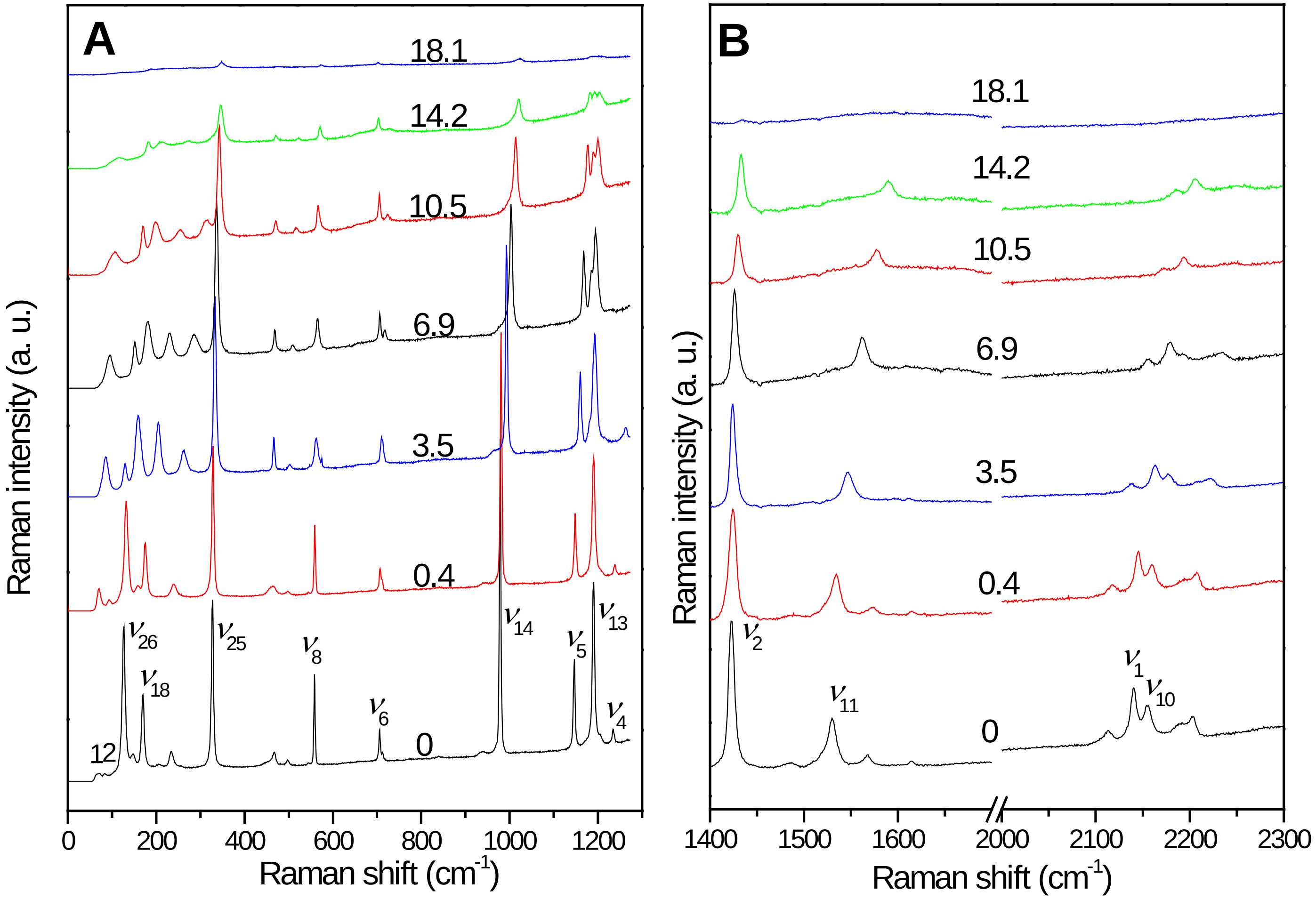

Fig. 4.8 Selected Raman spectra of CTA collected at room temperature on compression in the spectral region of 0-1250 cm^{-1} (A), 1400-2300 cm^{-1} (B) in the pressure region of 0-37.4 GPa. The pressures in GPa are labeled for each spectrum. The assignments are labeled for Raman modes (see text). The spectra above 18.1 GPa are omitted because no Raman peaks were observed.

this pressure. When compressed > 18.1 GPa, all the modes disappeared. According to Hu *et al.*[16], CTA will form tri-tetrazole isomer at about 27 GPa and therefore, we decided to compress further. Upon further compression to 26 GPa, the sample color changed to dark red. And the color became darker with increasing pressure, similar to the phenomenon of polymerization occurred to sodium azide[22] and may suggest the possible chemical transformation.

4.3.2.3 IR spectra on compression

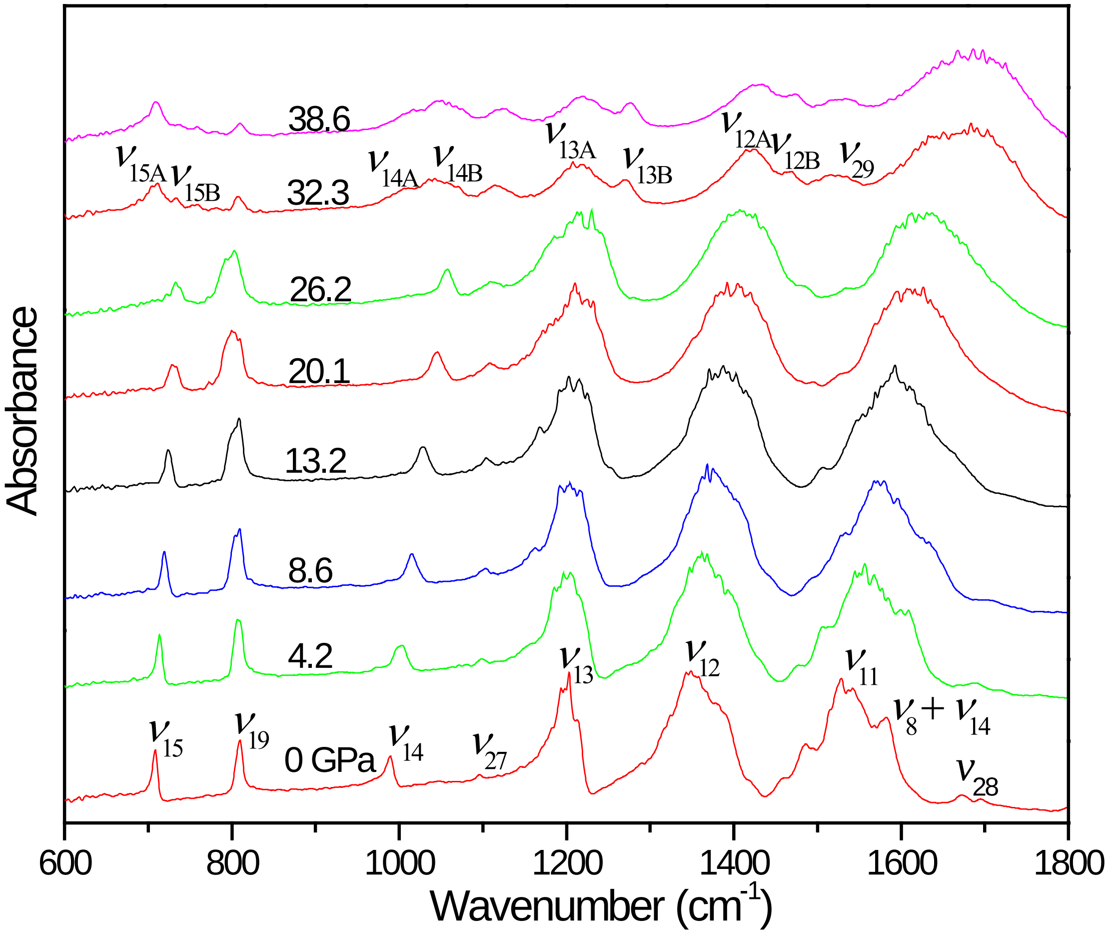

Fig. 4.9 Selected IR spectra of CTA collected at room temperature on compression in the spectra region of 600-1800 cm^{-1} in the pressure region of 0-38.6 GPa. The pressures in GPa are labeled for each spectrum. The assignments are labeled for IR modes (see text).

Mid-IR spectra of CTA were collected on compression to 38.6 GPa. Selected absorption spectra as a function of pressure in the spectral region of 600-1800 cm^{-1} are depicted in Fig.

4.9. No obvious changes could be observed upon compression to 4.2 GPa, then the mode v_8+v_{14} was weakened and disappeared at 8.6 GPa. At the same time, the mode v_{27} was strengthened and became prominent upon further compression. With increasing pressure, all the modes were broadened gradually. When compressed to 26.2 GPa, sample colour changed to dark red, consistent with the Raman results. Then as the pressure was increased to 32.3 GPa, profiles of IR changed obviously and splitting was observed for several IR modes, such as the ring deformation modes v_{12} and v_{15}, the N_3 symmetric stretching mode v_{13} and the ring-N stetching mode v_{14}, with each splitting labeled in Fig. 4.9. In addition, a new mode, labeled as v_{29}, appeared at 1524 cm^{-1}. The profile changes of ring vibration modes and the appearance of the new peak, as well as the darkening of sample color suggested the polymerization occurred. Upon further compression to the highest pressure 38.6 GPa, all the modes persisted but the intensity was severely reduced and with more broadened profiles.

4.3.2.4 Pressure effects on Raman and IR modes

The pressure dependence of the observed Raman and IR modes of CTA were examined by plotting the vibrational frequencies as a function of pressure as shown in Fig. 4.10 (A) and (B). In general, all the Raman modes exhibited pressure-induced blue shifts, in agreement with bonds became stiffened upon compression. However, due to the weak intensity, modes could not be observed above 18 GPa from Raman. Complementary to the Raman modes, IR modes of CTA could persist up to around 39 GPa. All the IR modes frequencies increased linearly with increasing pressure, in agreement with the Raman spectra that there were no phase transitions in the whole pressure range.

4.3.2.5 Raman and IR spectra on decompression

In order to understand the high-pressure stability and the structural evolutions of CTA, Raman and IR spectra were collected on decompression to near-ambient pressure. Starting from 38.6 GPa, Raman spectra of CTA were collected upon decompression to near-ambient pressure with recovered spectra depicted in Fig. 4.11 (A). Because of the small size of the laser beam, the Raman spectra of different part of sample were collected and labeled in the image. As can been seen from spectrum *a*, upon decompression to ambient pressure, only few internal modes were recovered and with much weaker intensity. Moreover, the lattice modes were not recovered, indicating the transformation during the

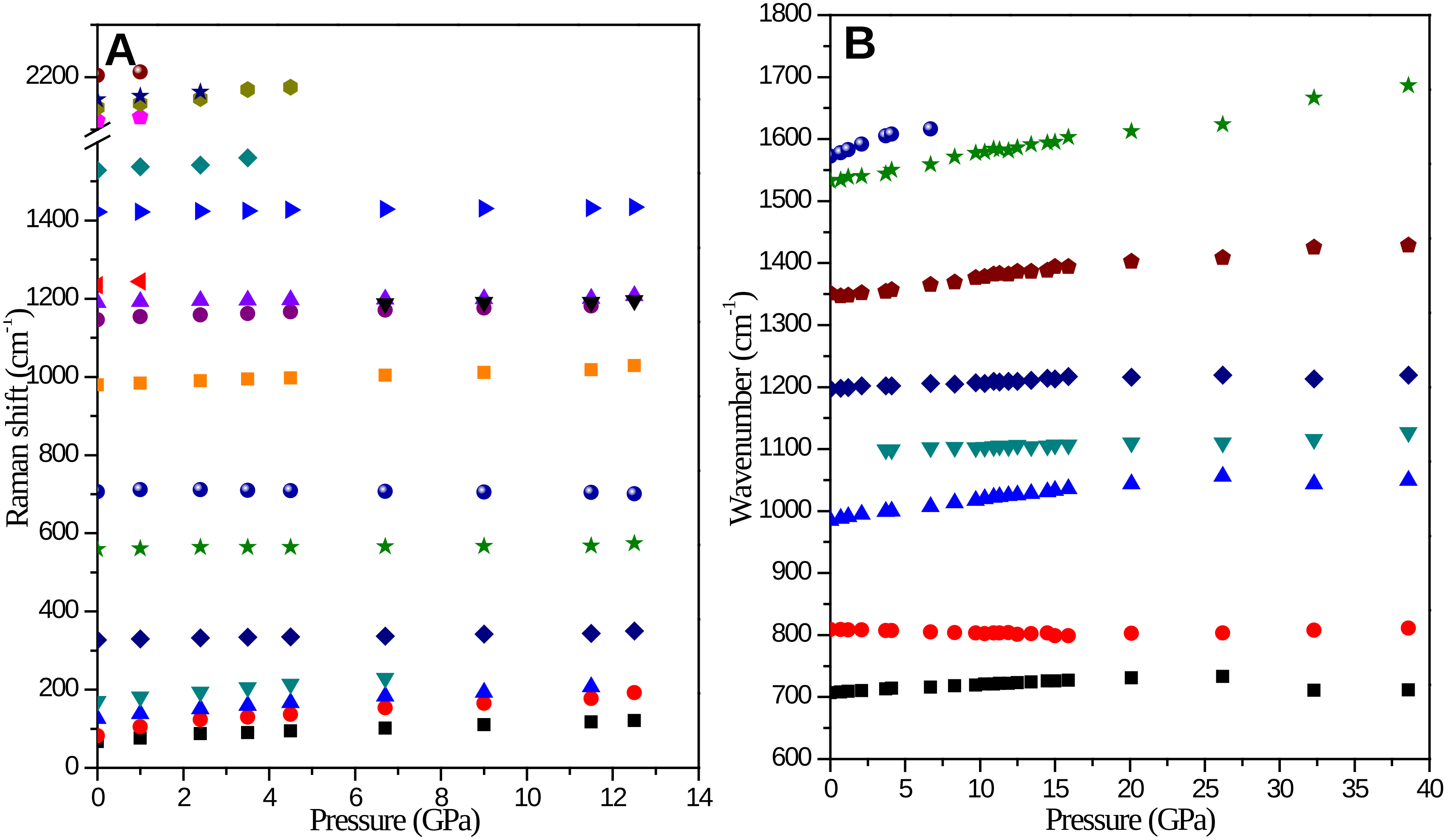

Fig. 4.10 Pressure dependence of Raman shifts (A) and IR frequencies (B). Different symbols represent modes with different origins of assignments.

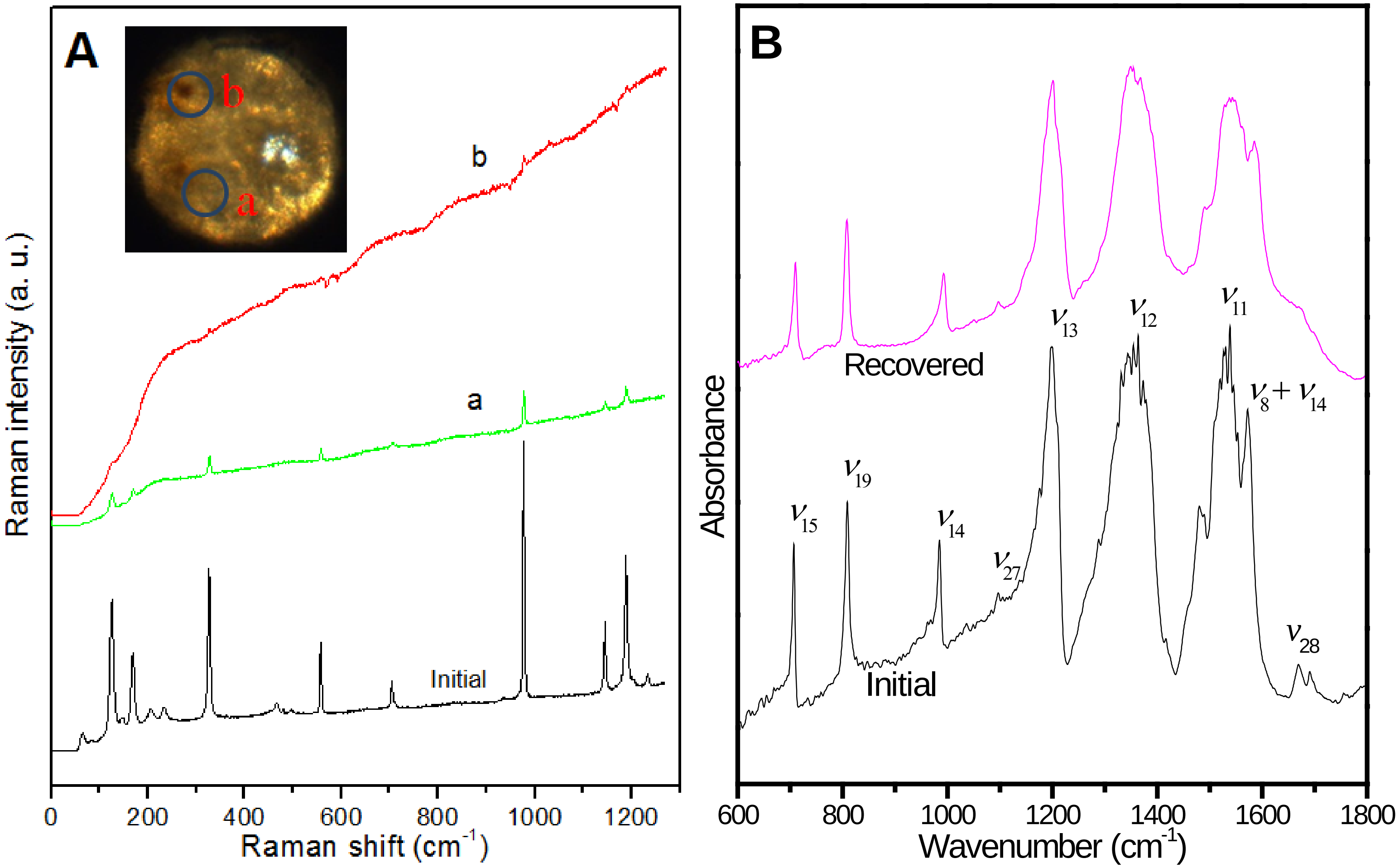

Fig. 4.11 (A) Raman spectra of recovered CTA at ambient conditions. Different color represent different parts of the sample (see the inset image). **(B)** IR spectra of recovered CTA at ambient conditions.

compression/decompression cycle was irreversible in the whole pressure range. However, for spectrum *b*, which was collected far away from the position where spectrum *a* was collected, both the lattice modes and internal modes were not recovered, suggesting that the molecular structure of CTA were destroyed at high pressure. In addition, the color of recovered sample as well as the evolution of color changes was monitored to compare the changes, which is shown in Fig. 4.12. Different from the Raman spectra, the IR spectra is the average absorbance of the sample in the hole drilled in the gasket. The recovered IR spectrum of CTA, shown in Fig. 4.11 (B), is very similar to the spectrum before compression. But the the C=N stretching mode was not recovered, indicating a possible structure change of the triazine ring. Therefore, based on the recovered Raman and IR results, we infer that the ring structure has been mostly destroyed when decompressed to ambient pressure and thus form the disordered structure. The disordered form has no prominent Raman features, but the functional groups of the disordered maybe similar to CTA, thus exhibits similar IR absorptions.

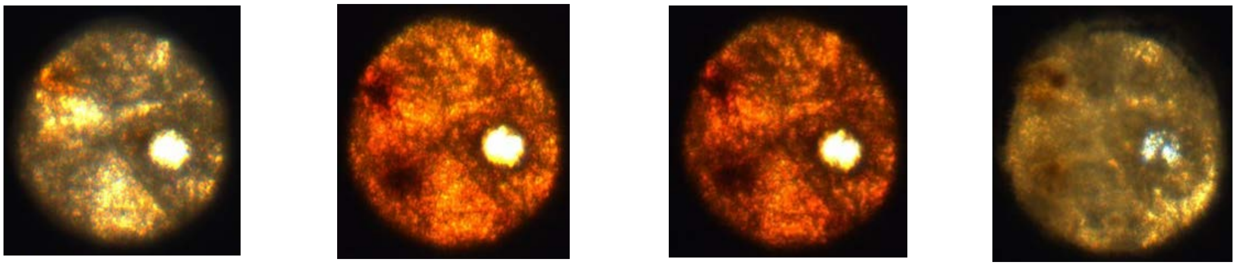

Ambient 26 GPa 39 GPa Recovered

Fig. 4.12 Evolution of sample color changes at different pressures. The bright spot is the ruby.

4.3.2.6 XRD pattern of CTA on compression and decompression

Supplementary to the Raman and IR results, XRD pattern of CTA in the compression and decompression process were collected with selected XRD pattern shown in Fig. 4.13. The diffraction pattern at near ambient pressure can be indexed with a trigonal structure with cell parameters, consistent with the previous result of CTA.[15] Upon compression, all the reflections were found to persist to 14.2 GPa as indicated by the consistent indexing of the reflections associated with this phase. Upon subsequent compression, several reflections began to disappear and only four reflections existed at the highest pressure. Upon decompression, all the reflections were recovered, indicating the crystal structure was reversible in the pressure range of 0-25.7 GPa.

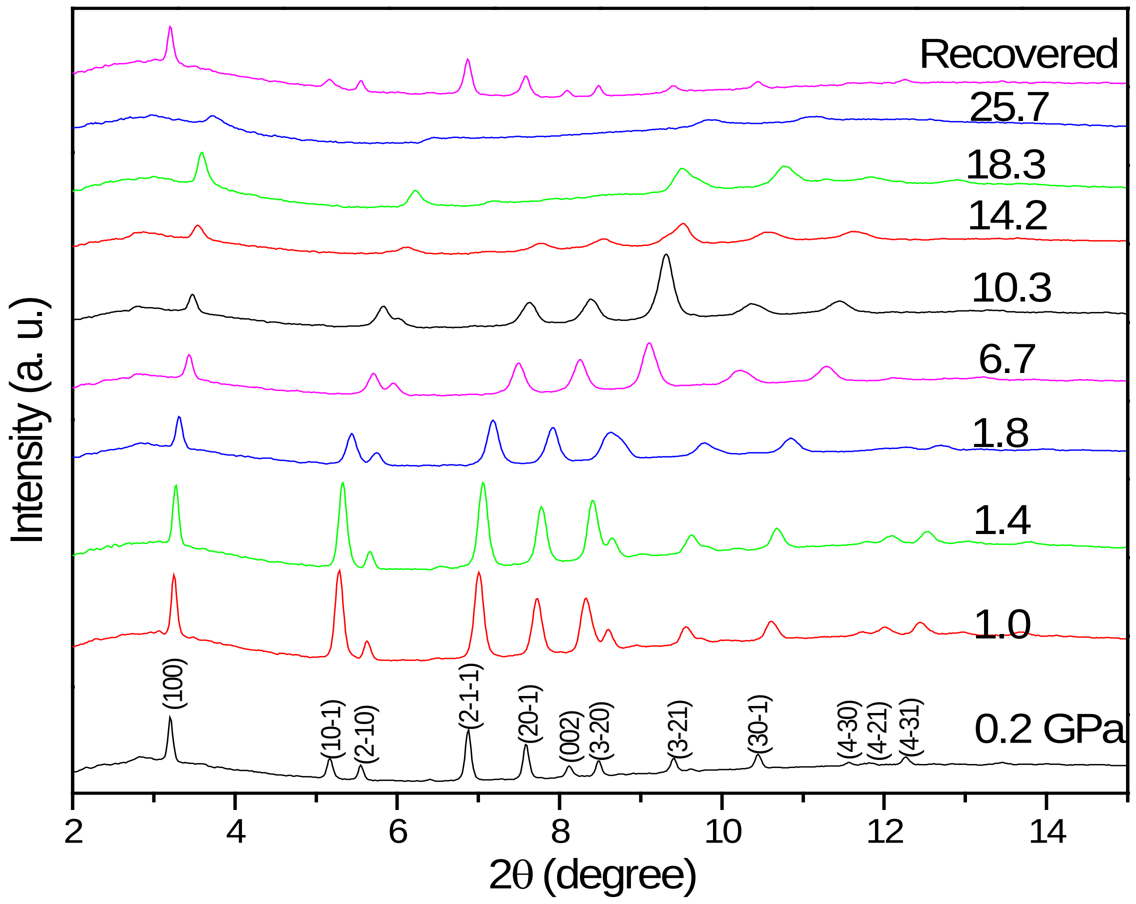

Fig. 4.13 X-ray diffraction patterns of CTA on compression and decompression at selected pressures.

4.4 Discussion

Our extensive Raman and IR measurements of s-triazine on compression consistently suggest the existence of several distinct phases with boundaries at around 0.9, 1.8, 5 and 9 GPa. All the transitions are associated with changes in crystal lattices or/and molecular structures. Upon compression to 2.0 GPa, two new lattice modes were found at 0.9 and 1.8 GPa, respectively. However, according to Dove *et al.*[23], the corresponding pressures were 0.5 and 0.8 GPa. The pressure discrepancy was likely due to the power of laser during the Raman measurements. In this work, a much weaker laser was used to avoid the potential laser-induced polymerization. Although the occurrences of the new modes were at different pressures, the profile of peaks was very similar. Then with increasing pressure, two more phase transitions were observed at 5 and 9 GPa, evidenced by the change of pressure dependence of Raman lattice modes, as well as the splitting and appearance of new modes both in the Raman and IR spectra. Upon decompression, the recovered Raman and IR spectra collectively suggested the formation of disordered structure as well as the ring-opening reaction with low yield.

Since s-triazine is isoelectric to benzene and pyridine, comparing high-pressure behaviors of benzene and pyridine with s-triazine may provide in-depth understanding of the nature of the transformations. S-triazine crystallizes into a rhombohedral structure at ambient conditions[13], which is different from the orthorhombic structure of benzene and pyridine of phase I. When compressed to 0.9 GPa, it transforms to the monoclinic structure[13], same as the structure of benzene and pyridine of phase II although the detailed space groups are different[12,24]. Upon further compression, the crystal structure is unknown due to the lack of XRD data, and the high pressure phases of these three compounds are compared and reported in Table 4.4. As can be seen, very large misalignment of phase transition pressures exists between s-triazine and pyridine or benzene, suggesting that the detailed crystal structure and phase stabilities differ between the corresponding phases. At around 23 GPa, all three compounds have ring-opening and polymerization reactions, but the difference is that the yield of s-triazine polymer is low, evidenced by the similar recovered IR spectra.

For CTA, our spectroscopic measurements and XRD data collectively indicated that during compression there were no phase transitions in the pressure range of 0-26 GPa, and one chemical reaction at above 26 GPa. Below 26 GPa, the XRD patterns showed no prominent changes, therefore, the appearance of the new modes and the splitting observed both in Raman and IR spectra were likely due to the changes of the orientation of the ring or the pressure-enhanced intermolecular interactions. When compressed > 26 GPa, the significant changes of the IR profile and the changes of sample color suggested the polymerization, also evidenced by the irreversible changes of the Raman and IR modes. According to Hu *et al.*'s[16] theoretical calculation, two possible reactions could occur at above 22 GPa. One is the intramolecular polymerization at about 27 GPa, which lead to the formation of tri-tetrazole $(CN_4)_3$ isomer. Another form is the intermolecular polymerization at 80 GPa and 2000K, which caused the sp^2 to sp^3 orbital transformation of carbon atoms. Given the fact that the sample colour changed at 26 GPa as well as the profile changes of IR spectra at the similar pressure, we propose the intramolecular polymerization may occur in this work. And more detailed analyses of the XRD patterns of CTA at high pressures are needed to clarify the molecular structure as well as the transition mechanism.

Table 4.4 Summary of observed high-pressure solid phases of s-triazine in comparison with those of benzene and pyridine

	S-triazine ($C_3H_3N_3$)	Pyrindine (C_5H_5N)	Benzene (C_6H_6)
Phase	I	I	I
Pressure range	0-0.9 GPa	1-2 GPa	0.07-1.4 GPa
Crystal structure	$R\bar{3}c$ (C_{3v}^{6}) [a]	$Pna2_1$(C_{2v}^{9}) [b]	$Pbca$(D_{2h}^{15}) [c]
Phase	II	II	II
Pressure range	0.9-2 GPa	2-8 GPa	1.4-4 GPa
Crystal structure	Monoclinic [d]	Monoclinic [b]	Monoclinic [e]
Phase	III	III	III
Pressure range	2-5 GPa	8-11 GPa	4-11 GPa
Crystal structure	?	Monoclinic [b]	Monoclinic [e]
Phase	IV	IV	IV
Pressure range	5-9 GPa	11-16 GPa	11-17 GPa
Crystal structure	?	Monoclinic [a]	Monoclinic [e]
Phase	V	V	V
Pressure range	9-15 GPa	16-22 GPa	17-23 GPa
Crystal structure	?	Monoclinic [b]	Monoclinic [e]
Chemical transformation	> 22 GPa	> 22 GPa	> 23 GPa
Yield	Low	High	High

[a] Reference [25].

[b] Reference [12].

[c] Reference [26].

[d] Reference [13].

[e] Reference [27].

Due to the fact that s-triazine is the framework of CTA and thus exhibits many similarities in properties, comparing their behavior may provide insight into the understanding of the high-pressure reactions. For both compounds, when pressure is beyond certain threshold, ring-opening reaction or polymerization will happen. When decompressed to ambient pressure, the IR spectra of both compounds showed more information than the Raman spectra due to the average effect. The reason is likely due to the disordered form has no prominent Raman features, while the functional groups may be similar to the initial compound and thus exhibits the similar IR absorptions. The high-pressure XRD measurements of both compounds as well as the data analyses are needed to further clarify the changes and reaction mechanisms.

Based on the spectroscopic data, XRD measurements and theoretical calculations, we know that a tritetrazole isomer is likely formed under high pressure. However, according to Hu *et al.*[16], the formation of the infinite polymeric nitrogen network will be favored at high pressure and high temperature. Therefore, future works on the high pressure together with high temperature are needed to synthesize the polymeric nitrogens.

4.5 Conclusion

Using *in situ* Raman and FTIR spectroscopies, as well as X-ray diffraction, we investigated high-pressure properties of s-triazine and CTA up to 22 GPa and 39 GPa, respectively. Four phase transitions were observed at around 0.9, 2, 5 and 9 GPa for s-triazine, evidenced by the changes in peak profiles, the number of vibrational modes, as well as the pressure dependence of Raman lattice modes over different pressure ranges. Additionally, the transition was identified irreversible for the lattice modes were not recovered and ring-opening reaction occurred with low yield. For CTA, no phase transitions were found under 26 GPa and a chemical reaction was observed above 26 GPa, evidenced by the changes of the IR profiles, the color change of the sample as well as the recovered Raman and IR spectra. A possible tri-tetrazole isomer was proposed for the high-pressure structure of CTA. This transformation is chemical in nature which can be attributed to the intramolecular polymerization of azide groups and the triazine ring. Further theoretical and experimental investigations are required to justify the high-pressure structure and possible transition mechanism of s-triazine and CTA.

4.6 Acknowledgements

The authors acknowledge funding support from a Research Tools and Instruments Grant from the National Science and Engineering Research Council of Canada, a Leaders Opportunity Fund from the Canadian Foundation for Innovation, an Early Researcher Award from the Ontario Ministry of Research and Innovation and a Petro-Canada Young Innovator Award from the University of Western Ontario, a grant from Defense Research and Development Canada at Suffield.

4.7 References

(1) Klapötke, T. M.; Mayer, P.; Schulz, A.; Weigand, J. J. *J. Am. Chem. Soc.* **2005**, *127*, 2032.

(2) Dixon, D. A.; Feller, D.; Christe, K. O.; Wilson, W. W.; Vij, A.; Vij, V.; Jenkins, H. D. B.; Olson, R. M.; Gordon, M. S. *J. Am. Chem. Soc.* **2003**, *126*, 834.

(3) Huynh, M.-H. V.; Hiskey, M. A.; Hartline, E. L.; Montoya, D. P.; Gilardi, R. *Angew. Chem. Int. Ed.* **2004**, *43*, 4924.

(4) Vij, A.; Pavlovich, J. G.; Wilson, W. W.; Vij, V.; Christe, K. O. *Angew. Chem. Int. Ed.* **2002**, *41*, 3051.

(5) Eremets, M. I.; Gavriliuk, A. G.; Trojan, I. A.; Dzivenko, D. A.; Boehler, R. *Nat. Mater.* **2004**, *3*, 558.

(6) Ciezak, J. A. *Propellants Explos. Pyrotech.* **2010**, *35*, 550.

(7) Ciezak, J. A. *Propellants Explos. Pyrotech.* **2010**, *35*, 373.

(8) Ciezak, J. A. *Propellants Explos. Pyrotech.* **2010**, *35*, 24.

(9) Ciezak, J. A. *Propellants Explos. Pyrotech.* **2011**, *36*, 446.

(10) Ciezak, J. A. *AIP Conf. Proc.* **2012**, *1426*, 1424.

(11) Ciabini, L.; Gorelli, F. A.; Santoro, M.; Bini, R.; Schettino, V.; Mezouar, M. *Phys. Rev. B* **2005**, *72*, 094108.

(12) Zhuravlev, K. K.; Traikov, K.; Dong, Z.; Xie, S.; Song, Y.; Liu, Z. *Phys. Rev. B* **2010**, *82*, 064116.

(13) Eckert, J.; Fincher Jr, C. R.; Heilmann, I. U. *Solid State Commun.* **1982**, *41*, 839.

(14) Dove, M. T.; Ewen, P. J. S. *J. Chem. Phys* **1985**, *82*, 2026.

(15) Knaggs, I. E. *Proc. Nat. Acad. Sc.i, Wash.* **1935**, *150*, 576.

(16) Anguang, H.; Fan, Z. *J. Phys.: Condens. Matter* **2010**, *22*, 505402.

(17) Jayaraman, A. *Rev. Sci. Instrum.* **1986**, *57*, 1013.

(18) Larkin, P. J.; Makowski, M. P.; Colthup, N. B. *Spectrochim. Acta A* **1999**, *55*, 1011.

(19) Daunt, S. J.; Shurvell, H. F.; Pazdernik, L. *J. Raman. Spectrosc.* **1975**, *4*, 205.

(20) Jonassen, H. B.; Paukert, T.; Henry, R. A. *Appl. Spectrosc.* **1967**, *21*, 89.

(21) Shearer, S. J.; Turrell, G. C.; Bryant, J. I.; Brooks Iii, R. L. *J. Chem. Phys.* **1968**, *48*, 1138.

(22) Eremets, M. I.; Popov, M. Y.; Trojan, I. A.; Denisov, V. N.; Boehler, R.; Hemley, R. J. *J. Chem. Phys.* **2004**, *120*, 10618.

(23) Dove, M. T.; Ewen, P. J. S. *J. Chem. Phys.* **1985**, *82*, 2026.

(24) Akella, J.; Kennedy, G. C. *J .Chem. Phys.* **1971**, *55*, 793.

(25) Siegel, L. A.; Williams, E. F. *J. Chem. Phys.* **1954**, *22*, 1147.

(26) Piermarini, G. J.; Mighell, A. D.; Weir, C. E.; Block, S. *Science* **1969**, *165*, 1250.

(27) Ciabini, L.; Santoro, M.; Bini, R.; Schettino, V. *J. Chem. Phys.* **2001**, *115*, 3742.

Chapter 5 Summary and future work

In this thesis, I have studied the high-pressure effects on five nitrogen-rich energetic materials, 5-ATZ, 5-MTZ, BTA·H_2O, s-triazine and CTA, by *in situ* vibrational spectroscopy and X-ray diffraction. Our work represents the first *in situ* high-pressure study of 5-ATZ, 5-MTZ, BTA·H_2O and CTA by Raman and IR spectroscopy and the first *in situ* high-pressure study of s-triazine by Raman and IR spectroscopy at a pressure far beyond previously achieved. The structural stability and reversibility of those compounds were examined. In addition, the high-pressure behaviour of five-membered and six-membered rings was compared to have a more in-depth understanding of the tetrazole and triazine rings. These systematic studies on 5-ATZ, 5-MTZ, BTA·H_2O, s-triazine and CTA will aid the design and synthesis of future energetic materials.

This study has provided some new spectroscopic and structural information of CTA under high pressure, more detailed work still need to be done. For example, the structures of new phases need to be analyzed using Rietveld refinement and compared with the spectroscopic results.

In addition, during the decomposition or detonation of energetic materials, high temperature is usually generated, which will also have a big influence on structural and molecular properties.[1,2] Therefore, the investigation of Raman and IR spectra as a function of temperature combined with pressure will greatly enhance our understanding of the temperature-pressure-induced structural transformations and possibly form the polymeric nitrogens. Furthermore, by shining UV light on compounds with unsaturated compounds under high pressure, polymers could be synthesized[3]. Therefore, the UV light aided high pressure study of those materials should also be explored. Finally, high-pressure studies combined with other techniques on other kinds of nitrogen-rich materials could provide more choices for the development of new energetic materials and more in-depth understanding of the properties and mechanisms under high pressures.

References

(1) Eremets, M. I.; Gavriliuk, A. G.; Trojan, I. A.; Dzivenko, D. A.; Boehler, R. *Nat. Mater.* **2004**, *3*, 558.

(2) Eremets, M. I.; Popov, M. Y.; Trojan, I. A.; Denisov, V. N.; Boehler, R.; Hemley, R. J. *J. Chem. Phys.* **2004**, *120*, 10618.

(3) Chelazzi, D.; Ceppatelli, M.; Santoro, M.; Bini, R.; Schettino, V. *Nat. Mater.* **2004**, *3*, 470.

Appendix: Rietveld refinement

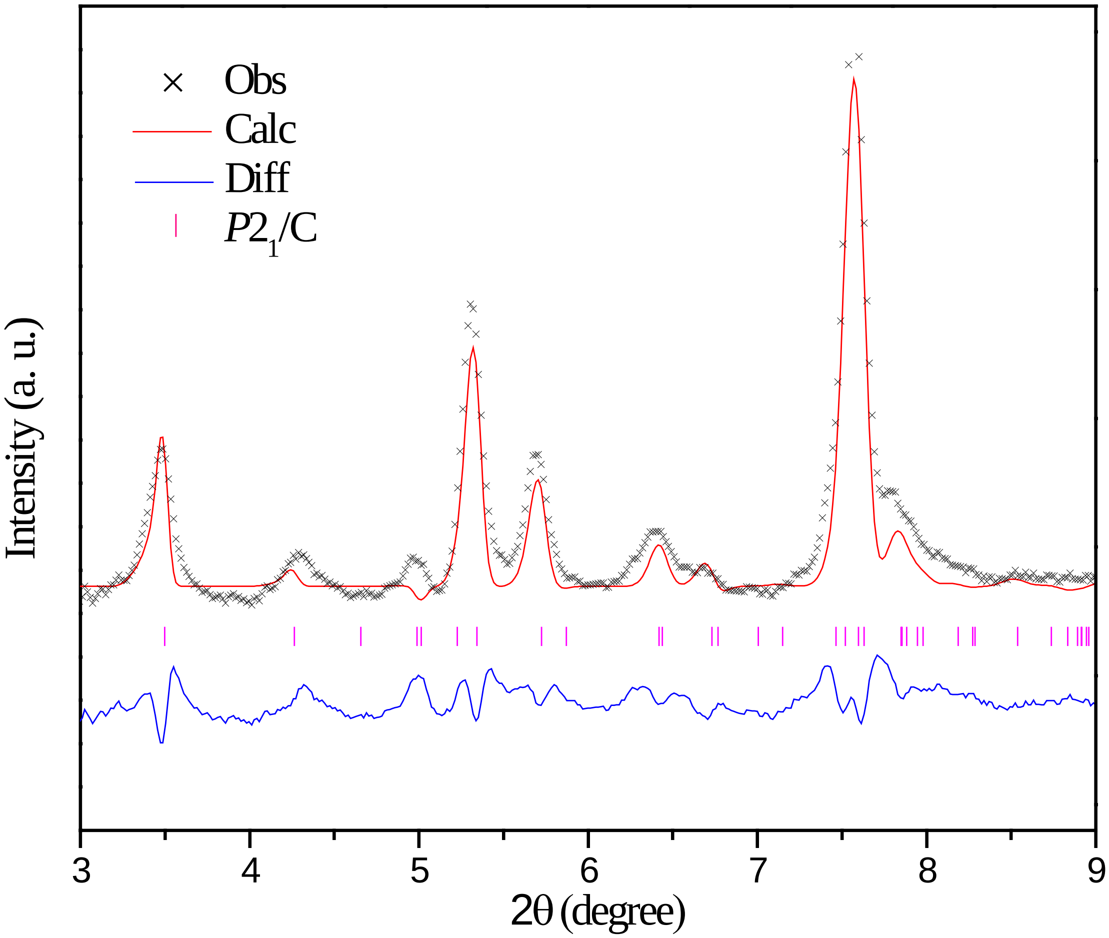

Fig. A1 Rietveld refinement of XRD pattern for BTA·H_2O at 0.12 GPa. The observed data are depicted in crosses (obs), while red and blue solid lines are the calculated (calc) profile and the difference (diff: $I_{obs} - I_{calc}$) curve, respectively.

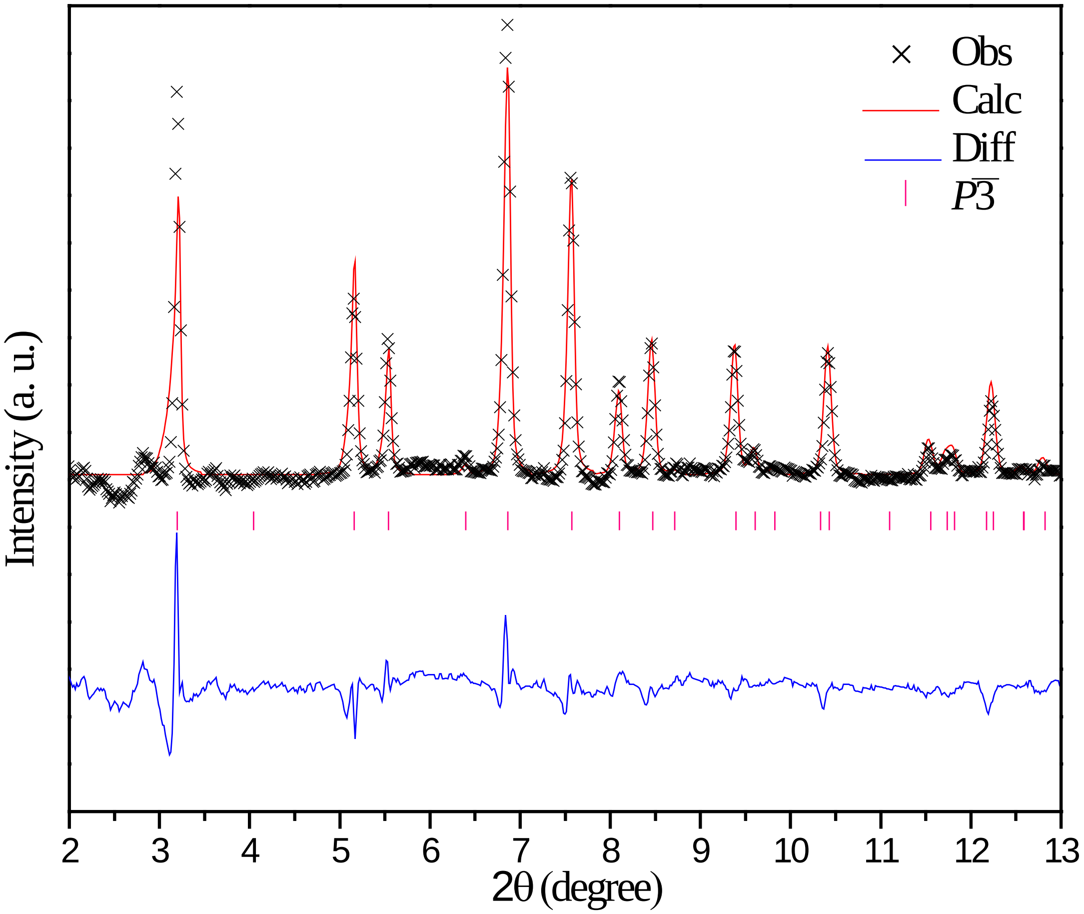

Fig. A2 Rietveld refinement of XRD pattern for CTA at 0.25 GPa. The observed data are depicted in crosses (obs), while red and blue solid lines are the calculated (calc) profile and the difference (diff: $I_{obs} - I_{calc}$) curve, respectively.

Curriculum Vitae

Name:	Liang Zhou
Post-secondary Education and Degrees:	The University of Western Ontario London, Ontario, Canada 2011-2013 M. Sc.
	Shandong University Jinan, Shandong, China 2007-2011 B. Sc.
Honours and Awards:	Excellent Student Scholarship, SDU, 2009-2010
	First Class Student Scholarship, SDU, 2007-2008
Related Work Experience	Teaching Assistant The University of Western Ontario, 2011-2013

Presentations

Zhou, Liang; Till, Erica; Song, Yang; Hu, Anguang; Cook, Cyril; Murugesu, Muralee. “Pressure-induced transformations of 5, 5´-bis(2-methyltetrazolyl)amine monohydrate (BTA·H_2O) and cyanuric triazide (CTA) probed by vibrational spectroscopy and X-ray diffraction”, *The 96th Canadian Chemistry Conference and Exhibition*, Quebec, Canada, May, 2013 (poster)